92PC92104-TPR-13

ADVANCED THERMALLY STABLE JET FUELS

Technical Progress Report
July 1995 - September 1995

H.H. Schobert, S. Eser, C. Song, P.G. Hatcher, A. Boehman, M.M. Coleman

Contributions from:

R. Arumugam, P. Chang, R.Dutta, K. Gergova, E. Kazakova,
E.Korbetskaya, W.-C. Lai, J. Li, S. Lin, S. Martin, M. Reddy,
P. Sanghani, L. Selvaraj, E. Yoon, and J. Yu

October 1995

RECEIVED
USDOE/PETC
95 DEC 21 AM 9:50
ACQUISITION & ASSISTANCE DIV.

Prepared for U.S. Department of Energy
under
Contract No. DE-FG22-92PC92104

MASTER

DISTRIBUTION OF THIS DOCUMENT IS UNLIMITED

OBJECTIVES

The Penn State program in advanced thermally stable jet fuels has five components: 1) development of mechanisms of degradation and solids formation; 2) quantitative measurement of growth of sub-micrometer and micrometer-sized particles suspended in fuels during thermal stressing; 3) characterization of carbonaceous deposits by various instrumental and microscopic methods; 4) elucidation of the role of additives in retarding the formation of carbonaceous solids; and 5) assessment of the potential of producing high yields of cycloalkanes and hydroaromatics by direct liquefaction of coal.

SUMMARY

The quantitative structure-property relationship method, based on comprehensive descriptors applied to the processes of hydrocarbon thermal degradation, demonstrated better performance in predicting degradation behavior of thirteen compounds stressed for four hours at 450°C than did other approaches based only on topological descriptors. Correlations based on comprehensive descriptors require a smaller number of parameters to achieve the same accuracy of prediction.

Further work was conducted in examining the effects of reactant and inert gas pressure on solids formation in supercritical and gas-phase pyrolysis of *n*-tetradecane at 450°C. *n*-Tetradecane was pyrolyzed in amounts of 1–9 mL and (cold) nitrogen pressures of 0.17–2.03 MPa for four hours.

Previously reported work on the thermal decomposition of pure *n*-alkanes under supercritical conditions was extended in this reporting period to an examination of the behavior of Norpar-13, which is a mixture on *n*-alkanes. Thermal stressing experiments were carried out at 425°C in a glass tube reactor and at 450°C in the stainless steel microautoclaves (tubing bomb reactors).

Work also continued on the development of a kinetic model for deposit formation from coal-derived jet fuel. A refined analytical method based on an internal standard was used to calculate concentrations of species and develop correlations for stressed fuel samples.

High-surface area activated carbons PX-21 and Maxsorb 92-11A, 94-06, and 94-20 have significant effects on decomposition reactions during the thermal stressing of *n*-alkanes at 425° and 450°C. The surface area and surface functionalities are the two most important parameters that influence the carbon activity. The higher the surface area, the more prominent is the effect of activated carbon; however, carbons with very high surface area (>2000 m^2/g) do not differ in their performance during thermal stressing. The active carbon surfaces catalyze hydrogen transfer reactions. Outgassed carbons (i.e., treated in nitrogen at high temperatures) showed higher activity during thermal stressing of *n*-dodecane at 450°C for one hour, but lower activity at 450°C for four hours, stressing compared to the original carbons. Oxidation of PX-21 decreases its effectiveness in stabilizing *n*-dodecane.

The carbonaceous solids deposited on the carbon surfaces during thermal stressing also play a catalytic role, which is attributed to specific oxygen functionality on the carbon surface and adsorbed species. Carbonaceous solid deposited on the carbon surfaces leads to a sharp decrease of nitrogen BET surface area.

Characterization of deposits from actual engine parts shows that different reaction and deposition mechanisms prevail in different sections of the fuel system. Metal surface seems to be an important factor for the formation of deposits inside the main tip. Temperature and concentrations of oxygen are the other important factors which govern deposition on different parts of an engine fuel system. The deposits obtained with model compounds heated in the presence of metal foils bear resemblance to those from actual engines in that a two-layer deposit structure is observed on an active metal substrate, such as nickel.

Kinetic studies were performed on dodecane, dodecane/tetrahydroquinoline mixtures, and dodecane/benzyl alcohol mixtures in the temperature range 400–500°C. The rate constants and Arrhenius parameters were calculated.

Exploratory work has continued on seeking a mild-condition pathway to coal hydrogenation. Samples of Wyodak subbituminous coal have been submitted for major and minor elemental analysis to allow determination of the distribution of mineral species (that might serve as in situ catalysts for hydrogenation), and whether the concentrations of ion-exchangeable cations (Ca, Mg, Na, and K) have been reduced upon demineralization. Non-catalytic liquefaction tests on the untreated coal are being conducted at lower temperatures and higher hydrogen pressures to evaluate the threshold conditions for preferential gas-phase hydrogen reactivity.

Work has also continued on reactions of Pittsburgh No. 8 bituminous coal at mild conditions. Some evidence for hydrogenation at 300°C in the presence of 9,10-dihydrophenanthrene was observed, but conversions and transformation of aromatic to aliphatic carbon were quite low.

The hydrogenation and dehydrogenation behaviors of naphthalene, phenanthrene, and pyrene were investigated via their product distributions and kinetic and thermodynamic parameters. Hydrogenations were carried out at 350, 400, and 450°C for various times up to equilibrium conditions. A global kinetic model was used to determine forward and reverse rate constants, which were then used to determine Arrhenius parameters. Enthalpy data were obtained and compared to literature values. The temperature at which dehydrogenation becomes favorable relative to hydrogenation reactions decreases with increasing ring size.

Low-temperature catalytic hydrogenation of naphthalene was investigated as a model reaction for low-temperature hydrotreating of coal-derived liquids to produce thermally stable jet fuels. Supported noble metal catalysts were found to be significantly more active than a commercial NiMo hydrotreating catalyst. At 473 K naphthalene hydrogenation over these noble metal catalysts can proceed even in the presence of 4200 ppm benzothiophene. Sulfur addition decreases the activity of all the noble metal

catalysts. Palladium catalysts have higher sulfur resistance than platinum. A Pd/TiO_2 catalyst was the most active and the least affected by sulfur among the three noble metal catalysts studied.

Mesoporous molecular sieves were shown to be active for the hydrocracking of bulky hydrocarbon molecules. Acidity is a key factor; it depends on the aluminum incorporation. Mesoporous molecular sieve catalysts also seem to be more stable—in terms of less coke formation—for the conversion of bulky hydrocarbons as compared to microporous molecular sieves.

Task 1. Investigation of the Quantitative Degradation Chemistry of Jet Fuels

1. The Study of Quantitative Structure-Thermal Stability Relationships in the Pyrolysis of Pure Hydrocarbons (Contributed by Elena Kazakova)

Introduction

This section of the report describes the continuing study of hydrocarbon degradation with the Quantitative Structure-Property Relationship (QSPR) method. As shown previously [1], this method has a strong potential as a tool for prediction of chemical properties. In the present work, the general QSPR analysis was performed using a set of united constitutional, topological, geometrical, electrostatic, and quantum-chemical descriptors. The same experimental data as in the previous study [1] were considered.

Preliminary Results

The first data set represents the experimental conversion results for 13 compounds after 4-hour high-pressure pyrolysis at 450°C [2-7]. This set was considered for linear regression analysis using comprehensive descriptors. The correlation obtained, based on three descriptors, is given by

$$C = (-134.85 \pm 34.069) + (134.92 \pm 18.437)\alpha_1 - (1237.2 \pm 383.08)\alpha_2 - (5.706 \pm 2.57)\alpha_3 \quad (1)$$

where α_1 is internal entropy of the molecule at 300 K divided by the number of atoms in the molecule, α_2 is relative positive charge, and α_3 is Kier shape index (order 3). The values of multiple correlation coefficient, R^2, and standard deviation, S^2, are 0.9023 and 174.75, respectively. It is worthwhile to point out that S^2 is an absolute (not relative) standard deviation. Figure 1 shows the comparison of the performance of previously obtained equation [1], based on topological descriptors only, and equation (1).

The correlation one-descriptor correlation

$$C = (-37.873 \pm 14.819) + (85.957 \pm 12.816)\beta_1 \quad (2)$$

also shows reasonable agreement in terms of R^2 and S^2 (0.8035, 287.55). The parameter β_1 in equation (2) is vibrational entropy of the molecule at 300 K divided by the number of atoms in the molecule. Figure 2 presents the comparison of predictions of equation (2) and the correlation based on topological descriptors only [1].

The second experimental data set used for the QSPR search contains the results of the Monsanto group [8] in the form of kinetic parameters and rate constants obtained in static tests (high pressure, 700 K). The linear equations for $\ln(k_0)$ have been generated in the form of

$$\ln(k_0) = 24227.-6092.9\gamma_1 - 153.17\gamma_2 - 109.78\gamma_3 \qquad (3)$$

where γ_1 is average valency of a C atom, γ_2 is maximum total bond order of a C atom, and γ_3 is average atomic nucleophilic reaction index for a C atom. The multiple correlation coefficient is 0.9925 and standard deviation is 0.0329. Figure 3 shows the performances of the topology-reduced (with 5 descriptors used) [1] and the comprehensive (with 3 descriptors used) QSPR applications.

The similar equation for the average rate constant for decomposition of saturated cyclic hydrocarbons is given by

$$k_{av} = 0.0486 + 0.00835\lambda_1 - 0.0546\lambda_2 - 0.0414\lambda_3 \qquad (4)$$

where λ_1 is weighted positive surface area, λ_2 is Kier&Hall index (order 2), and λ_3 is number of rings. The values of R^2 and S^2 are 0.93 and 0.0016, respectively. Figure 4 presents the comparison of performance of topology-based equation [1] and the equation (4).

All calculations have been carried out with CODESSA package developed by the group of Prof. A. R. Katritzky at Florida Sate University [9]. The input files for all compounds studied were generated using the MOPAC 5 code [10] .

Conclusion

The QSPR method based on comprehensive descriptors applied to the processes of hydrocarbon thermal degradation demonstrated better performance as compared to the approach based on topological descriptors only. The correlations based on comprehensive descriptors require a smaller number of parameters to obtain the same quality of predictions.

References

1. Kazakova, E. *The Study of Quantitative Structure Stability Relationships in the Pyrolysis of Hydrocarbons* (Department of Material Science & Engineering, The Pennsylvania State University, 1995).

2. Lai, W.-C.,*Pyrolysis of Tetradecane at Elevated Pressure for Long Duration: Product Distribution and Reaction Mechanisms* (Department of Material Science & Engineering, The Pennsylvania State University, 1992).

3. Lai, W.-C. , C. Song,*Pyrolysis of Alkylcyclohexanes at 450°C and Elevated Pressure. Product Distribution and Reaction Mechanism* (Department of Material Science & Engineering, The Pennsylvania State University, 1993).

4. Lai, W.-C., C. Song, *Product Distribution of the Pyrolysis of n-Tetradecane at 400°C and 425°C* (Department of Material Science & Engineering, The Pennsylvania State University, 1993).

5. Peng, Y.,*Pyrolysis of Butylbenzenes: Effect of Structure of Alkyl Side Chain on the Pyrolysis of Alkylbenzenes* (Department of Material Science & Engineering, The Pennsylvania State University, 1992).

6. Peng, Y., *Pyrolisis of Octylbenzene: Effect of Structure of Alkyl Side Chain on the Pyrolysis of Alkylbenzenes* (Department of Material Science & Engineering, The Pennsylvania State University, 1992).

7. Peng, Y..*Pyrolysis of n-Alkylbenzenes* (Department of Material Science & Engineering, The Pennsylvania State University, 1994).

8. Fabuss, B.N., J.O. Smith, and C.N. Satterfield, in *Advances in Petroleum Chemistry and Refining* (eds. Kobe, K.A. & McKetta, J.J.), 157 (Interscience Publishers, New York, 1964).

9. Katritzky, A., V. Lobanov, and M. Karelson,*CODESSA*: *Comprehensive Descriptors for Structural and Statistical Analysis* (University of Florida, Gainesville, 1995).

10. Stewart, J.J.P. *Quantum Chemistry Exchange Program (Indiana University, Bloomington, Indiana, 1983), No. 455.* (1983).

2. *Effects of Reactant and Inert Gas Pressure on the Solid Formation in Both Supercritical- and Gas-Phase Pyrolysis of n-Tetradecane at 450 °C (Contributed by Wei-Chuan Lai and Chunshan Song)*

Introduction

In previous quarterly reports, we have reported that there is a significant pressure dependence in the pyrolysis of *n*-tetradecane (*n*-C_{14}) at 450 °C for 30 min under initial (cold) N_2 pressures of 0.17-2.03 MPa using 1-11 mL samples in two types of microreactors (28 mL and 23.2 mL) [1,2]. Little is known about the role of reactant and inert gas pressure in supercritical fluids at high temperatures for long-duration pyrolysis. With the goal of understanding the effects of reactant and inert gas (N_2) pressure on the *n*-C_{14} decomposition, solid deposit formation, and product distribution, we pyrolyzed *n*-tetradecane using 1-9 mL samples at 450 °C for 4 h under initial (cold) N_2 pressures of 0.17-2.03 MPa (10-280 psig) in 28-mL microreactors. The present work covers the long-duration thermal decomposition of *n*-C_{14} in both supercritical phase and gas phase.

Experimental

Aldrich reagent-grade *n*-tetradecane, *n*-C_{14} (purity: 99+ %) was used as received in this work. A given amount of *n*-C_{14} (1, 5, or 9 mL) was charged into a 28-mL microreactor (unmodified reactor with "cold volume", see reference [2]). After the reactor was sealed and purged six times with 6.9 MPa ultra-high purity (UHP) N_2, it was pressurized with UHP N_2 to a certain pressure ranging from 0.17 MPa to 2.03 MPa. The pyrolysis was conducted at 450 °C for 4 h in a fluidized sand bath. The products were separated into gases, liquids, and solid deposits by using the procedure described elsewhere [3]. The gaseous and liquid products were analyzed by GC and GC-MS with packed or capillary columns [3].

Results and Discussion

Because the pyrolysis temperature is above the critical temperature of *n*-C_{14} (419 °C), it is worth discussing the initial system pressure and phase behavior of the *n*-C_{14}-N_2 mixtures. Since the effect of sample volume reflects the influence of reactant pressure, we have calculated the initial total pressure of the *n*-C_{14}-N_2 mixtures (at 450 °C) and their critical pressures and temperatures using the equations of state recommended by Reid et al. [4] Table 1 shows the reduced pressure (ratio of total pressure to the critical pressure) of the mixtures at 450 °C. The data in Table 1 indicate that the reactant likely exists in supercritical phase when the initial sample volume is 9 mL under all the N_2 pressures examined, and in low-density gas phase when the initial sample volume is 1 mL. With 5-mL sample, the phase of the reactant at 450 °C could be either medium-density gas phase or near supercritical phase, depending on the initial N_2 pressure. In general, pressure affects the density, viscosity, and diffusivity. Pressure change near critical point can change the system from gas-like to liquid-like phases or vice versa, and may affect the chemical reaction behaviors [5-7].

Figure 5 shows the *n*-C_{14} conversion as a function of the initially charged *n*-C_{14} volume at four different initial N_2 pressures in the 28 mL microreactors. The experimental error was 0.83%, determined from three replicates using 5 mL samples under 0.79 MPa N_2. Note that 1 mL of *n*-C_{14} corresponds to a *n*-C_{14} concentration of 0.138 mol/L. The *n*-C_{14} conversion displays a concave downward (volcano-like) behavior with the reactant volume (concentration); a maximum conversion occurs at 0.69 mol/L (or 5 mL of *n*-C_{14}). The current results indicate that there are moderate changes in *n*-C_{14} conversions with changes in sample volume (concentration), especially when the *n*-C_{14} loading increases from 5 mL to 9 mL. For example, at a low initial N_2 pressure (0.17 MPa), increasing sample volume from 5 to 9 mL decreased *n*-C_{14} conversion from 98.6 to 91.2 mol %. Changes in sample volume from 1 to 5 mL had less impact on *n*-C_{14} conversion, but one can find a small increase in conversion with increasing sample volume. The pressure of the inert gas (N_2) has little impact on the decomposition rate of *n*-C_{14} when small sample (1 or 5 mL) was used; however, at a higher initial *n*-C_{14} concentration (9 mL sample), increasing N_2 pressure increased *n*-C_{14} conversion. In short, the influence of the reactant volume (concentration) appears to also depend on the system phases. We can find that the *n*-C_{14} decomposition rate was retarded when the system phase was changed from gas to supercritical phase. The decrease might be attributed to cage effects or diffusion limitations, which may be expected at high density due to the more restricted mobility of molecules.

Inhibition of solid formation from long-duration pyrolysis of n-C_{14} was observed by changing reactant or inert gas pressure as shown in Figure 6, which shows the solid yields as a function of the initially charged *n*-C_{14} volume and N_2 pressure. Similar to the *n*-C_{14} conversion, the solid yield also displays a volcano-like behavior with the reactant volume (concentration); maximum solid formation occurs at 0.69 mol/L (or 5 mL of *n*-C_{14}). In general, the solid formation was retarded when the system phase was changed from medium-density gas phase to supercritical phase. For example, at an initial N_2 pressure of 0.79 MPa, increasing the reactant concentration from 0.69 mol/L (or 5 mL of *n*-C_{14}) to 1.24 mol/L (or 9 mL of *n*-C_{14}) reduced the formation of deposits by 77 % (from 3.1 % to % 0.7 wt %). The decrease of solid deposition might be attributed to the enhanced solid solubility of the fuel under supercritical condition (a physical process) [8], or it might be due to a chemical process as suggested by Edwards and Zabarnick [9]. It is also interesting to note that the pressure of N_2 has significant impact on the formation of deposits when small sample (1 mL) was used. For example, the solid yields range from 0.6 wt % to 2.8 wt % when the pyrolysis was started with 1-mL *n*-C_{14}. In short, the influence of sample volume and inert gas pressure on solid formation is interdependent; i.e., increasing sample volume can either decrease or increase solid formation, depending on the inert gas pressure, and vice versa. This illustrates the complexity of the mechanisms governing the pressure effects of reactant and inert gas.

The total gas yields (C_1-C_4) from *n*-C_{14} are shown in Figure 7 as a function of the initially charged *n*-C_{14} volume and N_2 pressure. Gas yield (wt %) decreases with increasing reactant volume (concentration) under constant initial N_2 pressure. In contrast to the effect of reactant pressure, the pressure of the inert gas (N_2) has less impact on the total gas yield under the studied N_2 pressure ranges, and the effect of N_2 pressure also depends on the reactant pressure. These observations imply that lower reactant pressure facilitates unimolecular reaction (β-scission) to form low molecular-weight gases while higher reactant pressure favors bimolecular reaction (H-abstraction). It is possible to control the product distributions as well as reaction extent by isothermally adjusting the system pressure in terms of sample volume or inert gas pressure.

References

1. Schobert, H. H.; Eser, C.; Song, C.; Hatcher, P. G.; Walsh, P. M.; Coleman, M. M. *Advanced Thermally Stable Jet Fuels.* Technical Progress Report (January 1994 - March 1994), May **1994**, The Pennsylvania State University.
2. Schobert, H. H.; Eser, C.; Song, C.; Hatcher, P. G.; Boehman, A.; Coleman, M. M. *Advanced Thermally Stable Jet Fuels.* Technical Progress Report (July 1994 - September 1994), October **1994**, The Pennsylvania State University.
3. Lai, W.-C.; Song, C.; Schobert, H. H.; Arumugam, R. *Prep. - Am. Chem. Soc. Div. Pet. Chem.* **1992**, *37* (4), 1671-1680.
4. Reid, R. C.; Prausnitz, J. M.; Poling, B. E. *The Properties of Gases & Liquids.* Fourth Edition. **1987**, McGraw-Hill Book Company: New York.
5. Tiltscher, H.; Hofmann, H. *Chem. Eng. Sci.* **1987**, *42* (5), 959-977.
6. Laidler, K. J. *Chemical Kinetics.* Third Edition. **1987**, Harper & Row Publishers: New York, Chapter 6.
7. Eckert, C. A. *Annu. Rev. Phys. Chem.* **1972**, *23*, 239-264.
8. Taylor, W. F. *Ind. Eng. Chem. Prod. Res. Dev.* **1974**, *13* (2), 133-138.
9. Edwards, T.; Zabarnick, S. *Ind. Eng. Chem. Res.* **1993**, *32*, 3117-3122.

Task 2. Investigation of Incipient Deposition

Deposit Growth During Heating of Coal-Derived Aviation Gas Turbine Fuels (Contributed by Prashant C. Sanghani and Andre L. Boehman)

In a previous report, we had discussed the use of information from model compound studies to develop rate expression for deposits formation from jet fuel. We are continuing our work on development of a kinetic model for deposit (i.e. coke) formation from coal-derived jet fuel. With the refined analytical method based on internal standard that was proposed in a previous report, concentrations of species were calculated and correlations were developed in stressed fuel samples.

The kinetics of coke formation from coal-derived jet fuel were studied using statistical methods. The degree of correlation between deposit (coke) growth and species concentration has been examined. Detailed composition analysis of neat mixture of fuel and tetradecane and pyrolysed samples were performed using GC and GC/MS. Formation of deposits from the mixtures of jet fuel and tetradecane was found to be approximately proportional to the initial concentration of tetradecane present in the mixture of tetradecane and fuel. Figure 15 shows a plot of mass fraction of solid produced versus initial concentration of tetradecane in the mixtures of tetradecane and coal-derived jet fuel with its correlation coefficient. Decomposition of tetradecane present in the fuel-tetradecane mixture was found to be first order with correlation coefficient of 0.98. A plot of tetradecane decomposition at 450^0C with its correlation coefficient is shown in Figure 16. The change in concentrations of compounds such as cycloalkanes, alkylated C_1, C_2, C_3 benzenes, and alkylated naphathalenes present in the jet fuel mixture at different time intervals are minimal. This led us to the conclusion that these compounds do not contribute to the solid formation during the pyrolysis of jet fuel. Detailed species-by-species identification is not yet finished. Since in the individual model compound studies tetradecane was found to produce maximum solids and disappearance of tetradecane during pyrolysis is much faster than other compounds, we concluded that tetradecane is the sole contributor to solids formation. The natural logarithm of tetradecane concentration remaining in the mixture at 450^0C at various intervals of time versus measured deposit mass is plotted in Figure 17. The correlation coefficient between tetradecane concentration and deposit mass was found to be 0.901. Therefore linear correlation between tetradecane and deposit mass is poor. Also it can be seen that more than 50% tetradecane undergoes decomposition before an observable mass of deposit forms. This is attributed to the presence of an induction period prior to significant deposition. Most of the deposit ($\approx$ 95%) forms by addition of reactive species on already growing films of deposits rather than a homogeneous process that occurs to a significant extent during the autoxidation regime. The statistical approach helps in identifying or arranging species in terms of their contribution to deposit formation. Grouping species on the basis of their correlation with deposit formation clarifies the required structure for a general kinetic model of the jet fuel degradation process.

Task 3. Characterization of Solid Gums, Sediments, and Carbonaceous Deposits.

1. Characterization of Actual Engine Deposits (Contributed by Jun Li and Semih Eser)

Introduction

In previous reports, we have presented results of characterization of deposits produced in a tubing bomb reactor [1] and in a flow reactor [2]. In this report, we will include data from characterization of actual engine deposits.

Characterization of actual engine deposits can serve two general purposes: It can help to identify the main cause for deposition in the engine system to provide measures for preventing deposit formation, and it offers a check on the relevance of our laboratory studies to the solid deposition observed in actual engine fuel system. We have previously documented that different solid formation and deposition mechanisms can be responsible for deposition accumulation on different parts or components of the fuel system in an aircraft.

Experimental

Two different types of actual engine deposits were examined: deposits from a fuel line, and deposits from a fuel nozzle. The nozzle deposits are further classified into two categories, main tip deposits and metering set deposits. Part of the carbonaceous deposits on these engine parts were scraped off, mixed with KBr to make a 1% deposit pellet, and examined using Fourier transform infrared spectroscopy (FTIR). The deposits from the engine parts were also made into an epoxy pellet for examination by polarized-light microscopy. The morphology of the deposits was examined using scanning electron microscopy (SEM) coupled, in some cases, with an energy-dispersive x-ray (EDX) detector for element mapping.

Results and Discussion

Fuel Line Deposits. Figure 18 shows a photograph of the afterburner fuel lines with carbonaceous deposit. It can be seen that, at severe deposition sections, the fuel line is entirely clogged with solids. Polarized-light micrographs in Figures 19 and 20 show that the solids have a highly anisotropic, pyrolytic carbon structure with distinct layers formed by vapor-phase deposition [3]. At the beginning of each coarse deposit layer, there is a thin layer (about 3–5 μm) of less oriented deposit. On top of this thin layer forms the typical cone structure of pyrolytic carbon. Closer to the metal surface, the pyrolytic carbon deposit appears to be more columnar than conical. Away from the surface, the growth cones become distinct and exhibit "regenerative" nucleation with random distribution of nucleation sites seen as the tips of the growth cones.

It is generally considered that the regenerative sites for the conical growth of pyrolytic carbon result from particulate carbons present in a gas phase [4]. It is possible that the gas-borne particles constitute apparently less-ordered thin layers which serve as nucleation sites for the growth of pyrolytic cones. The different appearance of the deposit layer next to the metal surface compared to the other sections of the deposits suggests that the metal surface plays a different role in initiating the deposition process. It is, however, clear that the incipient deposit surface, as well as the subsequent layers of the deposit, hosts a prolific growth of pyrolytic carbon structures under the conditions present in the afterburner fuel line.

Nozzle Deposits. It is known that different parts of a fuel nozzle are exposed to different conditions (e.g., temperature, fuel and air concentrations, flow rate). Therefore, it is important to collect deposit samples from different parts of the nozzle. Figure 21 is a composite SEM micrograph showing the morphology of deposits on the primary metering set, from the inlet end (at the bottom of the micrograph) with an O-ring to the outlet end (on top of the micrograph) close to the secondary spin slots at the tip. It is seen that the deposit is thicker at the outlet end, gradually becomes thinner as it moves closer to the inlet end (O-ring). This indicates that deposition starts at the outlet, then works its way towards the inlet. Spherical carbon particles are clearly seen on the sections of the metering set with changing outside diameter (Figure 22). These particles were probably nucleated in the gas phase and precipitated out from the fluid phase since they had become insoluble in the flowing fluid. Possibly, the initial particles contain high concentrations of oxygen groups. Polarized-light micrographs (Figure 23) show that the deposits in this area have an isotropic texture within a scale of 1 μm.

In the secondary spin slots, deposition is heavy. The slots are almost filled with bulk deposit (Figure 24). Polarized-light microscopy shows that deposit in the secondary spin slots also has an isotropic texture (Figure 25).

On the inside surface of the main tip, carbon deposits are found in colonies of porous particulate aggregates (Figure 26). Polarized-light microscopy (Figure 27) reveals that the deposit in this area consists of two layers: An initial dense layer with many bright particles scattered along this layer, and a subsequent porous layer. Back-scatted electron microscopy shows that these particles are about 500 nm in size. The composition of these particles can be determined qualitatively by X-ray elemental mapping. Figures 28 and 29 show that Ni, Fe, and Cr are the main elements constituting these particles, and Ni appears to be the most abundant among the three in the dense layer of carbon close to the metal surface. It is clear that metal particles were lifted from the surface and incorporated in the carbonaceous deposit, suggesting that the metal surface was actively involved in the formation of the incipient deposits.

The metal surface effects are not readily visible on the deposits collected on the metering set, probably because of higher oxygen concentrations (from air) present around the metering set during deposit formation. Figures 30 and 31 show the FTIR spectra of deposits collected from the metering set and from inside surface of the main tip. It can be seen that the oxygen functional group content (mainly as CO groups) is higher in the metering set deposits than that in the main tip deposits.

Summary

Characterization of deposits from actual engine parts show that different reaction and deposition mechanisms prevail in different sections of the fuel system. Metal surface seems to be an important factor for the formation of deposits inside the main tip. Temperature and oxygen concentrations of oxygen are the other important factors which govern deposition on different parts of an engine fuel system. Results from the deposits obtained with model compounds heated in the presence metal foils bear resemblance to those from actual engine deposits, in that, a two-layer deposit structure is observed on an active metal substrate, such as nickel.

References

1. H. H. Schobert, S. Eser, C. Song, P. G. Hatcher, P.M. Walsh, and M.M. Coleman, *Advanced Thermally Stable Jet Fuels*, Technical Progress Report, 92PC92104-TPR-5 and 92PC92104-TPR-7.

2. H. H. Schobert, S. Eser, C. Song, P. G. Hatcher, P.M. Walsh, and M. M. Coleman, *Advanced Thermally Stable Jet Fuels*, Technical Progress Report, 92PC92104-TPR-10, 36-40, February, 1995.

3. H. H. Schobert, S. Eser, C. Song, P. G. Hatcher, P.M. Walsh, and M. M. Coleman, *Advanced Thermally Stable Jet Fuels*, Technical Progress Report, 92PC92104-TPR-5 and 92PC92104-TPR-3, 15-40, July, 1993.

4. J. C. Bokros, in *Chemistry and Physics of Carbon*, P. L. Walker, Jr. editor, Marcel Dekker, Inc, New York, 1-118, 1969.

2. *Effects of Solid Carbon Surfaces on Thermal Decomposition of n-Dodecane (Contributed by Katia Gergova, Rathnamala Arumugam, Philip Chang, and Semih Eser)*

Introduction

The presence of different solid carbons added to *n*-alkanes during thermal stressing at temperatures higher than 400°C causes substantial changes in decomposition reactions. The high surface area activated carbons (2000-3000 m^2/g) were found to be very effective in suppressing thermal degradation of *n*-alkanes and preventing carbonaceous solid formation on metal surfaces [1]. In addition, the hydrogen transferring pyrolysis of *n*-alkanes in the presence of decalin and high surface area carbons showed that the active carbon surfaces catalyze hydrogen transfer [2]. Although the surface area and accessibility of the active sites are important factors in some reactions, the nature of the carbon surfaces and the presence of surface oxygen groups play a dominant role in other reactions [3,4]. The carbonaceous solid deposited on the surface of activated carbons during thermal stressing also affects the degradation reactions. The carbonaceous overlayer has always been associated with catalytic poisoning, but it seems that in some cases the overlayer can have catalytic activity. There are evidences that carbon deposited on a catalyst surface is also catalytically active [5]. Some hydrogenation reactions were catalyzed by carbon overlayers [6]. The most obvious catalytic role of carbon is in promoting the deposition of solid carbons [5]. In other cases, the surface complexes may be the active catalysts. Cariaso and Walker [7] found that impurities in the carbon could also have a strong influence on the catalytic reactions.

The ability of carbon surfaces to promote a variety of surface reactions has been studied over many years and many catalytic reactions of carbon have been reported. To the best of our knowledge, there are no studies reported in the literature on the effect of carbon surfaces on pyrolysis of jet fuel range hydrocarbons.

The main objective of this work is to study the effects of active carbon surfaces during thermal decomposition of *n*-dodecane. The results are presented in two parts; the first part includes thermal stressing of *n*-dodecane in the presence of high surface area activated carbons which have been subjected to various treatments. In the second part, effects of previously deposited carbonaceous solids on further solid deposition from *n*-dodecane are discussed.

Part 1. Effects of High Surface Area Activated Carbon Addition on Thermal Decomposition of *n*-Dodecane

Experimental

Thermal stressing experiments were carried out on 10 mL *n*-dodecane at 425°C and 450°C for 1h. The experiments were performed in microautoclave reactors purged with ultra-high purity grade nitrogen five times to minimize the presence of dissolved oxygen and finally pressurized to 0.7 MPa with nitrogen. In order to study the transfer reactions in the presence of a hydrogen donor, 5% decalin was added to *n*-dodecane. The effect of several high surface area activated carbons on the thermal decomposition of *n*-alkanes was studied. The high surface area activated carbon PX-21 was obtained from Amoco Oil Company and activated carbons Maxsorb 92-11A, Maxsorb 94-06, and Maxsorb 94-20 were kindly provided by the Kansai Coke and Chemical Company, Ltd. Gas chromatography (GC) of liquid samples after thermal treatment was conducted using a Perkin Elmer 8500 GC with fused silica capillary column. Compounds in the liquid products were identified by capillary gas chromatography-mass spectrometry (GC-MS) using a Hewlett-Packard 5090 IIGC coupled with HP 5971A mass selective detector. Thermogravimetric (TGA) studies of carbon samples were carried out using a Mettler TA 4000 system and 200 ml/min. N_2 flow. The temperature in TGA experiments was increased from 30 to 1000°C at 10°C/min. Surface area and porosity measurements were conducted using Quantachrome automated Adsorption Apparatus-Autosorb 1, model ASTI. The characterization of activated carbons was carried out by N_2 adsorption, and the adsorption data were analyzed by using the BET equation [8] to calculate apparent surface areas of activated carbons and Dubinin-Radushkevich equation to calculate micropore area [9]. The total pore volumes were determined from the amount of vapor adsorbed at a relative pressure of 0.95. The cross-sectional area of nitrogen was taken to be 0.162 nm^2.

Degassing of PX-21 in N_2 A quartz tube and a tube furnace were used for degassing PX-21 in flowing N_2. The samples were heated to 900°C within 2 hours, and held for 1 hour and 4 hours at the temperature prior to cooling in N_2.

Pretreatment of PX-21 with air A quartz tube and a tube furnace were used for the pretreatment in air. The duration of the treatments was one hour at 300°C and approximately five minutes at 750°C. After heating, the samples were cooled in air.

Temperature Programmed Desorption (TPD) Experiments of Carbon Samples. The amounts of CO and CO_2 desorbed from the carbon surface were measured by temperature programmed desorption (TPD) experiments. The TPD experiments were carried out soon after carbon samples were prepared. The contact with air was minimized by using auto-sealed crucibles. The calibration of the instruments were carried out after each TPD experiment.

Results and Discussion

The *n*-dodecane and *n*-dodecane+decalin mixture appear to have a yellow color after thermal stressing at 425°C for 1h. The liquids become brown when stressed at a higher temperature (450°C). Song et al. [10] showed that adding hydrogen donors, such as decalin and tetralin, would decrease the extent of decomposition of alkanes and the gas formation, and the hydrogen donor effect was attributed to the stabilization of the reactive radicals. In our previous work [1] we observed a synergistic effect between activated carbon and decalin addition in suppressing the thermal degradation reactions. When 100 mg PX-21 carbon with BET surface area 2090 m^2/g was added to *n*-dodecane, the liquid product from thermal treatment at 425°C appears to be colorless. The higher temperature of thermal stressing (450°) leads to a yellow color of the resulting liquid. However, the comparison of the appearance of the liquids stressed with and without PX-21 carbon shows that the liquid obtained after stressing of *n*-dodecane and decalin mixture mixed with activated carbon is considerably lighter in color.

These visible differences in the liquids obtained from stressing of *n*-dodecane and 5% decalin with and without activated carbons are confirmed by the differences in the *n*-dodecane concentration after thermal stressing. The liquid obtained from stressing of *n*-dodecane+5% decalin with 100 mg PX-21 at 425°C has 5% higher *n*-dodecane concentration than the liquid stressed without carbon. The difference in the concentration of *n*-dodecane in the product reaches almost 10% at 450°C. These data suggest that activated carbon surfaces play an important role in suppressing thermal decomposition of *n*-dodecane and preventing solid formation during thermal stressing even at temperatures as high as 450°C.

In our previous work we showed that the surface area of activated carbon added to n-alkanes during thermal stressing is a very important parameter, i.e. the higher the surface area, the more effective the carbon surfaces in stabilizing the free radicals and catalyzing recombination reactions. The activity of the carbon increases with the increasing surface area up to 2000 m^2/g. Further increase in the surface area does not seem to change the activity of the carbon. Another important parameter which affects carbon activity is the surface functional groups. The high surface area carbon PX-21 was treated at 900°C for 2h in N_2 atmosphere in order to remove the surface functional groups. The color of the liquid obtained after stressing of *n*-dodecane + decalin + 50 mg outgassed PX-21 is lighter than the color of the liquid obtained after stressing of *n*-dodecane + decalin with 50 mg of original carbon. Figure 32 shows the percentage of *n*-alkanes identified in the liquids obtained after stressing at 425°C. The concentration of *n*-dodecane is 5% higher for the liquid obtained after stressing with outgassed PX-21 than with original PX-21. On the other hand, the concentration of C_7-C_{11} alkanes produced as a result of decomposition of *n*-dodecane at this temperature is significantly lower in the liquid obtained after stressing with the outgassed carbon. The increase in carbon activity can be attributed to increasing number of active sites which were not available before outgassing of the carbon. Figure 33 compares the activity of original PX-21 carbon and outgassed carbon (900°C for 1 h) as a catalyst for enhanced H transfer reactions. The concentration of naphthalene is lower in the liquid obtained after thermal stressing with outgassed PX-21 and the concentration of *cis*- and *trans*-decalin is higher, which indicates that the original carbon has higher activity than the outgassed carbon in promoting H transfer reactions. The difference is most likely due to the capacity of the carbon surface to abstract more hydrogen and re-donate to stabilize the free radicals in the liquids. Original PX-21 carbon probably contained appreciable amounts of chemisorbed oxygen functional groups which were removed during outgassing. In this case, the surface oxygen complexes present on the original PX-21 carbon may be the active sites for hydrogen transfer.

Figure 34 shows the effect of pretreatment of PX-21 (degassing and oxidation) on thermal decomposition of *n*-dodecane at 450°C for 4 h in the presence of 200 mg of added carbon. It can be seen that oxidized PX-21 samples preserved much less *n*-dodecane than untreated PX-21 and degassed PX-21 after thermal degradation experiments. In contrast to the results obtained with the PX-21 degassed for shorter duration (1 h), addition of PX-21 degassed for 4 h appears to preserve less *n*-dodecane than untreated PX-21. This could be due to the removal of some beneficial surface groups from the carbon during prolonged degassing and longer stressing time. Except for the degassed sample, there seems to be an inverse relationship between the amount of CO and CO_2 desorbed from the PX-21 samples and *n*-dodecane preserved after stressing. Oxygen functional groups, especially acidic groups, are known to promote hydrocarbon cracking.

The effect of carbonaceous overlayers deposited on the surface of activated carbon seems to be different from that of the original carbon. Three high surface area activated carbons (Maxsorb) provided by Kansai Coke and Chemical Company, Ltd. as well as PX-21 carbon, were used to study the effect of the carbon surfaces during thermal stressing of *n*-dodecane with 5% addition of decalin at 425°C. The Kansai Coke and Chemical Company, Ltd. reported the following values for the BET N_2 surface areas of Maxsorb activated carbons:

Maxsorb 94-20	2080 m^2/g
Maxsorb 94-06	2320 m^2/g
Maxsorb 92-11A	3190 m^2/g

These carbons showed the same effect as PX-21 carbon. It appears that they successfully suppress the carbon deposition and retard the degradation of *n*-dodecane. Figure 35 shows the concentration of *n*-dodecane in the liquids obtained after thermal stressing of *n*-dodecane mixed with 5% decalin at 425°C for 1h. The *n*-dodecane concentration is the lowest for the liquids stressed without carbon and highest for the liquids stressed with used Maxsorb carbons. The carbonaceous overlayer formed on the carbon surfaces after thermal stressing acts as a more active catalyst than the original carbon. Unlike the oxygen functional groups on the surface of original activated carbon, the oxygen complexes on the carbonaceous overlayer seem to increase the carbon activity. This is an important feature of the deposit formed on the activated carbons because it confirms the concept of dual role of carbon surfaces as a catalyst and inhibitor [11].

The higher activity of outgassed carbon was attributed to the removal of chemisorbed oxygen which renders the active sites available for free radicals. In the case of the carbon covered with carbonaceous solid, the oxygen functional groups appear to be responsible for the higher activity of the carbon. In order to confirm our results, which seem to be contradictory, thermogravimetric analysis of the original, outgassed, and stressed carbon were carried out. Figure 36 shows the TGA of (a) original PX-21, (b) PX-21 outgassed in N_2 at 900°C and (c) PX-21 stressed with *n*-dodecane and 5% decalin at 425°C for 1h. During heating to 1000°C, the total weight loss of outgassed carbon is only 16%, while the total weight loss of original PX-21 is 36%. The considerable difference (20%) of mass loss observed confirmed the presence of various functional groups on the surface of original PX-21 carbon. The TGA of stressed carbon (Figure 36c) shows 20% weight loss due most likely to release of functional oxygen from the carbonaceous overlayer during the heat-up to 1000°C. Part of the weight loss is a result of the liquid adsorbed during thermal stressing.

The studies of the surface area and pore structure of activated carbons before and after stressing with *n*-dodecane and decalin provide some information about their structure and how this structure affects the degradation processes at high temperatures. Table 2 shows the surface area and pore volume of original Maxsorb carbon 92-11A, the carbon after thermal stressing with mixture of *n*-dodecane and 5% decalin, and the carbon coated with carbonaceous solid and stressed with *n*-dodecane and decalin at the same conditions. In addition, 5 g of Maxsorb 92-11A carbon was extracted in Soxhlet apparatus for 24 h using 300 mL toluene, and the *n*-dodecane and toluene mixture was stressed at 425°C for 1 h with the extracted carbon. The surface area and pore volume of extracted carbon before and after thermal stressing is listed also in Table 2. A BET surface of 2710 m^2/g was determined for original Maxsorb 92-11A, which is 400 m^2/g lower than the value reported by the company, which is not unusual keeping in mind that different instruments have been used. As mentioned above, the behavior of the carbons with surface area higher than 2000 m^2/g during thermal stressing with *n*-alkanes at temperature 400–450°C would not differ based only on the differences in the surface area. Table 2 shows that Maxsorb 92-11A carbon has mainly microporous structure. The mesopore area is relatively small and the average pore diameter is in the micropore area. After thermal stressing with the mixture of *n*-dodecane and decalin, the surface area of activated carbon decreased considerably (900 m^2/g) because of the carbonaceous solid deposited on the activated carbon surface. However, the micropore area of activated carbon calculated by N_2 adsorption is the same after thermal stressing at 425°C for 1h. This result suggests that the meso- and macroporosity of the carbon is blocked selectively by the carbonaceous solid deposited on the activated carbon surface. The average pore diameter decreases from 10 to 8Å, which indicates that the percentage of micropores with diameter larger than 5Å increases. The total pore volume also decreases substantially, which confirms that only micropores with diameters equal in size to N_2 molecules and smaller pores predominate. Table 2 shows that the carbon stressed subsequently with *n*-dodecane and decalin mixture does not have any porosity, which is due to the thick carbonaceous solid on its surface.

Although the data for the PX-21 carbon showed that the extraction of the carbon improved its performance in suppressing carbon deposition and improving stability of *n*-dodecane and decalin mixture [12], these results were not confirmed with Maxsorb 92-11A carbon. The extraction of Maxsorb 92-11A carbon led to a substantial decrease of the surface area (Table 2). The total pore volume and the micropore volume also decreased while the average pore diameter showed the same value as the original carbon. These results indicate that the decrease in the surface area is due to adsorption of the extraction liquid (toluene) in the micropores of activated carbon. The thermal stressing of the extracted carbon with *n*-dodecane and decalin decreases its surface area and porosity uniformly rather than selectively. The unique structure of the original carbon was changed during the extraction process. Most likely the active centers available for carbon deposition during thermal stressing were blocked by the solvent, which led to a decrease of the total pore volume as well as the micropore volume of extracted and stressed carbon.

Figure 37 shows the N_2 adsorption isotherms of original Maxsorb 92-11A, stressed Maxsorb 92-11A, and Maxsorb 92-11A after extraction and thermal stressing with *n*-dodecane and decalin at 425°C for 1h. All adsorption isotherms are Type I, which characterizes microporous solids[13]. One can see that the carbonaceous solid deposited on the carbon surfaces does not change the microporous structure of activated carbon and affects only the volume of the gas adsorbed. The absence of hystheresis indicates that the mesoporosity is not developed.

Part 2. Effects of Previously Deposited Carbonaceous Solids on Subsequent Solid Deposition.

Initially, the cleaned bare metal surface of the reactor was used for thermal stressing of *n*-dodecane. Four subsequent experiments were carried out in the same reactors coated with carbonaceous deposits from the previous experiments. After each experiment, the carbonaceous deposit on reactor walls was washed with hexane and dried prior to the next experiment. Subsequent deposit accumulation took place on a solid carbon surface. Some solid carbons which came out of the reactor in the form of flakes were reintroduced into the reactor before the subsequent experiment. The amount of carbon deposit on the walls, and total amount of carbon deposit, including the plugs, are shown for each experiment in Figure 38. The amount of total carbon deposit from the first experiment is slightly less than that obtained by the subsequent experiments. Also, the concentration of *n*-dodecane preserved in the first experiment is slightly higher than those subsequently. Although the measured values are close to each other, there seems to be a difference between the first experiment such that accumulated deposits attract more deposition, mainly on the bottom plug, presumably by condensed-phase pyrolysis reactions. It is considered that thermal stressing of *n*-dodecane at 450°C for 4 hours represents a very severe thermal stressing which can mask the effect of different surfaces on solid deposition. Lower temperature and shorter duration of stressing will be carried out in the future.

Conclusions

High surface area activated carbons PX-21 and Maxsorb 92-11A, 94-06, and 94-20 have strong effect on decomposition reactions during thermal stressing of *n*-alkanes at high temperatures, 425°C and 450°C. = The surface area as well as the surface functionalities are the two most important parameters that influence the carbon activity. The higher the surface area of activated carbon, the more prominent is the effect of activated carbon used. However, activated carbons with very high surface area (over 2000 m^2/g) do not differ in their performance during thermal stressing.

The addition of hydrogen donor decalin showed that the active carbon surfaces catalyze hydrogen-transfer reactions. The treatment of activated carbon at high temperature in N_2 atmosphere leads to removal of oxygen complexes on the carbon surfaces. Outgassed carbons showed a higher activity during thermal stressing of *n*-dodecane at 450°C for 1 h, but lower activity at 450°C for 4h stressing compared to original carbons. Oxidation of PX-21 decreases its effectiveness in stabilizing *n*-dodecane.

The carbonaceous solid deposited on the carbon surfaces during thermal stressing also plays a catalytic role, which is attributed to specific oxygen functionality on the carbon overlayer as well as adsorbed species. The surface area and porosity of activated carbon measured before and after thermal stressing with *n*-alkanes showed that carbonaceous solid deposited on the carbon surfaces as well as extraction of original carbon in toluene leads to a sharp decrease of N_2 BET surface area. While the meso- and/or macroporosity of activated carbons covered with carbonaceous solid is blocked selectively during thermal stressing, extraction decreases the porosity of the carbon uniformly due to adsorption of small amounts of toluene. The N_2 adsorption isotherms are type I, which is characteristic of microporous solids, and they do not exhibit hysteresis, indicating absence of considerable mesoporosity.

The 316 stainless surface of the reactors coated with carbonaceous deposits appears to attract more deposition, especially in the bottom plug, than that obtained on a clean metal surface. Presumably, condensed-phase pyrolysis reactions are responsible for the observed increase in the amount of carbonaceous deposits collected on a carbon coated metal surface.

References

1. K. Gergova, S. Eser, R. Arumugam, and H. H. Schobert, Effect of High Surface Area Activated Carbon on Thermal Degradation of Jet Fuel, Proceedings of the 5th

International Conference on Stability and Handling of Liquid Fuels, Rotterdam, the Netherlands, Oct. 3-7, pp. 227-240, 1994.

2. H. H. Schobert, S. Eser, C. Song, P. G. Hatcher, A. Boehman, M. M. Coleman, Advanced Thermally Stable Jet Fuels, Technical Progress Report, 92PC92104- TPR-9.

3. G. S. Szymanski and G. Rychlicki, *Carbon* **31**, 247-257, 1993.

4. G. C. Grunewald and R. S. Drago, *Journal of Molecular Catalysis* **58**, 227-233 ` 1990.

5. D. L. Trimm, Catal. Rev. Sci. Eng. 16, 155, 1977.

6. M. C. Gardner and R. S. Hansen, J. Phys. Chem. 74, 3298, 1970.

7. O. C. Cariaso and P. L. Walker, J., Carbon 13, 233, 1975.

8. S. J. Gregg, K. S. W. Sing, Adsorption, Surface Area and Porosity, Academic Press, London, p. 285, 1982.

9. M. M. Dubinin, L. V. Radushkevich., Dokl. Akad. Nauk, SSSR 55, 331, 1947.

10. H. H. Schobert, S. Eser, C. Song, P. G. Hatcher, P.M. Walsh, M. M. Coleman, Advanced Thermally Stable Jet Fuels, Technical Progress Report, 92PC92104-TPR-2.

11. R. Venkateswaran and M. H. Back, Carbon 32, 911, 1994.

12. H. H. Schobert, S. Eser, C. Song, P. G. Hatcher, A. Boehman, M. M. Coleman, Advanced Thermally Stable Jet Fuels, Technical Progress Report, 92PC92104-TPR-11.

13. S. Brunauer, L. S. Denning, W. S. Denning, and E. Teller, J. Am. Chem. Soc. 62, 1723, 1940.

Task 4. Coal-based Fuel Stabilization Studies

Kinetic Studies of Potential Jet Fuel Stabilizers. (Contributed by Emily M. Yoon, Leena Selvaraj, Semih Eser and Michael M. Coleman)

Introduction

In a previous report, we demonstrated that THQ (1,2,3,4-tetrahydroquinoline) is the superior thermal stabilizer amongst the hydrogen donor compounds screened for jet fuels at temperatures in the range of 400-500°C [1]. Kinetic studies have now been performed on dodecane neat, dodecane/THQ mixtures, and dodecane/benzyl alcohol mixtures in the range of 400 - 500°C. The rate constants and Arrhenius parameters have been calculated.

Results and Discussions

Thermal stressing was performed on 10 mL dodecane samples with and without additives at different temperatures in the range of 400 - 500°C for the required reaction time. The liquid products were analyzed and using a Perkin-Elmer GC with a FID detector.

Figure 39 represents mole percent dodecane remaining after thermal stressing at different temperatures as a function of time for (a) dodecane neat, (b) dodecane with 10 mol% benzyl alcohol (BzOHO, and (c) dodecane with 10 mol% THQ respectively. The degradation of dodecane with or without additives increases with time as well as temperature. The rate of dodecane degradation is retarded in the presence of benzyl alcohol and THQ as shown in Figures 39 (b) and 39 (c), respectively. Figure 39 illustrates that there is a very strong temperature dependence in dodecane degradation even in the presence of THQ or BzOH.

Assuming the reaction is first-order, the following equation was used to calculate the rate constant k.

$$C_A = C_{Ao}e^{-kt} \qquad (1)$$

or

$$\ln\left(\frac{C_A}{C_{Ao}}\right) = -kt \qquad (2)$$

The concentration of dodecane (C_A) after specific degradation periods was calculated using GC data. First-order reaction, plots of in (C_A/C_{AO}) versus time should be linear with a slope equal to (-k). Figures 40, 41, and 42 represent the plot of $\ln(C_A/C_{AO})$ versus time for dodecane neat, dodecane/benzyl alcohol, and dodecane/THQ mixtures, respectively. It is observed that with the increase in temperature, the rate constant k increases significantly. From these data, apparent activation energies for each reaction were calculated. The rate constant k can be expressed in the Arrhenius form:

$$K = A\,e^{-Ea/RT} \qquad (3)$$

where E_a is the activation energy, A is the preexponential factor for the reaction, R is the gas constant, and T is the absolute temperature. The variation of k with temperature can be determined by differentiating the logarithmic form of equation 3.

$$\frac{d\,\ln k}{d\left(\frac{1}{T}\right)} = -\frac{E_a}{R} \qquad (4)$$

Plots of (ln k) versus (1/T) give a slope of ($-E_a/R$). Accordingly, activation energies E_a can be calculated. The values of E_a obtained from the data shown in Figure 43 are 58, 67 and 71 kcal/mol for dodecane neat, dodecane/BzOH and dodecane/THQ mixtures, respectively. The activation energy increases in the order of $E_{a;Dod}<E_{a'Dod+BzOH}<E_{a'Dod+THQ}$. Table 3 summarizes the values of the rate constant k, activation energy E_a, and preexponential factor A. The rate constants decrease in the order of $K_{Dod}>k_{Dod+BzOH}>k_{Dod+THQ}$. The preexponential factor increases in the same order as activation energy. These kinetic results show that the dodecane degradation is retarded in the presence of BzOH, and even further in the presence of THQ.

Additionally, rate constants and Arrhenius parameters for THQ degradation in dodecane have been calculated. Figure 44 shows the mole% THQ remaining after thermal stressing in the dodecane/THQ mixture as a function of Temperature. Note that THQ degradation also increases with time and temperature. Note that THQ degradation were obtained from the data show in Figure 45 , and the activation energy and preexponential factor for THQ degradation in figure 46.

The above results are now being carefully analyzed and a paper is currently being prepared.

References

1. Yoon, E.M., M.M. Coleman, and C. Song, *Advanced Thermally Stable Jet Fuels*, Technical Progress Report, 92PC92104-TPR-12, August , 1995/

Task 5. Exploratory Studies on the Direct Conversion of Coal to High-Quality Jet Fuels.

1. Exploratory Studies on the Possibility of Non-Radical Hydrogen Transfer under Low Temperature Liquefaction Conditions. (contributed by Shona Martin)

Introduction

As reported previously [1,2], the observation that in the presence of solvent gaseous hydrogen reacts preferentially with coal under low-temperature conditions, has led to the concept of non-radical hydrogenation under certain conditions. To date, a series of experiments has been undertaken to compare the effect of demineralization on coal conversion at low temperatures (*ca* 350°C), where preliminary results indicated that conversions were comparable upon demineralization. The aim of the work reported thus far was to evaluate the nature and distribution of coal mineral matter in both untreated and treated (demineralized) samples of Wyodak coal, and consider the influence of these compounds by assessing their possible catalytic effect.

It is well documented that low-rank coals contain substantially more organic oxygen than bituminous coals; a significant part of the organic oxygen is present as carboxylic acid and phenolic groups. Further, low-rank coals contain both discrete minerals, such as quartz, pyrite, calcite, clays, and substantial amounts of inorganics associated with the organic structure. The organic bound mineral matter is present in cations in carboxylic acid salts, such as $-COO^-M^+$, $-COO^-M^{2+}OH$, or $-(COO^-)_2M^{2+}$, where M is an alkali or alkaline earth metal. The relative concentrations of these metals depend upon the geographical location of the coal.

These mineral and inorganic species can act as catalysts or poisons during liquefaction depending on reaction conditions. Mineral matter is known to act as a catalyst for coal hydrogenation, mainly owing to its pyrite content, which exhibits dual properties; one as a heterogeneous catalyst, the other giving rise to H_2S which in turn can act as a homogeneous catalyst. Under hydrogenation conditions, sulfur liberated in the transformation from pyrite to pyrrhotite, in the form of hydrogen sulfide, plays a catalytic role in hydrogen transfer by stabilizing the radicals from the thermal breakage of the coal matrix. This H_2S effect has been reported elsewhere, with high conversion yields obtained in spite of mild conditions when high sulfur coals are hydrotreated in an excess of hydrogen [3]. Moreover, Fe is known as a good catalyst for coal hydrogenation and is added in the form of a wide variety of precursors, e.g. $FeSO_4$, $Fe(CO)_5$, and Fe_2O_3. Thus Fe present in coals, predominantly in the form of pyrite, should possess a certain degree of catalytic activity. More recently, Maldonado-Hodar et al. [4] concluded that mineral matter activity in coal hydrogenation could be mainly attributed to pyrite content.

Several authors have observed a favorable influence of demineralization on coal depolymerization. Mochida et al. [5] attributed this enhanced reactivity to elimination of calcium carbonate deposition, which in turn favors good contact between demineralized coal and the hydrogen-donor solvent, in effect shortening the liquefaction time. Serio and co-workers [6] conducted a study on the effect of coal pretreatment in direct liquefaction, on a series of coals ranging from lignite, subbituminous and bituminous. They reported that the two low-rank coals (including Wyodak) modified by demineralization showed notable improvements in liquefaction yields as measured by the relative amounts of toluene solubles, oils and pyridine solubles. Further, they deduced that the extent of retrograde reactions for low-rank coals (lignite and subbituminous) was significantly reduced upon demineralization.

In another study, Joseph et al. [7] found that exchangeable alkali and alkaline earth metal cations such as Na^+, K^+ and Ca^{2+} reduced conversion and product quality during liquefaction of a Wyodak subbituminous coal and a North Dakota lignite. They attributed this adverse effect, which increases in the order $Na^+ < K^+ << Ca^{2+}$, to these cations inhibiting hydrogen transfer from the donor solvent or H_2 gas to the coal free radicals, thus promoting retrogressive reactions. From Table 4, Wyodak contains significant amounts of calcium, with the concentrations of other cations being considerably lower. Serio et al. [6] reported Ca concentrations of 1.09 and 0.04 wt% for raw and demineralized Wyodak samples, respectively. Indeed, low-rank coals often have higher concentrations of Ca and Mg, which are generally ion-exchanged on carboxyl groups in high oxygen coals.

Experimental.

All relevant details for liquefaction experiments completed to date have been reported previously [1,2].

Results and Discussion.

Table 5 summarizes the preliminary liquefaction results completed thus far. It is clearly demonstrated that demineralization has no seriously detrimental effect on liquefaction under such conditions. There are similarities between these results and those of Serio et al. [6], who also reported increased conversion for low-rank coals following demineralization. Indeed, in terms of liquid product distribution, the best results are obtained in the presence of 1-methyl- naphthalene (non-donor solvent), suggesting that hydrogenation may have been facilitated by gaseous H_2. However, this remains to be proven. Nevertheless, it raises questions as to possible hydrogenation mechanisms. Joseph [7] ascribed this phenomenon to cations inhibiting hydrogen transfer from donor solvent/gaseous hydrogen to free radicals, in effect promoting retrogressive reactions. Therefore, could it be that the absence of these species allows for better access for gas-phase H_2?

Summary

Previous FTIR and ^{13}C NMR results indicated that at temperatures such as 350°C, coal conversion was not mineral matter catalyzed [2]. This has been confirmed by consideration of the possible catalytic activity of certain mineral species. Currently, both treated and untreated Wyodak samples have been submitted for major and minor elemental analysis, allowing determination of the mineral distribution of interest in this study. Moreover, it will provide information on whether the concentrations of ion-exchangeable cations (Ca, Mg, Na, K) have been significantly reduced upon demineralization, i.e. how "effective" the demineralization has been, allowing better control over the future demineralized samples. Further thermal liquefaction tests on untreated coal are being conducted at lower temperatures and higher pressures to evaluate the threshold conditions for preferential gas-phase H_2 reactivity.

References:

1. S.C. Martin, H.H. Schobert Advanced Thermally Stable Jet Fuels, Technical Progress Report, 92PC92104-TPR-11, p74
2. S.C. Martin, H.H. Schobert Advanced Thermally Stable Jet Fuels, Technical Progress Report, 92PC92104-TPR-12, p35
3. Garcia, A.B., Schobert, H.H. Fuel **68**, 1613 (1989)
4. Maldonado-Hodar, F.J., Rivera-Utrilla, J., Mastral-Lamarca, A.M., Ferro-Garcia, M.A. Fuel **74**(6), 818 (1995)
5. Mochida, I., Yufu, A., Sakanishi, K., Korai, Y. Fuel **67**, 114 (1988)
6. Serio, M.A., Solomon, P.R., Kroo, E., Bassilakis, R., Malhotra, R., McMillen, D. Am. Chem. Soc., Div, Fuel Chem., Prep. **35**(1), 61 (1990)
7. Joseph, J.T., Forrai, T.R. Fuel **71**, 75 (1992)
8. Penn State Coal Sample Bank and Database.

2. The Study of Coal Using Low-Temperature Hydrogenation in Presence of Hydrogen-Donor Solvents (Contributed by Elena Korobetskaya)

Introduction

As was stated in the last report, Pittsburgh No. 8 coal does not seem to react with molecular hydrogen at temperatures below 300°C. This result confirms the statement that for hydrogenation of coal it is necessary to use atomic hydrogen or protons formed during some reactions (Aronov, 1960). For example, some kinds of organic solvents (tetrahydronaphthalene, 9,10-dihydrophenanthrene, dihydropyrene) might play the role of hydrogen-donors during the hydrogenation process. Possible mechanism of the donation process is:

$$\{\mathrm{COAL}\}-\mathrm{CH_2}-\mathrm{CH_2}-\{\mathrm{COAL}\} \xrightarrow{\mathrm{300\hat{}C}} 2\,\{\mathrm{COAL}\}-\mathrm{CH_2}^*$$

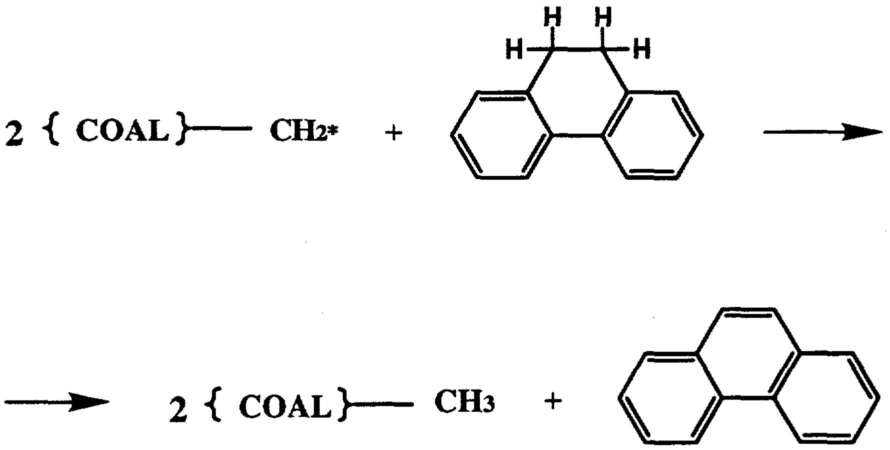

In the presence of gaseous molecular hydrogen the following reaction might occur:

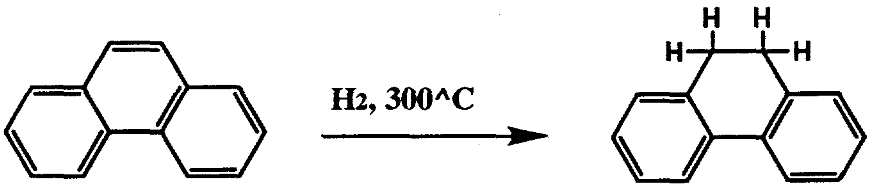

Undoubtedly this reaction could not occur, or it will occur very slowly, without a catalyst. If the catalyst was not added to the system, possibly some kinds of natural catalysts contained in coals speed up the reduction of phenanthrene. One of the possible catalyst in this case is FeS_2 which is originally present in coal mineral matter.

$$\mathbf{FeS_2 \longrightarrow FeS}$$

FeS is a compound that could be formed from FeS_2. This compound could be the catalyst for the process of transformation phenanthrene to 9,10-dihydrophenanthrene.

In the type of process discussed above radicals are formed in coal by breaking C–C bonds by heating; these radicals are stabilized by hydrogen which is produced from the reaction of dehydrogenation of 9,10-dihydrophenanthrene (hydrogen-donor solvent). Phenanthrene is formed during this reaction; and then phenanthrene reduces to 9,10-dihydrophenanthrene by molecular hydrogen.

The experiments which are presented in this section are based on the mechanism of hydrogenation discussed above.

Method and materials

Two coal samples with different rank were used for the experiments: Pittsburgh # 8 (DECS-12, hvAb rank) and Wyodak (DECS-8, subC rank). The experiments were carried out at 300^C. The samples were pressurized by molecular hydrogen in the batch reactors. The starting pressure in the reactors were:

Reactor # 1 (DECS-12) - 1150 psi;
Reactor # 2 (DECS-8) - 890 psi

Time of reactions was 30 min. 9,10-dihydrophenanthrene was used as a hydrogen-donor solvent. No catalyst was used for the experiment. Changes of the pressure during the reaction are presented in Figure 47.

The residues were investigated by CP/MAS NMR spectroscopy. Spectra are presented in Figures 48–51.

Results

CP/MAS NMR spectrum of original Pittsburgh # 8 coal sample is presented in Figure 48. There are two big peaks on the spectrum—aromatic and aliphatic. The spectrum approximately shows 30.7% of aliphatic and 65.7% of aromatic carbon. The aromatic peak consists of two smaller peaks—128 ppm and 160 ppm. The peak at 128 ppm corresponds to benzoid rings; the peak at 160 ppm corresponds to oxygen-substituted aromatics.

Figure 49 shows the spectrum of the residue from Pittsburgh # 8 coal sample that was treated with molecular hydrogen at 300°C in presence of 9,10-dihydrophenanthrene as a hydrogen-donor solvent. There are also aliphatic and aromatic peaks on spectrum. The percentage of aliphatic carbon is 36.2%; percentage of aromatics is 60.3%. As in Figure 48 there is a peak at 128 ppm which corresponds to benzoid rings, still there are some oxygen-substituted aromatics but percentage of this kind of aromatics is reduced from 3.6% (original coal, Fig. 48) to 3.4% (treated sample, Fig. 49).

CP/MAS NMR spectrum of original Wyodak coal sample is presented in Figure 50. Again there are two peaks corresponding to aliphatic and aromatic structures. The percentage of aromatics in this coal sample is 50% (peak at 128); also there is the peak corresponding to oxygen-substituted aromatics, the percentage of these compounds being approximately 10%. The percentage of aliphatics in the original coal is 39%

The spectrum of the sample of Wyodak coal that was treated in the same way as Pittsburgh # 8 coal sample, is presented in Figure 51. The percentage of aliphatics in this sample is 40.7%. Percentage of aromatics is 56%; percentage of oxygen-substituted aromatics is reduced from 10% (original coal, Fig. 4) to 3% (treated sample, Fig. 5).

It is clear from the spectra (Figures 48-49) that there is a conversion of structure from aromatic to aliphatic during the heating of coal samples under hydrogen pressure with hydrogen-donor solvent. Average reduction of aromatics in this process is 5%. Increase of aliphatic percentage of Pittsburgh #8 coal sample is 6%. Reduction of oxygen-substituted aromatic contents is 0.2% for Pittsburgh #8 coal sample and 7% for Wyodak coal sample. The spectra of Wyodak coal samples (Figures 50-51) show a strange behavior: the amount of aliphatics is still increased (but not so much as in Pittsburgh # 8 sample), but the amount of aromatics unexpetedly increases in contrast to the decrease of aromatic peak in Pittsburgh # 8 sample. The reason of such behavior might be following: there is a conversion of structure from aromatic to aliphatic, but there is the possibility that part of aliphatic structure become small enough (on a molecular scale) to form gaseous products. In this case the amount of aliphatics in the solid residue becomes smaller, and the comparative percentage of aromatics in the spectrum becomes larger. It seems to be possible that this explanation may be a clue to such behavior of coal in the NMR spectra.

Conclusions

It could be stated that 9,10-dihydrophenanthrene allows the process of hydrogenation to occur at 300°C without a catalyst. The average percentage of aromatics converted during hydrogenation is 5%. The effectiveness of the hydrogenation process at given conditions probably increases with decreasing rank of coal (Pittsburgh #8 is high volatile bituminous coal, Wyodak is subbituminous coal): low-rank coal produces a larger amount of low molecular weight aliphatic molecules than high rank coal.

3. Hydrogenation / Dehydrogenation of Polycyclic Aromatic Hydrocarbons using Ammonium Tetrathiomolybdate as Catalyst Precursor (Contributed by Richard Dutta).

Abstract

The hydrogenation and dehydrogenation behavior of naphthalene, phenanthrene, and pyrene was investigated via their product distribution and kinetic and thermodynamic parameters. Hydrogenation reactions were carried out in 25 mL microautoclave reactors at 350, 400, and 450°C for various times up to equilibrium conditions. A global kinetic model was used to determine forward and reverse rate constants, which were then used to determine Arrhenius parameters. Enthalpy data were obtained and compared to values calculated in the literature. It was found that the temperature where dehydrogenation became favorable over hydrogenation reactions decreased with increasing ring size. This was also shown by an increasing thermodynamic control over the reactions as ring size increased.

Introduction

Coal liquefaction can be considered a technically viable alternative for the production of liquid transportation fuels if the coal macromolecule can be broken up into low molecular weight fragments, and the fragments can then be hydrogenated to decrease the concentration of aromatics and heteroatoms (nitrogen, sulfur, and oxygen) in the final product. The liquefaction process can be facilitated using various sulfided catalysts, which are generally resistant to poisoning by heteroatomic compounds. Derbyshire [1,2] and Mochida [3] have reviewed the extensive literature on this subject. Research by McMillen et al. [4-6] has brought about a greater understanding of the hydrogen-transfer mechanism involved in the coal dissolution process. However, the exact role of the catalyst is still under question. The catalyst is thought not to participate in bond cleavage directly. The breaking of these bonds in the coal macromolecule is generally considered to be a thermally driven process. However, the use of a catalyst, along with a hydrogen-donor solvent, does improve conversion to liquid products. In fact, if the coal is relatively easy to convert, a catalyst will improve conversion even without a good donor solvent being present [7]. Therefore, research into catalyst development and the effects of catalysts on coal dissolution and upgrading of primary products is an important component of coal liquefaction development.

Molybdenum has long been a focus of research into catalytic coal liquefaction. In a recent historical essay, Moulijn and colleagues have traced the use of sulfided molybdenum catalysts for coal conversion back at least to 1924 [8]. The use of dispersed molybdenum catalyst in a pilot plant has been reported by Moll [9]. Liquefaction improves with an increase in molybdenum concentration, but limits have been observed beyond which further increases in molybdenum addition no longer have a significant effect [10-12]. Because the catalytically active form, MoS_2, is insoluble, a dispersion of molybdenum onto coal particles is often effected using so-called catalyst precursors. The precursors are soluble compounds of molybdenum that may have little or no catalytic activity themselves but are presumed to convert to a catalytically active form at liquefaction temperatures. Ammonium heptamolybdate (AHM) has been used in liquefaction research [1,13,14]. Derbyshire et al. [1,8,14] produced ammonium tetrathiomolybdate (ATTM) by sulfiding AHM with H_2S. They observed higher conversions using this precursor instead of AHM. The mechanism by which ATTM decomposes to its active form, MoS_2, has been studied by Prasad [15], and later by Naumann [16]. The latter work describes the decomposition of ATTM to amorphous MoS_2 in the temperature range of 350–450°C. Work by Romanowski discusses the rapid decomposition of ATTM under hydrogen atmosphere [17].

In our laboratory, the most recent work showing the effectiveness of ATTM in coal liquefaction is that by Burgess [18] and by Huang [7]. Through careful coal selection, it was shown that coal conversions of up to 95% could be achieved in catalytic reactions, although the hexane-soluble oils produced in the process still remained aromatic. The aromatics in the coal liquids have to be removed if they are to be used for liquid transportation fuels. In the United States, the 1990 Clean Air Act amendments have significantly restricted the allowable concentrations of aromatic compounds in gasoline and diesel fuels [19]. Coal may be the preferred feedstock for advanced generation jet fuels that would be able to withstand severe thermal stressing without decomposing to carbonaceous solids. However, aromatics have been shown to be precursors to solid deposition in fuels at elevated temperatures [20-22]. Upgrading processes would have to be employed to hydrogenate the aromatics produced during liquefaction. This step would involve catalytic hydrotreating of the primary liquid products from coal. However, if capital investment and operating costs coal-to-liquids plant are to be kept to a minimum, it would be advantageous to hydrogenate as many of the coal fragments as possible during the liquefaction step itself; that is, as the coal fragments are released during the depolymerisation of the coal macromolecule.

Various strategies have been formulated for application of temperature during liquefaction. These strategies are concerned with optimizing depolymerisation of coal, upgrading primary products, and avoiding retrogressive reactions. The retrogressive reactions represent the recombination of reactive free radicals to form a carbonaceous char that resists further reaction. Such reactions are often the result of the fact that the rate of hydrogenation—specifically, hydrogen capping of free radicals generated from thermal cleavage of coal macromolecules—cannot catch up to that of free radical formation. In temperature-staged and temperature-programmed liquefaction, a low-temperature pretreatment stage is followed by a high-temperature reaction stage. Conditions during the second stage are responsible for the quality of the coal liquids produced. With careful "fine tuning" of the reaction conditions, it could be possible to have advantageous thermodynamics in the system along with reasonably fast kinetics of depolymerisation of the coal macromolecule. Basically, a trade-off between kinetics and thermodynamics is possible.

Because of the complexity of the macromolecular structures of coals, the likely existence of numerous parallel reactions during liquefaction, and the production of dozens of individual compounds in the coal-derived liquids, research into the effect of various reaction conditions is facilitated by model compounds. Hydrogenation of aromatics has been studied for many years and the available literature is vast. It has been reviewed by Moreau [23], Girgis [24] and Stanislaus [25] The research has focused on kinetic, thermodynamic and product distribution analysis. Correlations among the reactivities of two-, three-, and four-ring compounds are lacking. Recently, Korre et al. [26] studied the hydrogenation of aromatics using $CoMo/Al_2O_3$ as catalyst. Categories of naphthalenic and phenanthrenic hydrogenations were introduced and comparisons of the kinetic data and equilibria were given. However, only one temperature was employed in that investigation. An investigation of temperature effects is vital if hydrogenation/dehydrogenation reactions are to be studied and optimised.

This section will discuss the hydrogenation and dehydrogenation reactions of naphthalene, phenanthrene and pyrene using ATTM as the catalyst precursor. The motivation for this work stems from previous work in our laboratory on the behavior of a variety of polycyclic compounds, aimed at investigating some of the fundamental chemical processes involved in various aspects of fuel utilization. These include direct coal liquefaction [7,18] stability of aviation fuels [20-22] and carbonization or graphitization reactions leading to carbon materials [27]. Recent work on the liquefaction behavior of resinite during coal liquefaction [28,29] also motivated the present research on model compound hydrogenation and dehydrogenation.

Experimental

All reactions were carried out in 25mL microautoclave reactors (made of type 316 stainless steel). In all runs, 3±0.01g reactant (Aldrich, 99%, used as received) and 0.075±0.005g ammonium tetrathiomolybdate (Aldrich, used as received) were weighed into the reactor. The reactor was then purged with hydrogen twice, before the final pressurization with hydrogen to 7MPa. Heating was accomplished by lowering the reactor into a fluidized sand bath preheated to the desired temperature. After a measured reaction time, the reactor was removed from the sandbath and quenched to room temperature by immersing it in a cold water bath. The products from the reaction were removed from the reactor using tetrahydrofuran (THF). The THF was removed by rotary evaporation and the product was weighed. It was found that in all cases the weight of the products equaled the weight of the original compound before reaction. The products were dissolved in acetone and analysed using a Perkin-Elmer 8500 gas chromatograph (column used was 30m x 0.25mm i.d. fused silica capillary colum (DB-17) coated with 50% phenyl - 50%

methylpolysiloxane with a coating film thickness of 0.25 µm). Identification of the products was achieved using a Hewlett-Packard 5890II gas chromatograph coupled with a HP 5791A mass selective detector.

In order to determine the dehydrogenation behavior of the hydrogenated pyrenes, the products from pyrene hydrogenated at 350°C and 60 minutes, 400°C and 80 minutes, and 450°C and 40 minutes, were catalytically dehydrogenated under N_2. This was accomplished using the same reactors as in the hydrogenation step. The products from the three hydrogenations listed above were weighed into the reactor along with a 1 wt% (metal) loading of ATTM. The reactor was pressurised with approximately 3MPa N_2 and immersed in a sand bath at the desired temperature and for the desired reaction time. After this time, the reactor was quenched as before, and the products were removed using THF. The products were analysed using GC as before. The dehydrogenation behavior of tetralin was investigated in a similar way to the hydrogenated pyrenes.

Results and discussion

We begin with the simple equation considering an equilibrium between aromatics and hydroaromatics:

$$\text{Aromatics} + n\,H_2 \rightleftharpoons \text{Hydroaromatics} \qquad (1)$$

Equation 1 is the basis for calculating the reaction kinetics. To simplify the system, two assumptions are made: (1) the forward reaction is pseudo-first-order; (2) The reverse reaction is first order in hydroaromatics.

The rate expression is then given by:

$$-d[A] / dt = k_f [A] P_{H_2}{}^{n} - k_r [HA] \qquad (2)$$

where: k_f and k_r are the forward and reverse rate constants, respectively, and P_{H_2} is the hydrogen partial pressure.

Assumption 1 is introduced, and the equation (2) becomes:

$$-d[A] / dt = k_f [A] - k_r [HA] \qquad (3)$$

At equilibrium $k_f [A] = k_r [HA]$, and therefore:

$$k_f / k_r = [HA]_{eq} / [A]_{eq} \qquad (4)$$

Also, a mass balance gives:

$$[A]_t + [HA]_t = [A]_{eq} + [HA]_{eq} \quad (5)$$

Therefore, using equations (4) and (5), equation (3) can be rearranged to give:

$$-d[A] / dt = k_f (1+[A]_{eq}/[HA]_{eq}) ([A]_t - [A]_{eq}) \quad (6)$$

By putting $K_R = k_f (1+[A]_{eq}/[HA]_{eq})$, and integrating, the final expression becomes:

$$\ln [A]_t - [A]_{eq} / [A]_0 - [A]_{eq} = -k_R t \quad (7)$$

Therefore a plot of equation (7), gives slope = $-k_R$, and therefore:

$$k_f = \text{slope} / (1+[A]_{eq} / [HA]_{eq}) \quad (8)$$

$$k_r = k_f [A]_{eq} / [HA]_{eq} \quad (9)$$

Arrhenius Plots

The Arrhenius equation was used to determine how the rate constants vary with temperature. By plotting $\ln k_f$ and $\ln k_r$ vs $1/T$, activation energies for hydrogenation and dehydrogenation were obtained. Also, the intersection of the two lines is the point where the rates of hydrogenation and dehydrogenation are equal. This is the boundary beyond which unfavorable dehydrogenation conditions predominate over favorable hydrogenation conditions.

Equilibrium considerations

$$K_p = [HA]_{eq} / [A]_{eq} \,.\, 1/PH_2{}^n \quad (10)$$

where n is the number of moles of hydrogen added in a given reaction e.g. naphthalene + $2H_2 \rightarrow$ tetralin (n=2); phenanthrene + $4H_2 \rightarrow$ octahydrophenanthrene (n=4).

Using the van't Hoff isochore equation (equation 11),

$$d \ln K_p / dT = \Delta H / RT^2 \quad (11)$$

the enthalpy of hydrogenation for each reaction can be calculated. By definition, this value should be equal to the difference in the activation energies for the forward and reverse reactions.

Naphthalene hydrogenation/dehydrogenation

Figure 52 shows the product distribution for naphthalene hydrogenation as a function of time at three temperatures. Tetralin was the only hydrogenation product observed. This behavior is consistent with literature reports citing the relative ease of hydrogenation to tetralin but much greater difficulty of proceeding to the decalins [30,31]. Cracking or isomerisation products of tetralin were seen at 450°C, but total concentration did not exceed 5 wt%. At 400°C and 450°C, equilibrium is reached after 60 minutes reaction time. Total conversion is slightly better at 400°C. At 350°C, the reaction does not reach equilibrium; after 180 minutes, the conversion reached 72%. To calculate the equilibrium composition of the reaction at 350°C, an extrapolation was used to find the point of 95% conversion.

Figure 53 shows a kinetic plot of equation (7) for naphthalene hydrogenation. It can be seen that the data fit the model well. Using equations (8) and (9), rate constants were calculated, and are reported in Figure 53.

Figure 53 shows that as temperature increases, k_f increases. The dehydrogenation rate constant, k_r also increases with increasing temperature, but the activation energies (Ea) of the two reaction are different. Figure 54 shows an Arrhenius plot for naphthalene hydrogenation/dehydrogenation. From regression analysis, calculated apparent activation energy for the forward reaction is 13 kcal/mol, and activation energy for the reverse reaction is 36 kcal/mol. Figure 54 also shows that dehydrogenation becomes the favorable reaction above 450°C.

To confirm this observation experimentally, tetralin was catalytically dehydrogenated under nitrogen atmosphere at 350, 400 and 450°C. Figure 55 shows the product distribution. It can be seen that at 350 and 400°C (30 minutes reaction), conversions of tetralin to naphthalene are 10 and 20% respectively. At 450°C, conversion increases to 55%, for the same reaction time. Therefore, these data confirm that dehydrogenation is the major reaction at only high temperatures (>450°C). This has also been shown in our laboratory with research on the thermal stability of tetralin. It was shown that tetralin was stable to decomposition and dehydrogenation at 450°C [32].

The use of tetralin as a donor solvent in coal extraction and liquefaction has been studied in detail for many years. A comprehensive review of the earlier work is given by Kiebler [33]. Several useful but more recent studies are also available [34-37]. Data derived by Hooper et al.[36] show that formation of naphthalene from tetralin only occurs at temperatures greater than 435°C, and show a pronounced increase in dehydrogenation at 450°C. These results agree quite well with the earlier work of Peter, who found tetralin decomposition up to 38% for reactions at 440°C and 1 hour [38]. The kinetics of the reaction are slower than the present work because these authors used only thermal (i.e., non-catalytic) conditions. However the thermodynamic behavior is similar to that seen from the data obtained in the present study. It can be argued that the point where the two reaction are equal is the temperature that a H-donor solvent is most effective. This would be about 450°C for the naphthalene/tetralin system.

Figure 56 shows a van't Hoff plot for hydrogenation of naphthalene to tetralin. Because of the uncertainty of behavior at higher temperatures, two lines were plotted. One included the data at 450°C, and the other did not. Therefore a range of values was obtained. Kp values were calculated using equation (10). Equation (11) was used to calculate the enthalpy of hydrogenation. A range of -25±5 kcal/mol is obtained from Figure 56. This compares reasonably well with the value obtained from the difference in the activation energies of the forward and reverse reactions (23.5 kcal/mol). The value is also in reasonable agreement with literature values of –29.8 and –32 kcal/mol [39,40].

Kinetics vs thermodynamics: naphthalene

If hydroaromatics are to be produced from aromatics, two factors have to be considered: (1) conversion; (2) length of time to reach the desired conversion level.

As can be seen from the data, conversion decreases with increasing temperature, but the kinetics of the reaction are slower at lower temperatures. From the data, it can be concluded that high temperatures are desirable for the first forty minutes of reaction, but after this time thermodynamics limit the conversion. At this point, it is then advisable to reduce the temperature to below 400°C, and continue to convert naphthalene to tetralin, as can be seen in the reaction at 350°C. To hydrogenate only at 350°C would take too long to achieve respectable conversion. These results suggest that a concept of "reverse temperature staging", in which an initial, high-temperature stage is followed by a second, low temperature reaction stage, may be of benefit in achieving high yields of hydrogenated products from the liquefaction step itself.

Phenanthrene hydrogenation/dehydrogenation

Figure 57 a, b and c shows the product distributions for phenanthrene hydrogen-ation at 350, 400 and 450°C, respectively. The figures show decreasing conversion as temperature increases. Also, product selectivity differs in the three different temperature reactions. At 350°C, the major primary product is dihydrophenanthrene (DHPh). Tetrahydrophenanthrene (THPh) is also a primary product, while octahydrophenanthrene (OHPh) is a hydrogenation product of di- and tetrahydrophenanthrene. However, a maximum in the concentration of DHPh appears after 50 minutes reaction. The concentration then decreases from 28 wt% to 19 wt%. This can be attributed to the dehydrogenation pathway of DHPh to phenanthrene. This was confirmed by hydrogenating DHPh at 350°C using ATTM. Figure 58 shows that phenanthrene is the major product during this reaction. Comparing the product distribution of THPh and OHPh with that of the same compounds shown in Figure 57a, it can be concluded that THPh is a direct hydrogenation product of phenanthrene, and OHPh is a hydrogenation product of DHPh. The interconversion of DHPh and THPh [41] seems unlikely based upon the fact that the concentration of THPh is the same when phenanthrene and DHPh are used as reactants. OHPh concentration is higher when DHPh is used as the reactant, suggesting that DHPh hydrogenates to OHPh directly.

At 400°C, the concentration of DHPh reaches a maximum in thirty minutes' less time than at 350°C. This is due to greater reaction rates at the higher temperature, and unfavorable thermodynamics allowing dehydrogenation to take place more readily. At 450°C, dehydrogenation is the most favorable reaction and therefore conversion is limited to only 27%. Figure 59 shows a kinetic plot of equation (7) for phenanthrene hydrogenation. Using equations (8) and (9), the rate constants were calculated and these are reported in Figure 59.

Figure 59 shows that as temperature increases, k_f increases. The dehydrogenation rate constant, k_r also increases with increasing temperature, but the activation energies of the two reactions are different. Figure 60 shows an Arrhenius plot for phenanthrene hydrogenation/dehydrogenation. From regression analysis, calculated activation energy for the forward reaction is 6.3 kcal/mol, and activation energy for the reverse reaction is 22.8 kcal/mol. These values are low but this may be attributed to the unusually high dehydrogenation susceptibility of DHPh. It may also show that the reaction is partly controlled by diffusion processes. The crossover temperature where dehydrogenation becomes the favorable reaction is 404°C.

Figure 61 shows a van't Hoff plot for hydrogenation of phenanthrene to DHPh, THPh and OHPh. K_p values were calculated using equation (10). Data for the reaction at 350°C were not included because the susceptibility of DHPh toward dehydrogenation caused considerable uncertainty in the results. Equation (11) was used to calculate the enthalpies of hydrogenation, and these are reported in Figure 61.

It can be seen that the value of ΔH per mole of hydrogen added is almost constant for the three reactions, and that the value of –12.3 kcal/mol (for the predominant reaction of phen + $H_2 \rightarrow$ DHPh) compares well with the value obtained from the difference in activation energies of forward and reverse reactions (–12.0 kcal/mol). The values also compare well to values given in the literature (–12 kcal/mol) [42].

Kinetics vs thermodynamics: phenanthrene

Thermodynamics appear to play a more important part in the hydrogenation of phenanthrene than for naphthalene. The temperature limit for favorable conditions is much lower than for naphthalene at 404°C. Also, the difference in reaction kinetics is not so pronounced as temperature increases from 350°C to 400°C. Naphthalene rates increased almost by a factor of three, whereas phenanthrene kinetics increased by only a factor of 1.2. These observations are in agreement with the conclusions of Girgis [24] that "equilibrium considerations take on increasing importance with an increasing number of rings in fused-ring aromatics".

Pyrene hydrogenation/dehydrogenation

Figure 62a, b and c shows the product distributions for pyrene hydrogenation at 350, 400 and 450°C respectively. The major product at all temperatures is dihydropyrene (DHPy). Secondary hydrogenation products are tetrahydropyrene (THPy) and hexahydropyrene (HHPy). Conversion decreases as temperature increases as seen with the other compounds in this investigation. The product selectivity at 350°C and 400°C is similar except that at 350°C the hydrogenation of DHPy to THPy is allowed to continue after 80 minutes reaction time. Therefore, it can be seen that reverse dehydrogenation reactions are having an effect at 400°C. At 450°C, conversion of pyrene stops after 20 minutes, with only 27% conversion to hydroaromatics.

Figure 63 shows a kinetic plot of equation (7) for pyrene hydrogenation. Using equations (8) and (9), the rate constants were calculated from the plot, and reported in Figure 63.

Figure 64 shows an Arrhenius plot for pyrene hydrogenation/dehydrogenation. From regression analysis, calculated activation energy for the forward reaction is 8.5 kcal/mol, and activation energy for the reverse reaction is 17.6 kcal/mol. Figure 64 also shows that dehydrogenation becomes the favorable reaction above 372°C.

In order to confirm this dehydrogenation behavior, hydrogenated pyrenes were subjected to dehydrogenating conditions, and the concentration of pyrene was followed. Figure 65 shows that as temperature increases the amount of dehydrogenation increases. However, in contrast to tetralin dehydrogenation, lower temperatures do have a considerable effect on the dehydrogenation rate.

The use of pyrene as a hydrogen shuttler has received some attention in the literature [37,43-46]. In essence, a hydrogen shuttler is a compound that is easily hydrogenated by gaseous hydrogen, and easily transfers the acquired hydrogen to coal or coal-derived fragments in a subsequent process. Study of the hydrogenation/ dehydrogenation behavior of pyrene and hydropyrenes (particularly dihydropyrene) is a vital step in determining the overall effectiveness of pyrene or similar heavy aromatics as components of coal liquefaction solvents. The present work shows that hydropyrenes are susceptible to dehydrogenation at temperatures above 372°C. Therefore, because coal liquefaction is usually carried out at higher temperatures than this, the important consideration is not the ability of hydrogenated pyrenes to give up their hydrogen, but it is the hydrogenation reactivity of pyrene itself that will determine the effectiveness of the solvent.

Figure 66 shows a van't Hoff plot for hydrogenation of pyrene to DHPy, THPy and HHPy. Kp values were calculated using equation (10). Equation (11) was used to calculate the enthalpies of hydrogenation, and these are reported in Figure 66.

The values for ΔH per mole of hydrogen added are almost constant for the three reactions, and that the value of –6.6 kcal/mol (for the predominant reaction of pyrene + $H_2 \rightarrow$ DHPy) compares well with the value obtained from the difference in activation energies of forward and reverse reactions (–9 kcal/mol). The values also compare reasonably well to values given in the literature (–10 kcal/mol) [46].

Kinetics vs thermodynamics: pyrene

Dehydrogenation reactions of pyrene hydroaromatics predominate above 372°C. Therefore when optimising conditions for hydrogenation of pyrene, the most important variable to take into account is the temperature. Kinetics do not play an important role in the reaction, except for the early stages of conversion (first 20 minutes of reaction). These observations satisfy the earlier statement that equilibrium considerations increase with increasing ring size.

Conclusions

The main objective for this work was to be able to make comparisons for 2, 3, and 4-ring systems and try to extrapolate this behavior to larger ring systems. From a kinetic standpoint, it appears that the rate of reaction is most important for bicyclic compounds. As ring size increases, kinetics play a less important role, and thermodynamics becomes the driving force for the outcome of the reaction. In fact, the data for pyrene show that even at the low temperature of 372°C, dehydrogenation reactions predominate. This would imply that if even larger ring systems are hydrogenated, equilibrium considerations will become even more important.

This shift in relative importance of thermodynamic and kinetic considerations can be attributed in part to the heats of formation of the various polycyclic compounds and their hydrogenated species. Shaw et al. [47] have reported these values. From their data, a clear trend of increasing thermodynamic control over hydrogenation reactions with increasing ring size is apparent. Figure 67 shows a comparison of enthalpy data from the present work and Shaw's data. It can be seen that there is a good correlation between the data. The figure also shows the following thermodynamic trends. When adding 1 mol H_2, dihydrophenanthrene is more readily formed than dihydropyrene. When adding 2 mol H_2, tetrahydronaphthalene is more readily formed than tetrahydrophenanthrene, which is more readily formed than tetrahydropyrene.

In terms of coal liquefaction, temperature effects are very important when hydrogenating three- and four-ring systems, whereas the kinetics of hydrogenation of two-ring systems are very important. Therefore, a trade-off between kinetics, thermodynamics and product selectivity is necessary. A significant question to be asked when determining a coal liquefaction process is the type of product is required. If it is desired to convert coal not simply to a synthetic crude oil, but rather to some specific product slate, then the coal has to be selected on a basis of its molecular architecture. For example, a product that requires a large concentration of tetralin and decalin, a coal-derived jet fuel for example, would need a feedstock in which bicyclic components dominate in its structure. Conditions for liquefaction can then be determined to match the desired reaction chemistry of the selected feedstock. Data from this work suggest that the important factor will be depolymerisation kinetics, and subsequent hydrogenation kinetics. A product that requires larger ring structures as part of its composition would require a coal that has these large polycyclic moieties as part of its structure. Our data suggest that if hydrogenation of the fragments is to take place, the temperature of the reaction would have to be selected carefully. A possible reaction strategy for consideration in the future, particularly for direct production of high yields of hydroaromatic or fully hydrogenated compounds, would be a reverse temperature program that would have a low-temperature final stage to avoid dehydrogenation reactions.

References

1. F. J. Derbyshire, Catalysis in Coal Liquefaction: New Directions for Research., IEA Coal Research, London, IEA CR/08, 1988.

2. F. Derbyshire, Energy Fuels, 3 (1989) 273.

3. I. Mochida and K. Sakanishi, in D. D. Eley, H. Pines and W. O. Haag (Editors), Advances in Catalysis, Vol. 40, Academic Press, San Diego, 1994, p. 39.

4. D. F. McMillen, R. Malhotra, S.-T. Chang and S. E. Nigenda, Am. Chem. Soc., Div. Fuel. Chem., 1985, 30(4), 297.

5. D. F. McMillen, R. Malhotra, G. P. Hum and S.-J. Chang, Energy Fuels, 1 (1987) 193.

6. D. F. McMillen, R. Malhotra, S.-J. Chang, W. C. Ogier, S. E. Nigenda and R. H. Fleming, Fuel, 66 (1987) 1611.

7. L. Huang, PhD dissertation, 1995, The Pennsylvania State University, University Park, PA.

8. J. A. Moulijn, P. W. N. M. van Leeuwen and R. A. Santen, in J. A. Moulijn, P. W. N. M. van Leeuwen and R. A. Santen (Eds.), Catalysis: An Integrated Approach to Homogeneeous, Heterogeneous and Industrial Catalysis, Elsevier, Amsterdam, 1993, Chapter 1.

9. N. G. Moll and G. J. Quarderer, Chem. Eng. Prog., 75(11) (1979) 46.

10. F. J. Derbyshire, V. H. J. de Beer, G. M. K. Abotsi, A. W. Scaroni, J. M. Solar and D. J. Skrovanek, Applied Catalysis, 27 (1986) 117.

11. G. M. K. Abotsi, PhD Dissertation, 1987, The Pennsylvania State University, University Park, PA.

12. A. B. Garcia and H. H. Schobert, Coal Prep., 7 (1989) 47.

13. S. W. Weller, Fourth International Conference on the Chemistry and Uses of Molybdenum, 1982.

14. S. W. Weller and M. G. Pelioetz, Ind. Eng. Chem., 43(5) (1951) 1243.

15. T. P. Prasad, E. Diemann and A. J. Muller, Inorg. Nucl. Chem., 35 (1973) 1895.

16. A. W. Naumann, A. S. Behan and E. M. Thorsteinson, Fourth International Conference on the Chemistry and Uses of Molybdenum, 1982, p313.

17. W. Romanowski and E. Roczniki, Chem. II Ann. Soc. Chim. Poionorum., 37 (1963) 1077.

18. C. Burgess, PhD Dissertation, 1994, The Pennsylvania State University, University Park, PA.

19. National Research. Council. Coal: Energy for the Future, National Academy Press, Washington, 1995.

20. C. Song, Y. Peng, H. Jiang and H. H. Schobert, Prepr. Pap.- Am. Chem. Soc., Div. Pet. Chem., 1992, 37, 484.

21. C. Song and P. G. Hatcher, Prepr. Pap.- Am. Chem. Soc., Div. Pet. Chem., 1992, 37, 529.

22. C. Song, S. Eser, H. H. Schobert and P. G. Hatcher, Energy Fuels, 7 (1993) 234.

23. C. Moreau and P. Geneste, in J.B. Moffat (Ed.), Theoretical Aspects of Heterogeneous Catalysis, Van Nostrand Reinhold, New York, 1990, p256.

24. M. J. Girgis and B. C. Gates, Ind. Eng. Chem. Res., 30 (1991) 2021.

25. A. Stanislaus and B. H. Cooper, Catal. Rev.-Sci. Eng., 36(1) (1994) 75.

26. S. C. Korre, M. T. Klein and R. J. Quann, Ind. Eng. Chem. Res., 34 (1995) 101.

27. J. V. Atria, M.S Thesis., 1994, The Pennsylvania State University, University Park, PA.

28. R. P. Dutta and H. H. Schobert, Am. Chem. Soc., Div. Fuel. Chem., 1993, 38, 1140.

29. R. P. Dutta and H. H. Schobert, in K. Anderson and J. Crelling (Eds.), Amber, Resinite, and Fossil Resins, ACS Symposium Series, in press (1995)

30. F. G. Bordwell, Organic Chemistry, Macmillan, New York, 1963, Chapter 15.

31. R. Q. Brewster, Organic Chemistry, Prentice-Hall, Englewood Cliffs, N.J., 1953, Chapter 31.

32. H. H. Schobert et al., Advanced Thermally Stable Jet Fuel Development Program Anual Report, Volume II, Fuel Science Program, The Pennsylvania State University, Interim Report for Period July 1990- July 1991. p8.

33. M. W. Kiebler, in H. H. Lowry (Ed.), Chemistry of Coal Utilization, Wiley, New York, 1945, Chapter 19.

34. M. L. Penninger, Int. J. Chem. Kinetics., 14 (1982) 761.

35. J. J. de Vlieger, A. P. G. Kieboom and H. van Bekkum, Fuel, 63 (1984) 334.

36. R. J. Hooper, H. A. J. Battaerd and D. G. Evans, Fuel, 58 (1979) 132.

37. B. C. Bockrath, in M. L. Gorbaty, J. W. Larsen and I. Wender (Eds.), Coal Science, Volume 2, Academic Press, New York, 1983, p65.

38. I. Peter, Technika, 19 (1938) 193.

39. D. M. Speros and F. D. Rossini, J. Phys. Chem., 64 (1960) 1723.

40. C. G. Frye and A. W. Weitkamp, J. Chem. Eng. Data., 14 (1969) 372.

41. J. L. Lemberton and M. Guisnet, Applied Catalysis, 13 (1984) 181.

42. C. G. Frye, J. Chem. Eng. Data., 7 (1962) 592.

43. R. C. Neaval, Fuel, 55 (1976) 263.

44. I. Mochida, A. Takarabe and K. Takeshita, Fuel, 58 (1979) 17.

45. F. J. Derbyshire and D. D. Whitehurst, Fuel, 60 (1981) 655.

46. K. P. Johnston, Fuel, 63 (1984) 463.

47. R. Shaw, D. M. Golden and S. W. Benson, J. Phys. Chem., 81 (1977) 1716..

4. Noble Metal Catalysts for Low-Temperature Naphthalene Hydrogenation in the Presence of Benzothiophene. (Contributed by Shawn D. Lin and Chunshan Song)

Abstract

This work deals with low-temperature catalytic naphthalene hydrogenation as a model reaction for low-temperature hydrotreating of coal-derived liquids to produce thermally stable jet fuels. Pt/Al_2O_3, Pd/Al_2O_3, and Pd/TiO_2 catalysts were compared to a commercial hydrotreating catalyst, $NiMo/Al_2O_3$, for naphthalene hydrogenation inside tubing bombs at 553 K with a cold feed (at room temperature) of 6.99 MPa H_2 and tridecane as the solvent. The noble metal catalysts were found to be significantly more active than $NiMo/Al_2O_3$. A further study at a reaction temperature of 473K showed that naphthalene hydrogenation over these noble metal catalysts can proceed even in the presence of benzothiophene at a concentration of 4200 ppm. Sulfur addition does decrease the activity of all the noble metal catalysts. However, Pd catalysts appear to have higher sulfur resistance than the Pt catalyst; Pd/TiO_2 catalyst was found to be the most active and the least affected by benzothiophene among the three noble metal catalysts studied.

Introduction

This work is a part of our effort in an on-going program to develop advanced thermally stable jet fuels from coal-derived liquids and petroleum. Recently, due to the more and more stringent environmental regulations and fuel specifications, reduction of aromatics from distillate fuels such as diesel fuel, gasoline and jet fuel has received considerable attention. Conventional hydrotreating processes are currently used in industry for aromatic saturation [1]. Hydrogenation and partial hydrogenation of aromatic compounds are also important for producing solvents and advanced liquid fuels. In our on-going program to develop advanced thermally stable jet fuels from coal-derived liquids and petroleum, both complete and partial hydrogenation reactions of naphthalene-type compounds have important roles to play. Complete saturation of naphthalene gives decalins which show much higher thermal stability than long-chain alkanes, while partial saturation produces tetralin which can substantially inhibit the thermal degradation and solid-forming tendency of long-chain alkanes in jet fuels at high temperature [2-4].

The hydrogenation of aromatic and polycyclic aromatic compounds (that are relatively rich in coal-derived liquids and petroleum-based heavy oils) is typically exothermic [1,5]; therefore, a lower reaction temperature is thermodynamically favorable. However, in hydrotreating fuels and heavy liquids where polycyclic aromatic compounds are present, a reaction temperature above 623 K is typical in conventional processes, which consequently requires a high concentration of hydrogen to offset the limitation of thermodynamic equilibrium conversion. Noble metal catalysts are active for the hydrogenation of aromatics even at a temperature below 473K [1,6,7], but they were not used for hydrotreating purpose owing to the cost and their susceptibility to the poisoning by sulfur-containing compounds [8]. However, recent studies showed that some noble metal catalysts may not be as sensitive to sulfur as had been generally recognized [9-13]. This study attempted to examine the potential of using noble metal catalysts for low-temperature hydrotreating reaction in the presence of sulfur-containing compounds, and as a model reaction, naphthalene hydrogenation was conducted in the absence and presence of benzothiophene.

Experimental

Catalyst Preparation

Pt/Al_2O_3, Pd/Al_2O_3, and Pd/TiO_2 catalysts were all prepared by incipient wetness method using H_2PtCl_6 (Aldrich, 99.995%) and $PdCl_2$ (Aldrich, 99.995%, dissolved in ultra-pure HCl solution before use) as the precursors. The pore volume and surface area of the support are 0.8 cc/g and 200 m^2/g for γ-Al_2O_3 (Sumitomo Metal Mining, S-1, ground to 80–120 mesh size) [14] and 0.5 cc/g and 50 m^2/g for TiO_2 (Degussa, P25), respectively. The supports were calcined at 773 K under dry air flow for 2 h before use. A nominal loading of 2 wt% metal was used for all three catalysts. A commercial hydrotreating catalyst $NiMo/Al_2O_3$ (Shokubai Kasei, P-modified and presulfided) [15] was used as the reference without further pretreatment. The pretreatment of the noble metal catalyst was carried out in a flow-type glass reactor having a side arm connection to a catalyst transfer tube such that the pretreated catalyst powders can be poured into the transfer tube without exposing to the air. The transfer tube loaded with pretreated catalyst was stored under N_2 environment in a home-made glove box. The pretreatment conditions for these noble metal catalysts were H_2 reduction at 723 K for Pt/Al_2O_3, 20% O_2 calcination at 673 K for Pd/Al_2O_3, and H_2 reduction at 473 K for Pd/TiO_2; these conditions were found to give relatively higher activities for naphthalene hydrogenation at 553 K with these three noble metal catalysts[16].

Reaction Conditions

Hydrogenation was carried out using tubing bombs made from a pair of weld connectors (Swagelok, ss316) and a 1/4" tube side arm for connection to a pressure gauge and a close-off valve. The total inner volume of the bomb is approximately 25 mL. Bombs were typically loaded with 4 g tridecane (Aldrich, 99%), 1 g naphthalene (Fischer, certified grade), and in certain cases, 9 mg or 21 mg of benzothiophene (Fluka, 99%). Loading of the pretreated catalyst was performed under N_2 environment in a home-made glove box, where the bomb was subsequently sealed. Thereafter, the bomb was connected to a gas manifold via its side-arm and the atmosphere inside the bomb was replaced by hydrogen (MG Ind., 99.999%) using dilution purge, i.e., at least 8 cycles of pressurizing with H_2 to 6.99 MPa followed by a careful venting to approximately 0.45 MPa. At the completion of dilution purge, the bomb was charged with H_2 to either 6.99 MPa or 10.44 MPa, disconnected from the manifold, plunged into a fluidized sandbath (Tecam) preset to the desired reaction temperature, and the reaction was timed. The reaction temperature was typically controlled to an accuracy of 10 K. After the reaction, the bomb was removed from the sandbath and quenched in a cold water bath.

On cooling, the pressure in the tubing bomb was carefully released to prevent any entraintment of liquid in the vent gas; part of the vent gas was collected in a gas bag for composition analysis. The bomb was then opened and the liquid content was poured into a funnel with filter paper, followed by rinsing and flushing the bomb with acetone (Aldrich, 99.9%); the filtrate and the wash solution were separately stored in small vials for later analysis. The solid residue on the filter paper was dried in an oven at 393 K for at least 3 h and then weighed.

Product Analysis

The composition of the vent gas was analyzed by GC (Perkin-Elmer 5800) using a Chemipack C18 (Alltech, 1/8", 6 ft) column with FID and Carboxene 1000 (Supelco, 1/8", 15 ft) column with TCD. The gas yield and the amount of H_2 reacted were calculated from the average molecular weight of the vent gas, the bomb pressure after reaction, and the weight change before and after the bomb was vented; details of the calculation are given in the appendix. Liquid samples were quantitized by adding a known amount of n-nonane (Aldrich, 99.9%) followed by GC (HP5890II) analyses on either a DB-17 (J&W, 30mx0.25mm) or a Rtx-50 (Restek, 30mx0.25mm) capillary column with FID detector. The response factors of individual species were determined by injection of mixtures of known composition. GC-MS (HP5890II GC coupled with HP5971A MSD) equipped with the same capillary columns was used to identify the compositions in the liquid products from time to time. The sum of the liquid products in both the filtrate and the wash solution samples were used as the overall yields of liquid products. The yield of solid product was taken as the weight difference between the solid residue and the catalyst loaded in the reactor. Some of the used catalysts (i.e., recovered solid residue) were further analyzed with TGA (Mettler, TG-50) under dry air flow from 323 to 1023 K at a heating rate of 5 K/min. An overall mass balance of >90% was obtained with this kind of analysis; most experiments show an overall mass balance of >95%.

Results and Discussion

Hydrogenation at 553K

The results of naphthalene hydrogenation at 553 K over the three noble catalysts studied and the NiMo/Al_2O_3 reference catalyst are shown in Table 6. The naphthalene conversions over Pt/Al_2O_3, Pd/Al_2O_3, and Pd/TiO_2 were all above 70% in the one-hour run, compared to a 17% conversion over NiMo/Al_2O_3 at a 50% higher catalyst loading. It is clear that the three noble metal catalysts are much more active than with the NiMo/Al_2O_3 hydrotreating catalyst at this reaction condition. Also included in Table 6 are the hydrogenation results of TiO_2 and HCl treated Al_2O_3; it is obvious that the high activities of these three noble metal catalysts cannot be attributed to the support or the Cl residue in the catalysts. Besides the higher naphthalene conversions with the three noble metal catalysts, the selectivity to hydrogenated naphthalene products (dihydronaphthalene, tetralin, and decalins) and the molar ratios of hydrogen reacted to naphthalene reacted, $\Delta H/\Delta N$, are also significantly higher than the NiMo/Al_2O_3 catalyst. The calculated $\Delta H/\Delta N$ ratio for the three noble metal catalysts roughly correspond to the amount of hydrogen added to form the hydrogenated products. This indicates that the hydrogen reacted was almost all used for hydrogenation with the noble metal catalysts; whereas for NiMo/Al_2O_3 a portion of the hydrogen consumed was used in other reaction routes such as in the formation of gas products. The low yields of solid and gas products over the noble metal catalysts also indicate that the hydrogenolysis of naphthalene was not significant at this reaction condition. It is clear that the noble metal catalysts are more suitable for the low-temperature hydrogenation of naphthalene and, potentially, more suitable for the hydrotreating purposes at 553 K or lower.

It is interesting to note that the main product of the naphthalene hydrogenation is tetralin at 553 K even when the naphthalene conversion is above 90% (Table 6). This trend is similar to that for CoMo/Al_2O_3 catalyst at 623 K [17]. As both naphthalene hydrogenation and tetralin hydrogenation are exothermic reactions, a higher equilibrium yield to more hydrogenated products is expected from thermodynamic considerations when a lower reaction temperature is used. Therefore, naphthalene hydrogenation at 473 K was studied.

Hydrogenation at 473 K

The results of naphthalene hydrogenation at 473 K are shown in Table 7 for the three noble metal catalysts. It appears that under these conditions tetralin remains the only hydrogenated product, except for those runs with conversion as high as 100%. As decalins would be thermodynamically favorable at this low temperature, it implies that the formation of decalins is kinetically less favorable over the catalysts under the conditions used. However, the hydrogenation abilities of these noble metal catalysts at 473 K are clearly shown from the high selectivity to hydrogenated products, high $\Delta H/\Delta N$ ratios, and the low selectivity to gases and solids, as shown in Table 7. These results indicate that noble metal catalysts can be useful for low-temperature polycyclic aromatic hydrogenation.

In Table 7, an increase in the catalyst loading from about 0.13 to approximately 0.2 g (amount of naphthalene kept constant) significantly increased the naphthalene conversion with any of the three catalysts, Pt/Al_2O_3, Pd/Al_2O_3, and Pd/TiO_2. At 0.2 g catalyst loading, all three noble metal catalysts promoted naphthalene conversion to about 100%. However, their product selectivity patterns are different. The major products with Pd/Al_2O_3 include tetralin, and *cis*- and *trans*-decalin, but only decalins dominate in the products with Pt/Al_2O_3 and Pd/TiO_2. Pt/Al_2O_3 displayed slightly higher selectivity to *cis*-decalin, whereas both Pd catalysts showed higher selectivity to *trans*-decalin. Highest yield of *trans*-decalin was obtained with Pd/TiO_2. These trends are consistent with the results from a collateral study in this laboratory [4]. Whether or not the kinetic characteristics of the catalyst itself would also result in this different selectivity to decalins cannot be judged simply from the data shown in Table 7.

The results of naphthalene hydrogenation in the presence of benzothiophene are also included in Table 7. When 9 mg benzothiphene was added (1800 ppm of benzothiphene in the feed), the molar ratios of sulfur to Pt and Pd are 3.3 and 1.8, respectively, and this ratio increases to 7.8 for Pt and 4.3 for Pd catalysts with addition of 21 mg benzothiphene (4200 ppm in the feed). The addition of 1800 ppm benzothiophene caused a 87, 53, and 39% decrease of the naphthalene conversion respectively for the Pt/Al_2O_3, Pd/Al_2O_3, and Pd/TiO_2 catalysts in the two-hour runs; whereas a 90, 84, and 57% decrease was observed respectively when 4200 ppm benzothiophene was added It is clear that benzothiophene can significantly hinder the hydrogenation activities of noble metal catalysts and a higher sulfur content resulted in a lower conversion during the same period of reaction. However, the above percentage reductions in naphthalene conversion indicate that palladium catalysts are less sensitive to benzothiophene than the platinum catalyst, and that the TiO_2 support is superior over Al_2O_3 support with respect to the catalytic hydrogenation activity in the presence of benzothiophene. This is generally true when compared either at similar sulfur/catalyst wt ratios or at comparable sulfur/metal molar ratios. For example, the naphthalene conversions over Pd/TiO_2 and Pd/Al_2O_3 catalysts in the presence of a larger amount of sulfur (4200 ppm; S/Pd mol ratio: 4.3) are still higher than that over Pt/Al_2O_3 catalyst with a smaller amount of sulfur (1800 ppm; S/Pt mol ratio: 3.3), and Pd/TiO_2 catalyst is superior to Pd/Al_2O_3 in terms of higher conversion, as can be seen from Table 7. Since the sulfur/metal molar ratio is larger than 1 in all the runs in the presence of benzothiophene, the sulfur added (particularly at the level of 4200 ppm) is enough to cover all the metal surface even with 100% metal dispersion. Therefore, the above results indicate that Pd/TiO_2 and Pd/Al_2O_3 catalysts have higher sulfur tolerance than Pt/Al_2O_3, and in this context Pd/TiO_2 catalyst is more promising than the other two catalysts.

To see whether the sulfur poisioning of the catalysts is a permanent effect, experiments with an extended reaction period (8 h) were performed. The results in Table 7 show that the naphthalene hydrogenation in the presence of benzothiophene can proceed to a conversion as high as 89 and 78% respectively for Pd/TiO_2 and Pd/Al_2O_3. Extending the reaction time with the Pd catalysts from 2 to 8 h resulted in gradual recovery of naphthalene conversion. This indicates that hydrogenation activity of the Pd catalysts can be recovered as a result of concomitant hydrodesulfurization. However, the sulfur poisoning on Pt/Al_2O_3 catalyst seems to be permanent as no recovery was observed by extending the reaction time. The reason why Pd catalysts showed better sulfur tolerance than the Pt catalyst is not clear at present; not only the type of the metal and support but also the pretreatment condition employed can cause a difference. Arcoya *et al.* [18] proposed that as the electron-donating character of palladium atoms decreases the metal becomes more sulfur-tolerant. Since the Pd/Al_2O_3 catalyst used in this study was pretreated in 20% O_2, positively charged Pd which could exist in this catalyst. However, this would not apply to Pd/TiO_2 catalyst since the hydrogen pretreatment at 473 K was found to be sufficient to reduce Pd to its zero-valence state. On the other hand, Chen *et al.* [9] found that Pt/TiO_2 showed higher resistance to H_2S than Pt/Al_2O_3 and suggested that the labile oxygen in TiO_2 could react with H_2S to form SO_x. This provides an insight to how the support may affect the sulfur-resistance of noble metal catalysts, and this effect may account for why extending the reaction time restored the catalyst activity in the presence of H_2S generated from benzothiophene conversion (see below). However, it is difficult to identify what the so-called labile oxygen is and how it could be generated [9]. TiO_2 supported noble metal catalysts have been known to cause metal-support interaction with the TiO_2 being partially reduced. The factors that could change the sulfur resistance of the Pd/TiO_2 catalyst include the partial reduction of TiO_2, the special active site at the interfacial region, the electronic interaction between metal and support, and even the formation of palladium hydride. Further study on the the origin of sulfur tolerance is needed in future work.

It should be noted that no benzothiophene was identified in the liquid products from all the runs with the addition of benzothiophene. In the runs with Pt/Al_2O_3, it is likely that benzothiophene was adsorbed strongly on the surface. The situation is different with Pd/TiO_2 and Pd/Al_2O_3. That the hydrogenation reaction approached completion with extended reaction time indicates that benzothiophene was gradually converted (on Pd/TiO_2 and Pd/Al_2O_3) to other sulfur species which do not deactivate the catalyst seriously as compared to benzothiophene. It is worthy noting the yield (selectivity times conversion) of ethylbenzene included in the R-(1-ring) category in Table 7, which increased with reaction time in the runs with added benothiophene. The yields of ethylbenzene with Pd/TiO_2 were 55.6, 75.3, and 79.9 mol% based on benzothiophene at 2, 4, and 8 h, respectively. Moreover, the partial hydrogenation product of benzothiophene, dihydrobenzothiophene, was detected in the products. The yields of dihydrobenzothiophene with Pd/TiO_2 were 17.4, 6.2 and 0 mol% based on benzothiophene at 2, 4, and 8 h, respectively. On the basis of these results, it is likely that the conversion of the benzothiophene over the Pd catalysts proceeded via a hydrodesulfurization reaction to form ethylbenzene and hydrogen sulfide with dihydrobenzothiophene as the intermediate. Accordingly, the hydrogen sulfide formed does not deactivate the palladium catalysts as much as benzothiophene does.

Figure 68 shows the selectivities to tetralin and decalins as a function of naphthalene conversion. Though the presence of benzothiophene in the feed decreased naphthalene conversion, it is interesting to note that the selectivity to hydrogenated naphthalene products were not significantly affected. It can be observed from Figure 68 that tetralin is the dominant product except in the region where naphthalene conversion approaches 100%, regardless of the presence of benzothiophene. This trend in product selectivity coincides with that presented in Table 6 for naphthalene hydrogenation at 553 K and that reported for $CoMo/Al_2O_3$ at 623 K [17]. This indicates that the effect of benzothiophene is likely site-blocking rather than electronic interaction, and that naphthalene hydrogenation could occur concurrently with the benzothiophene hydrodesulfurization. These results suggest that some noble metal catalysts can be useful for low-temperature hydrotreating purpose even when the feed contains sulfur.

Quantitative Estimation of Sulfur Resistance

In an effort to obtain a quantitative analysis of the effect of benzothiophene on the naphthalene hydrogenation over these noble metal catalysts, we performed a pseudo-first order kinetic analysis. The apparent rate constants can be estimated by the slopes from a graph like Figure 69, where the results reported for the naphthalene hydrogenation at 553 K (Table 6) and the hydrogenation at 473 K in the presence of 0.5 wt% sulfur (Table 7) are presented accordingly. The effect of benzothiophene on the rate of naphthalene hydrogenation is then estimated by the ratio of the apparent rate constant in the presence of benzothiophene to that without benzothiophene, i.e., ks/k. After correction for the amounts of catalysts used in different runs, the ks(473K)/k(553K) ratio was found to be 0.1, 0.12, and 0.02 for Pd/TiO_2, Pd/Al_2O_3, and Pt/Al_2O_3 respectively. If the activation energy that Nieuwstad *et al.* [7] reported for 2-methylnaphthalene hydrogenation over Pd/C catalyst, 10 kcal/mol, is used to correct for the effect of reaction temperature, then the ks(473K)/k(473K) ratio becomes 0.46, 0.56, and 0.1 respectively for Pd/TiO_2, Pd/Al_2O_3, and Pt/Al_2O_3. This again indicates that the palladium catalysts are less affected by the presence of benzothiophene. Based on the equation reported by Lo [5,19] and the benzothiophene concentration used in this study, a ks/k ratio of 0.73 was estimated for $NiMo/Al_2O_3$ at 623 K; the ks/k ratios of the two palladium catalysts at 473 K are practically comparable. This indicates that the palladium catalysts are comparable to $NiMo/Al_2O_3$ for simultaneous hydrogenation and hydrodesulfurization even at a lower reaction temperature when $NiMo/Al_2O_3$ catalyst shows little activity.

TGA Analysis

The results of TGA analysis of the fresh and used Pd/Al_2O_3 catalysts are shown in Figure 70. For the sample that was exposed to the reaction mixture at room temperature for 30 min, two weak weight loss features appear at approximately 443 and 693 K. The former feature cannot be unambiguously explained since it is within the region where moisture desorbs, while the latter is considered as the naphthalene adsorbed on the catalyst since no reaction would occur at this condition. This 693 K weight loss feature can also be observed for other Pd/Al_2O_3 samples whose reaction conversion were less than completion. For the sample tested at 473 K for 2 h, the 693 K feature cannot be identified, likely due to the fact that the conversion level was as high as 100%. For the sample used for the reaction in the presence of benzothiophene, this 693 K feature is only barely above the noise level of the baseline, which implies that the surface coverage of naphthalene was low when the benzothiophene present. This is consistent with the discussion above that benzothiophene may be preferably adsorbed. The new feature appearing at around 473 K with the sample tested with benzothiophene could be due to the adsorbed benzothiophene, but it needs further experiments to verify.

Comparison between Pd/TiO_2 and Pt/Al_2O_3 samples tested with or without benzothiophene is given in Figure 71. For the two used Pt/Al_2O_3 samples, only in the region below 473 K can TGA features be observed which make unambiguous attribution impossible owing to the possible interference from the moisture. Pd/TiO_2 was found to contain very little moisture feature and a small weight gain feature around 493 K which shifts to higher temperature when benzothiophene is present in the feed. An oxidation of either the reduced Pd or the partially reduced TiO_2 could cause this feature. The oxidation of reduced Pd is considered less likely because it was not observed in Pd/Al_2O_3 samples and because all the samples used in TGA analysis had been air-exposed. Although no report on the partial reduction of TiO_2 after a 473 K H_2 pretreatment was found in the literature, oxygen adsorption isobar of TiO_2 indicated that oxygen adsorption at around 473 K is possible for activated TiO_2 [20]. Therefore, the weight gain feature of Pd/TiO_2 might be due to the interaction between O_2 and activated TiO_2, e.g., partially reduced TiO_2 either due to the pretreatment or due to the reducing environment of the reaction. If this speculation is true, its shift to higher temperature when tested in the presence of benzothiophene indicates that benzothiophene might interact with the partially reduced TiO_2. Finally, TGA results showed that there is no coking problem with these noble metal catalysts under the reaction conditions used. This is another potential advantage of low-temperature catalytic hydrogenation with the noble metal catalysts.

Thermodynamic and Kinetic Considerations

The equilibrium of the naphthalene hydrogenation and its reverse reaction has been studied by Frye [21] and by Frye and Weitkamp [22]. The equilibrium constants were found to be well below 0.1 for naphthalene hydrogenation to either tetralin or decalins at a temperature of 573 K or above. This indicates that this reaction is thermodynamically unfavorable at higher reaction temperatures. Similarly, the hydrogenation of phenanthrene and other polycyclic aromatic compounds is also thermodynamically unfavorable at higher temperature [5,21]. However, the industrial hydrotreating process for improving hydrogen/carbon ratio of heavy liquids typically uses a temperature above 623 K and a high hydrogen pressure with catalysts such as NiMo/Al_2O_3. The heavy liquids, especially those from coal liquefaction, contains a significant amount of aromatics and polycyclic aromatic compounds. Thus, a high hydrogen pressure is necessary if high conversion is desired.

Figure 72 shows the trends of equilibrium conversions of naphthalene and the selectivity of its hydrogenated products as a function of reaction temperature. Figure 72 was derived from calculation based on the equilibrium constants reported by Frye and Weitkamp [22], a feed with the hydrogen/naphthalene ratio of 13, and a total pressure of either 1 or 10 atmosphere; the assumption of ideal gas mixture was imposed for simplification. It is clear that the equilibrium conversion decreases with increasing temperature and that tetralin becomes the dominant product at higher temperatures where the naphthalene conversion drops below ca. 80%. A high reaction pressure obviously shifts these trends to higher temperature range. Figure 72 also shows that the reaction at lower temperature and a lower pressure could have the same thermodynamic equilibrium as the reaction at higher temperature and higher pressure. Thus, a lower temperature hydrotreating process is thermodynamically feasible beside its higher energy efficiency.

In addition to the thermodynamics, the kinetic aspects would also determine whether a lower-temperature hydrotreating process is technically feasible. The conventional hydrotreating catalysts operating at the temperature above 623 K usually have the advantage of being inexpensive and capable of simultaneous hydrodesulfurization, hydrodenitrogenation, and hydrodeoxygenation. However, these catalysts are relatively inactive at a temperature below 573 K; therefore, other types of catalysts should be examined when a lower-temperature hydrotreating process is desired. Supported Group VIII catalysts have been used for hydrogenation reactions over a wide temperature range, and have shown significant activities for the hydrogenation of aromatic compounds at temperatures below 473 K [1,6,7]; therefore, they could be the candidates for low-temperature hydrotreating catalysts. Although the noble metal catalysts were found easily poisoned by sulfur [8], recent studies showed that sulfur resistance of Pt and Pd catalysts is affected by factors such as the valence state of metal [18,23], the type of support [9,11,23,24], the preparation procedure [10], and the extent of presulfurization [25]. This implies that tailoring the supported noble metal catalysts may improve the sulfur resistance and make useful catalysts for low-temperature hydrotreating purpose.

From Tables 6 and 7, the three noble metal catalysts studied showed their potentials for applications in the polycyclic aromatic hydrogenation and hydrotreating purposes. The high activities of group VIII metal catalysts (Pt, Pd, Ni) toward hydrogenation of alkylbenzenes and of polycyclic aromatic compounds have been known for some time; their activities toward hydrogenation of polycyclic aromatic compounds can be orders of magnitude higher than the conventional hydrotreating catalysts such as $NiMo/Al_2O_3$ [1]. Even the presulfided Pt and Pd catalysts showed significantly higher hydrogenation activities and C-N hydrogenolysis activities than sulfided Mo catalyst [26]; this indicates that sulfur-poisoned noble metal catalysts might still have comparable activities to the conventional hydrotreating catalysts. Thus, in terms of higher energy efficiency and higher activity of the catalyst, the use of some noble metal catalysts for low-temperature hydrotreating purposes could become an attractive option in the future. However, more detailed studies are needed before effective implementation of supported noble metal catalysts for these applications.

Summary

The present study, though still preliminary, has shown that noble metal catalysts such as Pt and Pd supported on Al_2O_3 and TiO_2 can be used for low-temperature hydrogenation of polyaromatic hydrocarbons, and they display catalytic activity even in the presence of sulfur in the feed ranging from 1800 to 4200 ppm. The Pd catalyst shows high sulfur resistance than Pt when supported on Al_2O_3, and the sulfur tolerance is even higher when Pd is loaded onto TiO_2 support. The potential of Pd/TiO_2 as a sulfur-tolerant catalyst for low-temperature hydrotreating warrants further detailed study.

Appendix: Gas Yield and Hydrogen Consumption Calculations

The estimations of hydrogen consumption and total gas yields are important in understanding the extent of hydrogenation reaction and the effect of hydrotreating, as well as in evaluating the catalyst performance. A simple approach is described below which is based only on the weight changes of the tubing bomb during its loading and unloading and the average molecular weight of gas products (excluding hydrogen) identified from gas chromatography. This approach uses two assumptions: (i) the ideal gas law is valid at room temperature and the pressure of reaction loading, and (ii) the gas solubility in the solvent inside the bombs at room temperature and the loading pressure can be neglected. These may seem oversimplified but in considering the experimental uncertainties it provides reasonable estimations of the hydrogen consumption and the gas yield. That the calculated $\Delta H/\Delta N$ ratios in Tables 6 and 7 show agreement with the product distribution obtained from the chromatography validates this approach.

Procedures

1. Calculate the amount of hydrogen loaded in the tubing bomb before initiating the reaction:

$$(n_{H_2})_{feed} = \frac{[(\Delta wt)_{H_2} + (wt)_{air}]}{(MW)_{H_2}}$$

or alternatively, $$(n_{H_2})_{feed} = \frac{P_{feed}(V_{Rx} - V_{lf})}{RT_r}$$

2. Calculate the average molecular weight of the vent gas after the reaction is quenched to room temperature:

$$(\Delta wt)_{vent} = \frac{P_{Rxn}(V_{Rx} - V_{lp})(MW)_{vent}}{R\,T_r} - \frac{P_{atm}(V_{Rx} - V_{lp})(MW)_{vent}}{R\,T_r}$$

$$\therefore\ (MW)_{vent} = \frac{(\Delta wt)_{vent}\,R\,T_r}{(V_{Rx} - V_{lp})\,(P_{Rxn} - P_{atm})}$$

3. Calculate the average molecular weight of the vent gas based on the gas chromatography analysis on the collected gas sample, in which hydrogen is excluded:

$$(MW)_g = \frac{\text{Total Weight}}{\text{Total Number of Moles}} = \frac{\sum(\text{Peak Area / Response Factor of Weight})_i}{\sum(\text{Peak Area / Response Factor of Mole})_i}$$

4. Calculate the mole fraction of hydrogen in the vent gas:

$$(MW)_{vent} = (MW)_g(1 - y_{H_2}) + (MW)_{H_2}\,y_{H_2}$$

$$\therefore\ y_{H_2} = \frac{(MW)_g - (MW)_{vent}}{(MW)_g - (MW)_{H_2}}$$

5. Calculate the hydrogen consumption in molar basis:

$$(n_{H_2})_{vent} = \frac{P_{Rxn}(V_{Rx} - V_{lp})\,y_{H_2}}{R\,T_r}$$

$$\therefore\ H_2 \text{ Consumption} = (n_{H_2})_{feed} - (n_{H_2})_{vent}$$

6. Calculate the gas yield in weight basis:

$$\text{Gas Yield} = \frac{P_{Rxn}(V_{Rx} - V_{lp})(1 - y_{H_2})(MW)_g}{RT_r}$$

Nomenclature

$(MW)_{air}$	average molecular weight of air;
$(MW)_g$	average molecular weight of the gas products (excluding hydrogen);
$(MW)_{H2}$	molecular weight of hydrogen;

$(MW)_{vent}$	average molecular weight of the vent gas after reaction;
$(n_{H2})_{feed}$	number of moles of hydrogen loaded initially;
$(n_{H2})_{vent}$	number of moles of hydrogen in the vent gas;
P_{atm}	atmospheric pressure;
P_{Rxn}	pressure of the tubing bomb after reaction at room temperature, read from the gauge atop the tubing bomb;
R	gas constant;
T_r	room temperature;
V_{lf}	liquid volume in the tubing bomb, estimated by the solid and liquid feed;
V_{lp}	liquid volume in the tubing bomb after the reaction, estimated by the solid and liquid unloaded;
V_{Rx}	total inner volume of the tubing bomb;
$(wt)_{air}$	weight of air inside the tubing bomb before loading hydrogen;
$(\Delta wt)_{H2}$	weight difference before and after loading hydrogen prior to reaction, measured by a lab. balance;
$(\Delta wt)_{vent}$	weight difference before and after venting the tubing bomb after reaction, measured by a lab. balance;
y_{H2}	mole fraction of hydrogen in the vent gas.

References

1. A. Stanislaus and B.H. Cooper, Catal. Rev.- Sci. Eng., 36 (1994) 75.

2. C. Song, W.-C. Lai and H.H. Schobert, Ind. Eng. Chem. Res., 33 (1994) 548.

3. C. Song, S. Eser, H.H. Schobert and P.G. Hatcher, Energy & Fuels, 7 (1993) 234.

4. A. Schmitz, G. Bowers and C. Song, Am. Chem. Soc. Div. Fuel Chem. Prepr., 40 (1995) 930.

5. M.J. Girgis and B.C. Gates, Ind. Eng. Chem. Res., 30 (1991) 2021.

6. K. Sakanishi, M. Ohira, I. Mochida, H. Okazaki and M. Soeda, Bull. Chem. Soc. Jpn., 62 (1989) 3994.

.7 Th.J. Nieuwstad, P. Klapwijk and H. van Bekkum, J. Catal., 29 (1973) 404.

8. C.H. Bartholomew, P.K. Agrawal and J.R. Katzer, Advan. Catal., 31 (1982) 135.

9. Y. Chen, Y. Chen, W. Li and S. Sheng, Appl. Catal., 63 (1990) 107.

10. L.E. Hayes, C.E. Snape and S. Affrossman, Prepr. Am Chem. Soc. Div. Fuel. Chem., 36 (1991) 1817.

11. M.N. Berube, B. Sung and M.A. Vannice, Appl. Catal., 31 (1987) 133.

12.. M. Koussath and, D. Vamvouka, H. Economou and X. Verykios, Appl. Catal., 77 (1991) 283.

13. M. Koussathana, N. Vamvouka, M. Tsapatsis and X. Verykios, Appl. Catal. A, 80 (1992) 99.

14. C. Song, T. Nihonmatsu and M. Nomura, Ind. Eng. Chem. Res., 30 (1991) 1726.

15. C. Song, H.H. Schobert and H. Matsui, Am. Chem. Soc. Div. Fuel Chem. Prepr., 36 (1991) 1892.

16. S.D. Lin, unpublished results.

17. S.C.Korre, M.T. Klein and R.J. Quann, Ind. Eng. Chem. Res., 34 (1995) 101.

18. A. Arcoya, X.L. Seoane, N.S. Fgoli and P.C. L'Argentiere, Appl. Catal., 62 (1990) 35.

19. H.S. Lo, Ph. D. Dissertation, University of Delaware, Newark, Newark, 1981.

20. S.D. Lin, Ph. D. Dissertation, The Pennsylvania State University, 1990.

21. C.G. Frye, J. Chem. Eng. Data, 7 (1962) 592.

22. C.G. Frye and A.W. Weitkamp, J. Chem. Eng. Data, 14 (1969) 372.

23. X.L. Seoane, P.C. L'Argentiere, N.S. Fgoli and A. Arcoya, Catal. Lett., 16 (1992) 137.

24. T. Xiao, L. An, W. Ahang, S. Sheng and G. Xiong, Catal. Lett., 12 (1992) 287.

25. A. Vzquez, F. Pedraza and S. Fuentes, J. Mol. Catal., 75 (1992) 63.

26. J. Shabtai, Q. Guohe, K. Balusami, N.K. Nag and F.E. Massoth, F. E., J. Catal., 113 (1988) 206.

5. Exploratory Studies on Coal liquids Upgrading using Mesoporous Molecular Sieve Catalysts

(Contributed by Madhusudan Reddy Kondam and Chunshan Song)

Introduction

Detailed synthesis, characterization, and preliminary catalytic activity screening of mesoporous molecular sieves (MCM-41 aluminosilicates) were reported in our earlier reports [1-3]. It was found that source of aluminum used in the synthesis of these materials has a significant influence on their physico-chemical properties [1-5]. The acid strength of these materials was observed to be lower compared to the microporous molecular sieves, comparison of their catalytic activities with microporous molecular sieves is not clearly known. As it is important to examine the mesoporous molecular sieve catalysts for upgrading the coal-derived liquids to jet fuels, we intended to compare their catalytic activities. In this report we report the catalytic activities of mesoporous molecular sieves prepared with four different aluminum sources, microporous molecular sieves (mordenite and Y), and alumina for the model reaction of 1,3,5-triisopropylbenzene (TIPB) hydrocracking.

Experimental

A total of seven catalysts were screened for the reaction of 1,3,5-triisopropylbenzene hydrocracking. Four of them were mesoporous molecular sieves (MCM-41 aluminosilicates) synthesized using aluminum isopropoxide (AI2), Catapal B alumina (PB2), aluminum sulfate (AS2), and sodium aluminate (SA2) with input SiO_2/Al_2O_3 ratio of 25. The detailed synthesis procedure is given elsewhere [1,3,4]. The microporous zeolites (mordenite (CBV-20A), and Y (LZ-Y62)) were obtained from PQ Corporation and Aldrich, respectively. The SiO_2/Al_2O_3 ratios of zeolite Y and mordenite were 5 and 21. Prior to the catalytic runs, all the catalysts were converted to protonic forms by calcining the ammonium forms at 460° C for 4 hours in an air flow of 200 ml/min. The alumina support (S-2) was the same γ-alumina as that used in a previous study [6].

The hydrocracking of 1,3,5-triisopropylbenzene (TIPB) was carried out in a batch reactor according to the procedure reported earlier [5]. All the reactions were carried out in horizontal tubing bomb reactors (with vertical shaking, 200 cycles per minute) with 0.1 g of catalyst, 1.0 g of reactant at 300°C for 30 minutes under 1000 psi hydrogen pressure. The gas products were collected in leak-proof evacuated gas bags and liquid products were recovered with acetone. Both the liquid and gas product analyses were done according to the procedure identical to those reported earlier [2,3,5].

After the catalytic runs, the recovered catalysts were analyzed by thermal analysis (TGA) in order to estimate the coke formation. The conditions were similar with the earlier work starting from 30° C to 700° C at rate of 10° C/min. in an air flow of 200 ml/min.

Results and Discussion

Table 8 and Figure 73 represent the results of the reaction of 1,3,5-triisopropylbenzene (TIPB) hydrocracking over mesoporous (AI2, PB2, AS2, and SA2), microporous (mordenite and Y) molecular sieves and alumina. Table 8 shows both the major gas and liquid products and their distribution. The major products in the gas over all the catalysts are propane and propylene whereas in the liquid the major products are benzene, cumene, 1,3-diisopropylbenzene (1,3-DIPB), 1,4-diisopropylbenzene (1,4-DIPB), unreacted TIPB, and some unidentified di- and tri-alkyl benzenes. The conversion of TIPB over alumina (S-2) is very small (5.4%) compared to those with all other catalysts. Among all the mesoporous molecular sieve catalysts, the catalyst prepared using sodium aluminate (SA2) showed high conversion (47.7%) whereas the one prepared using Catapal B alumina (PB2) showed low conversion (8.9%). Remaining two mesoporous molecular sieve catalysts (AI2 and AS2) prepared with aluminum isopropoxide and aluminum sulfate respectively showed slightly lower conversion (44.4 and 40.5%) compared to the catalyst SA2 (47.7%). The microporous (mordenite and Y) molecular sieve catalysts are also active for this reaction; however, the conversion over zeolite Y is higher (47.5%) compared to that over mordenite (28.9%).

In molecular sieve catalysis, the hydrocracking activity usually depends on the acidity of the catalyst. In fact, hydrocracking of a model compound over molecular sieve catalysts is one of the ways to characterize their acidity. Among all the catalysts tested in this study only the the alumina catalyst is amorphous and less acidic hence it gave very poor conversion compared to all other catalysts tested. Though mesoporous molecular sieve catalysts are found to be active for this reaction, the catalyst prepared with Catapal B alumina showed poor activity. The order of catalytic activity among mesoporous molecular sieves is SA2>AI2>AS2>PB2, which is a good correlation with their acidity order observed from TPD of *n*-butylamine and reported in our earlier reports [2-5]. This acidity difference hence the difference in catalytic activity can be attributed to the difference in the level of aluminum incorporation when different aluminum sources were used in the synthesis. Characterization by X-ray diffraction and solid state ^{27}Al NMR clearly showed that aluminum incorporation is in the same order of observed acidity, hence the catalytic activity [2-5].

In the reaction of TIPB hydrocracking both microporous molecular sieve catalysts (mordenite and Y) have shown good activity, but the zeolite Y is more active compared to mordenite, which also again follows the trend of their acidity. However, the hydrocracking of TIPB over microporous molecular sieves must be mainly on the surface acid sites of the catalyst at least until the dealkylation of one or two isopropyl groups takes place because the TIPB can not diffuse as such into the pores of microporous molecular sieves. The high conversion over zeolite Y might be due to presence of more number of external acid sites because of its low Si/Al ratio compared to mordenite, secondly the diffusion of secondary products like diisopropylbenzene and cumene might also be possible into the pores of zeolite Y leading to high conversion.

The hydrocracking of TIPB depends not only on the acidity of the catalyst but also on the porosity of the catalyst. The overall order of catalytic activity (SA2>HY> AI2>AS2> HM>PB2>alumina) is not the order of acidity for the catalysts tested. From an acidity point of view, both HY and HM should have been much more active compared to all other catalysts but it is not true because TIPB and their cracked products diffuse easily in mesoporous molecular sieves. That is why the mesoporous molecular sieve catalysts with better aluminum incorporation and crystallinity have shown better performance in this reaction compared to zeolite Y and mordenite.

Another important factor to be considered is the catalyst stability. In order to understand the catalyst stability in this reaction of TIPB hydrocracking, the coke formation over catalysts was studied by thermal analysis. Figures 74 and 75 represent the TGA and DTG for the three catalysts (AI2, HM and HY) recovered after the reaction. Figure 74 shows that the weight loss is very high for mesoporous molecular sieve catalyst (AI2) compared to two microporous molecular sieve (HY and HM) catalysts. However, the major weight loss for AI2 is below 230° C whereas for HY and HM major weight loss is after 230° C. Usually if there is a coke formation in the zeolite catalyst, during thermal analysis it starts burning around 400° C, leading to a major weight loss. DTG (Figure 75) clearly shows a major peak for HM and HY after 400° C, which indicates there is a major weight loss due to the coke burning. It also shows that for the mesoporous catalyst AI2 the major weight loss is below 230 °C with two distinct peaks. The peak at lower temperature corresponds to the evolution of regular solvents used in the recovery, in this case acetone, and moisture. Hence the particular low-temperature peak is also present for other catalysts HM and HY. But, the peak at around 190° C for AI2 might be due the some heavy hydrocarbons trapped inside the mesopores which diffused out upon heating. These results indicate that there is almost no coke formation with mesoporous catalysts; however, it is observed with microporous molecular sieves. In fact the color of recovered HY and HM catalysts is black and AS2 is brown, which confirms further that mesoporous catalysts are stable in this reaction compared to microporous molecular sieve catalysts. This can be explained by the low acidity and high diffusivity within the mesopores. These two factors in mesoporous molecular sieves catalysts might not be favoring the formation of coke precursors.

In conclusion, our results in this section indicate that mesoporous molecular sieves are active for the hydrocracking of bulky hydrocarbons; however, acidity is a key factor which depends on aluminum incorporation. Mesoporous molecular sieves catalysts also seem to be more stable for the conversion of bulky hydrocarbons as compared to microporous molecular sieve catalysts, in terms of less coke formation.

References

1. H. H. Schobert, S. Eser, C. Song, P. G. Hatcher, A. Boehman and M. M. Coleman, *Advanced thermally stable jet fuels*, 92PC92104-TPR-10, p. 90.
2. H. H. Schobert, S. Eser, C. Song, P. G. Hatcher, A. Boehman and M. M. Coleman, *Advanced thermally stable jet fuels*, 92PC92104-TPR-11, p. 49.
3. H. H. Schobert, S. Eser, C. Song, P. G. Hatcher, A. Boehman and M. M. Coleman, *Advanced thermally stable jet fuels*, 92PC92104-TPR-12, p. 42.
4. K. M. Reddy and C. Song, *Catalysis Letters*, accepted for publication, 1995.
5. K. M. Reddy and C. Song, *Am. Chem. Soc. Div. Fuel Prpr., 40 (4) (1995) 1003.*
6. C. Song, T. Nihonmatsu, and M. Nomura, *Ind. Eng. Chem. Res., 30 (1991) 1726.*

APPENDIX I

Tables

Table 1. Reduced Pressure of n-C_{14}-N_2 Mixtures at 450 °C as a Function of Initial n-C_{14} Volume and N_2 Pressure in 28-mL Reactor.

	initial N_2 pressure			
	0.17 MPa	0.79 MPa	1.41 MPa	2.03 MPa
n-C_{14}	reduced pressure of mixture (P/P_c)			
1 mL	0.15	0.13	0.16	0.20
5 mL	0.94	0.63	0.58	0.57
9 mL	1.69	1.37	1.26	1.22

Table 2. Surface area and pore volume of original and extracted activated carbon Maxsorb 92-11A before and after thermal stressing with dodecane and decalin.

Maxsorb	N_2 BET surface area, m^2/g	Mesopore area, m^2/g	Micropore area, m^2/g	Total pore volume, cc/g	Average pore diameter, Å
92-11A	2710	175	1760	0.67	10
92-11A, stressed	1820	90	1760	0.37	8
92-11A, coated, stressed	14	1.4	1.8	0.002	6
92-11A extracted	1420	60	1360	0.34	10
92-11A, extracted, stressed	950	45	900	0.21	8

Table 3. Kinetic Parameters of Thermal Degradation of Dodecane.

Reactant	**rate constant x 10^6, sec^{-1}**							
	400°C	**415°C**	**425°C**	**435°C**	**440°C**	**450°C**	**E_a (Kcal/mol)**	**A(sec^{-1})**
Dod Neat	15.1	32.9		118.0		286.0	58	5.4×10^{13}
Dod+10M%BzOH	4.3		30.1		68.0	147.0	67	2.4×10^{16}
Dod+10M%THQ	0.9		7.2		16.0	45.6	71	9.2×10^{16}

Table 4. Metal Concentration in Wyodak Coal.

	Metal Concentration (ppm)				
	Na	K	Ca	Mg	Fe
Wyodak [7]	930	82	12600	2610	2580
Wyodak [8]	800	800	13000	2800	5700

Table 5. Results of Non-Catalytic Liquefaction of Normal and Demineralised Wyodak Coal at 350 °C for 30 min. Under 6.9MPa H_2.

Coal	Pretreatment	Solvent	Gaseous Distribution			Liquid Distribution			Total Liquids	% Conv.
			CO	CO_2	C_1-C_4	Oil	Asph.	Preasph.		
Wyodak	-	-	0.2	4.5	0.2	2.1	2.6	4.5	9.2	12.5
"	demineralised	-	0.087	3.01	0.048	0.06	4.46	10.29	14.81	19.71
"	-	Tetralin	0.2	4.1	0.2	4.1	7.6	10.0	21.7	25.9
"	demineralised	"	0.07	2.0	0.035	2.83	3.38	9.79	16.0	21.52
"	-	1-MN	0.2	4.3	0.2	1.1	5.8	7.4	14.3	18.3
"	demineralised	"	0.095	1.9	0.485	2.14	6.30	11.73	20.16	15.01

Table 6. Naphthalene Hydrogenation over Various Catalysts at 553K Using Tridecane as the Solvent

	$NiMo/Al_2O_3$	Pt/Al_2O_3		Pd/Al_2O_3		Pd/TiO_2		TiO_2	HCl/Al_2O_3
Feed									
Catalyst (mg)	207	127	136	132	137	144	131	132	134
H_2[1] (psig)	1000	1000	1000	1000	1000	1000	1000	1000	1000
Naph[2] (mg)	1001	1001	1003	1002	1011	1002	1004	1001	1005
Reaction[3]									
Time (h)	1	1	2	1	2	1	2	1	1
ΔH_2[4](mmol)	2	10	15	10	16	12	15	3	5
$\Delta H_2/\Delta N$[5]	1.5	1.8	2.2	1.7	2.2	1.8	1.9	4	5.8
Yield[6] (mg)	122	804	949	829	992	863	1016	50	72
% Conv, x_N[7]	17	72	86	77	90	84	98	9	11
Selectivity, wt %[8]									
di-H-N[9]	0.2	0	0	0	0	0	0	0.2	0.3
Tetralin	55	92	85	90	90	92	90	16	6
t-Decalin	0	3	7	2	2	1	6	0	0
c-Decalin	0	2	5	0.7	0.4	0.2	1	0	0
R-(1-ring)[10]	6	0.6	0.6	2	0.5	0.6	0.5	5	3
R-(2-ring)[11]	1	0.1	0.2	0.1	0.1	0.2	0.2	1	0.4
R-(3^+ring)[12]	0	0	0	0	0	0	0	0	2
Solid	0	0.2	0.5	0.3	0.2	0	0	2	2
Gas	38	3	1	5	7	6	3	76	87

---

[1] H_2 feed at room temperature to an accuracy of 20 psig.

[2] Naphthalene.

[3] Temperature setting of the sandbath heater is 200°C.

[4] Number of moles of H_2 reacted.

[5] Molar ratio of H_2 reacted to naphthalene reacted.

[6] Overall yield of products listed below.

[7] Naphthalene conversion, calculated from the amount of N remained and the amount of N fed.

[8] Based on recovered products excluding naphthalene.

[9] Dihydronaphthalene.

[10] R-(1-ring) includes alkylbenzenes and alkylcycloparaffins.

[11] R-(2-ring) includes indenes, indanes, alkyltetralins, alkylnaphthalenes, and biphenyls.

[12] R-(3^+ring) includes species having at least 3-ring structures.

Table 7. Naphthalene Hydrogenation over Noble Metal Catalysts at 473K using Tridecane as the Solvent

	Pt/Al_2O_3					Pd/Al_2O_3					Pd/TiO_2					
Feed																
Catalyst(mg)	124	207	191	184	196	135	208	199	195	202	138	214	197	194	191	202
H_2 (psig)	1500	1500	1500	1500	1500	1500	1500	1500	1500	1500	1500	1500	1500	1500	1500	1500
Naph (mg)	1001	1004	1003	1004	1001	1001	1004	1001	1002	1002	1002	1002	1002	1001	1000	1001
BT[2] (mg)	0	0	9	21	21	0	0	9	21	21	0	0	9	21	21	21
Reaction																
Time (h)	2	2	2	2	8	2	2	2	2	8	2	2	2	2	4	8
ΔH_2(mmol)	4	34	3	2	6	8	29	9	4	10	8	33	7	7	11	17
$\Delta H_2/\Delta N$	4.8	4.3	2.9	2.6	7.7	2.5	3.7	2.4	3.2	1.6	2.8	4.2	1.5	2.1	2.3	2.4
Yield (mg)	115	1072	149	120	133	434	1060	500	187	828	388	1068	636	462	656	949
% Conv, X_N	11	100	13	10	10	42	100	47	16	78	37	100	61	43	61	89
Selectivity, wt%																
di-H-N	0	0	0	0	0	0	0	0	0	0	0	0	0.1	0	0	0
Tetralin	44	1	63	20	47	82	36	83	62	93	84	0.5	88	81	89	89
t-Decalin	0	44	0	0	0	0	43	0.5	0	0.3	0.4	76	0.4	0.3	0.2	0.8
c-Decalin	0	49	0	0	0	0	17	0	0	0	0.1	18	0	0.1	0	0.1
R-(1-ring)	3	0	0.2	7	9	1	0	0.8	4	2	2	0	0.8	2	1.9	1.4
R-(2-ring)	2	0	0.1	3	1	0.5	0.1	0.1	2	0.3	0.4	0.1	0.2	0.4	0.4	3
R-(3^+ring)	0	0	0	0	0	0	0	0	0.4	0	2	0	0.1	0	0	0
di-H-BT[3]	0	0	0	1	0	0	0	0.2	5	0.1	0	0	0	0.8	0.2	0
Solid	6	1	1	11	0	1	0.2	0	0	0.1	0	0	0	0.1	0.1	0.5
Gas	46	6	35	59	43	16	5	15	28	5	12	5	10	15	9	6

[1] See footnotes of Table 1. [2] Benzothiophene. [3] Dihydrobenzothiophene.

Table 8. Hydrocracking of 1,3,5-Triisopropylbenzene over various catalysts (1g reactant, 0.1g catalyst, 300 °C, 30 minutes and 1000 psi H_2)

	Catalyst						
	AI2	PB2	AS2	SA2	Al_2O_3	HM	HY
Conversion (%)	44.42	8.85	40.47	47.68	5.44	28.90	47.53
Product Distribution							
Gas (wt%)							
C1+C2	0.01	0.00	0.01	0.01	0.01	0.02	0.01
Propane	1.26	0.06	1.17	1.61	0.01	1.08	2.06
Propylene	1.96	0.57	2.20	2.99	0.02	0.11	1.80
Isobutane	0.44	0.01	0.26	0.63	0.00	0.39	0.54
n-Butane	0.02	0.00	0.01	0.02	0.00	0.08	0.02
C5+	0.27	0.00	0.00	0.03	0.10	0.14	0.06
Liquid (wt%)							
Benzene	0.03	0.02	0.02	0.03	0.02	0.68	0.04
Cumene	1.19	0.03	0.83	1.14	0.04	3.92	1.93
1,3-DIPB	15.42	2.84	13.80	14.77	0.00	4.00	17.87
1,4-DIPB	4.90	0.38	4.07	4.57	0.00	1.77	6.05
1,3,5-TIPB	55.58	91.15	59.54	52.32	94.56	71.10	52.47
Others	11.24	2.22	9.87	10.21	1.24	6.07	14.16

APPENDIX II

Figures

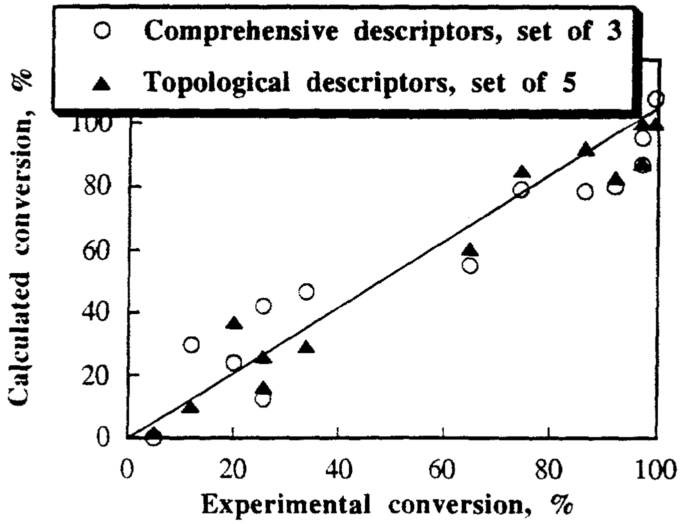

Figure 1. Comparison of the calculated and the experimental conversion after 4-hour high-pressure pyrolysis at 450°C (correlations with 5 topological descriptor set and 3 comprehensive descriptor set), in-house experimental data [2-7].

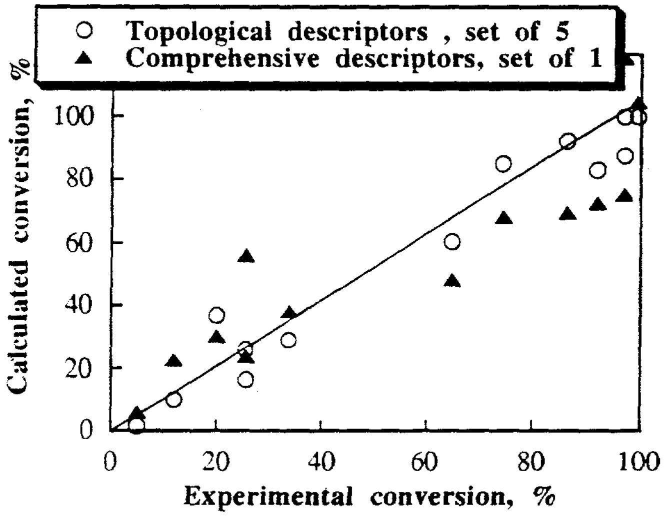

Figure 2. Comparison of the calculated and the experimental conversion (correlations with 5 topological descriptor set and 1 comprehensive descriptor set), the experimental data are the same as in Figure 1.

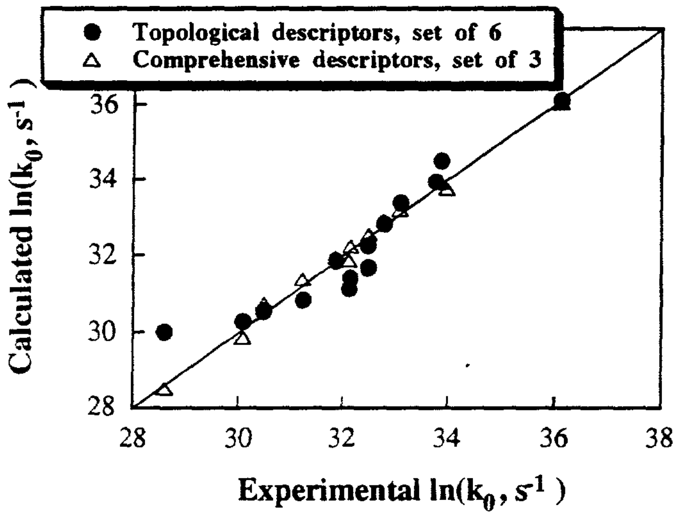

Figure 3. Comparison of the calculated and the experimental ln(k_0); correlations with 5 topological descriptor set and 3 comprehensive descriptor set, literature survey [8].

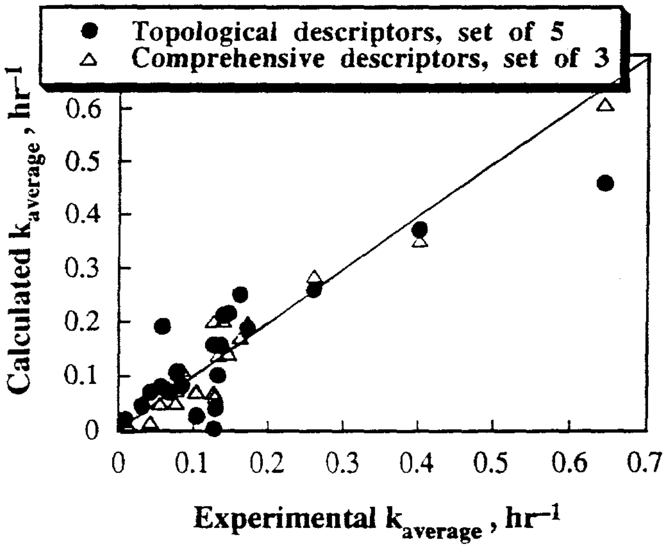

Figure 4. Comparison of the calculated and the experimental average rate of decomposition of saturated cyclic hydrocarbons (correlations with 5 topological descriptor set and 3 comprehensive descriptor set), literature survey [8].

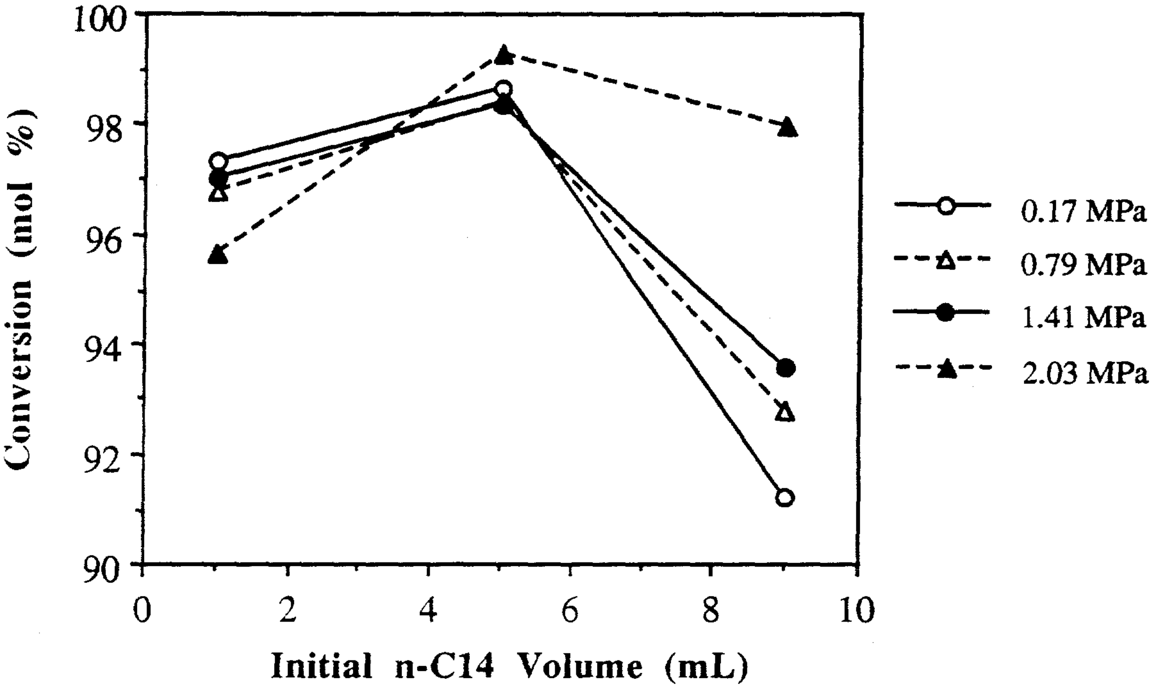

Figure 5. Effects of Initial Sample Volume of *n*-C_{14} (at Room Temperature) on Pyrolytic Conversion at 450 °C for 4 h under Different Initial Pressure of N_2 in 28-mL Microreactors.

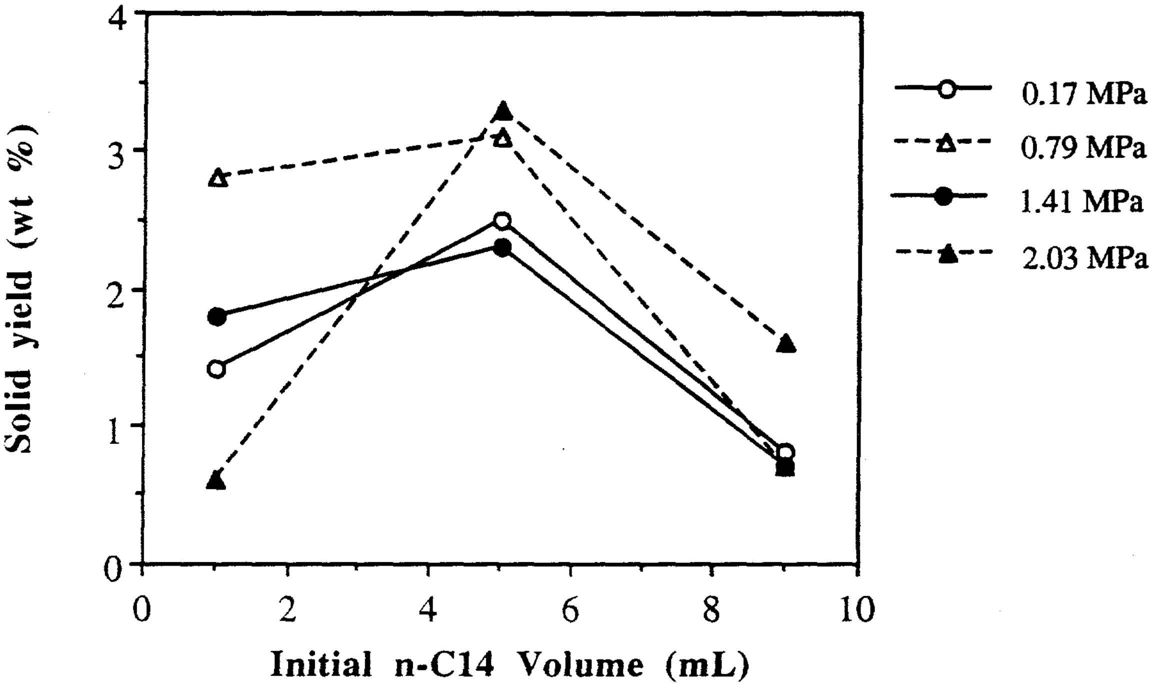

Figure 6. Effects of Initial Sample Volume of *n*-C_{14} (at Room Temperature) on Solid Yield at 450 °C for 4 h under Different Initial Pressure of N_2 in 28-mL Microreactors.

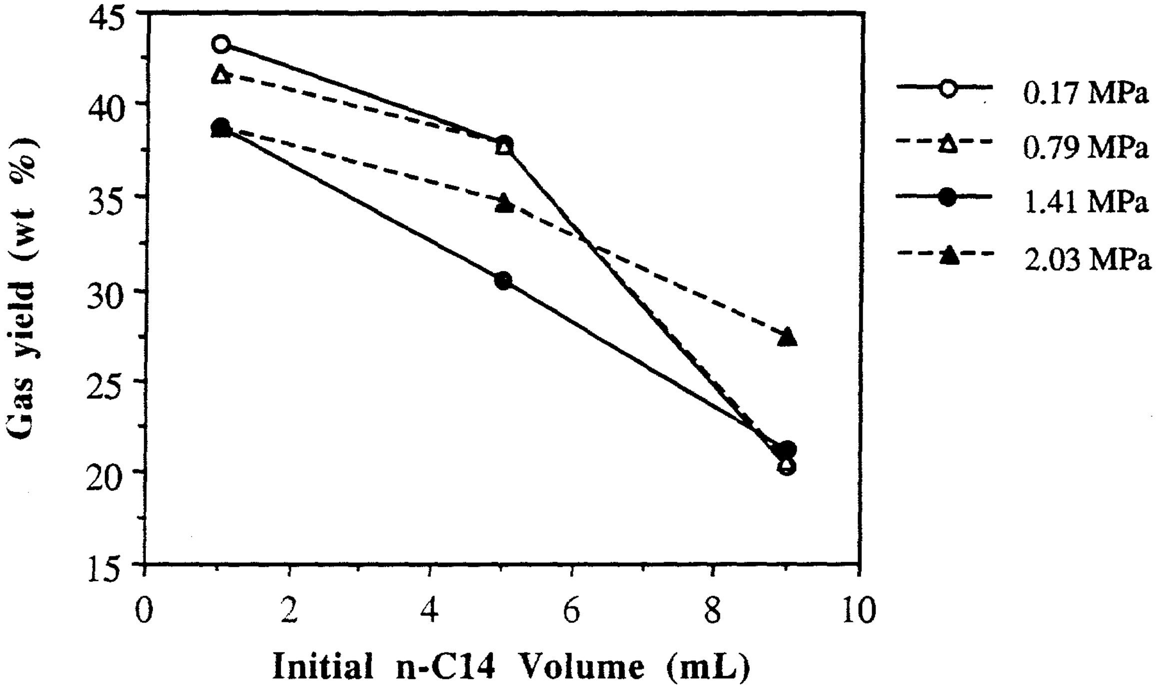

Figure 7. Effects of Initial Sample Volume of *n*-C_{14} (at Room Temperature) on Gas Yield at 450 °C for 4 h under Different Initial Pressure of N_2 in 28-mL Microreactors.

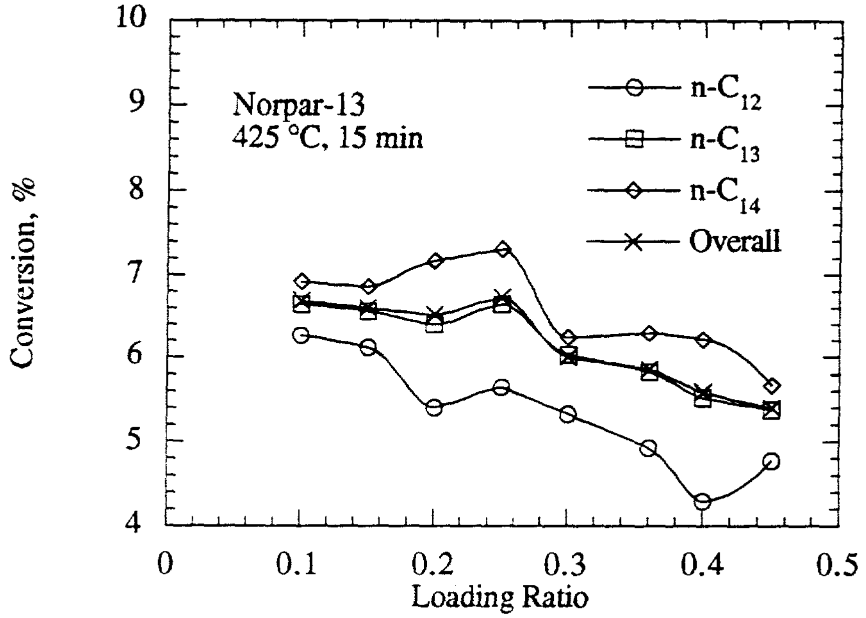

Figure 8. Changes in Conversion with Loading Ratio from Thermal Decomposition of Norpar-13 at 425 °C for 15 min.

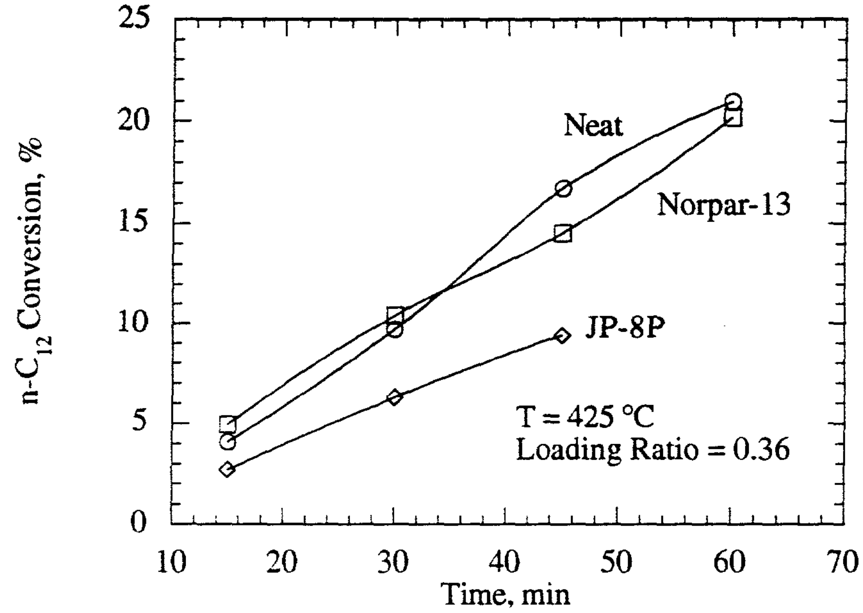

Figure 9. Changes in Conversion of n-C_{12} with Reaction Time from Thermal Decomposition of Pure Compound, Norpar-13, and JP-8P at 425 °C.

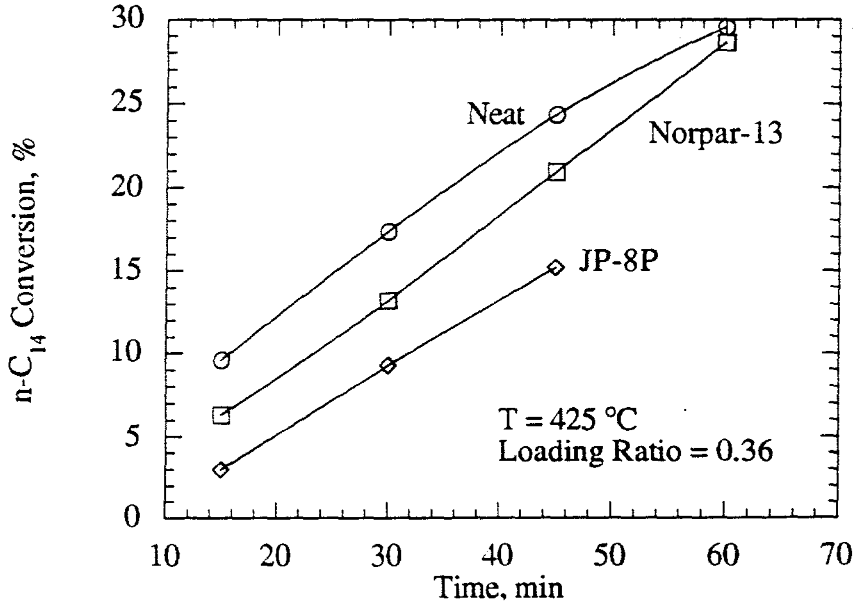

Figure10. Changes in Conversion of n-C_{14} with Reaction Time from Thermal Decomposition of Pure Compound, Norpar-13, and JP-8P at 425 °C.

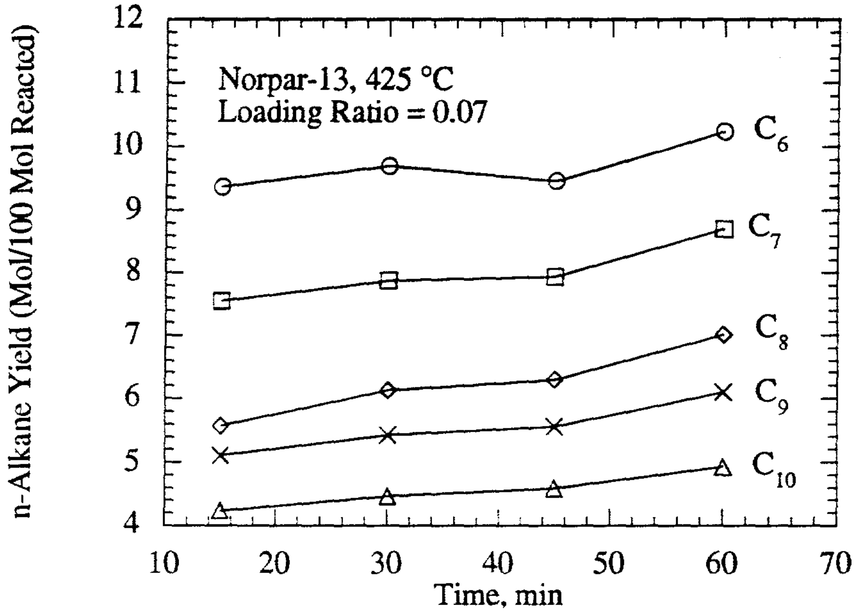

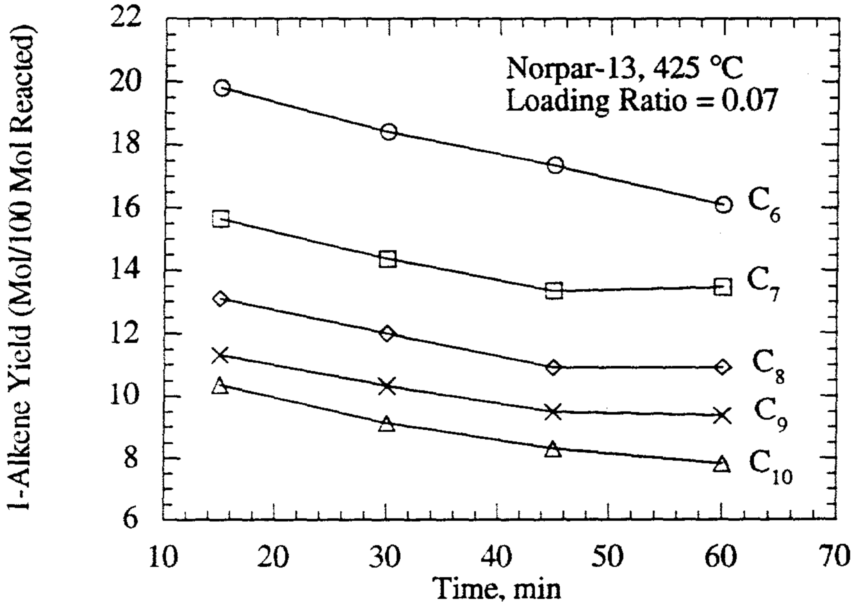

Figure 11. Changes in Molar Yields of C_6-C_{10} *n*-Alkanes and 1-Alkenes with Reaction Time from Thermal Decomposition of Norpar-13 at 425 °C and a Loading Ratio of 0.07.

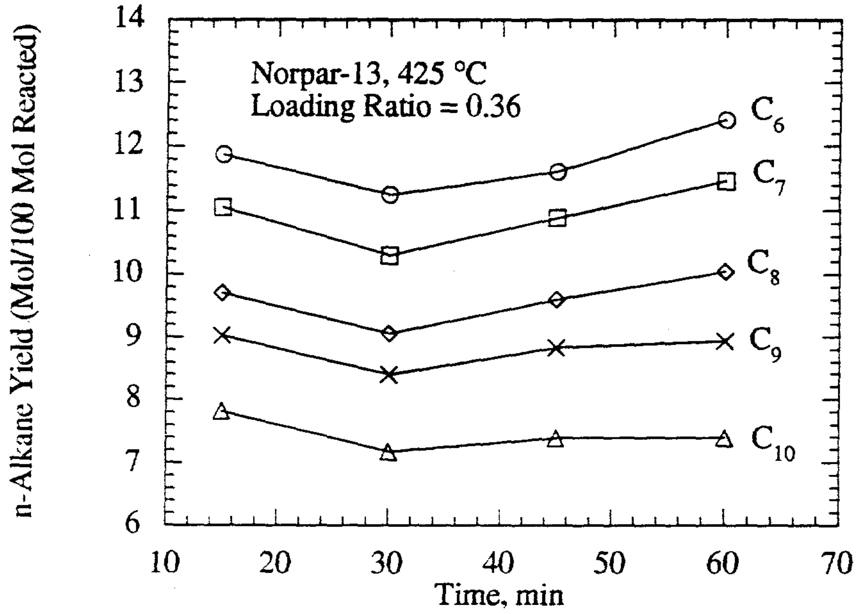

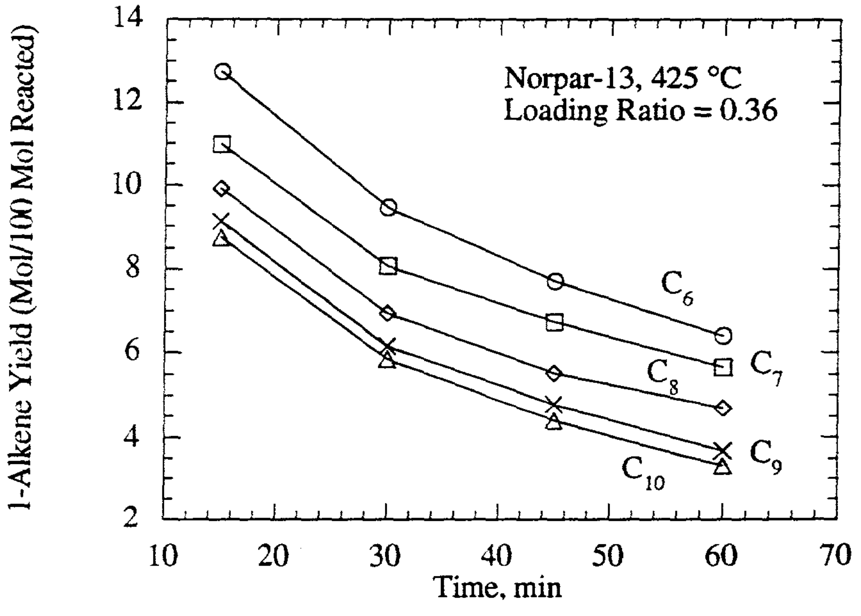

Figure 12. Changes in Molar Yields of C_6-C_{10} *n*-Alkanes and 1-Alkenes with Reaction Time from Thermal Decomposition of Norpar-13 at 425 °C and a Loading Ratio of 0.36.

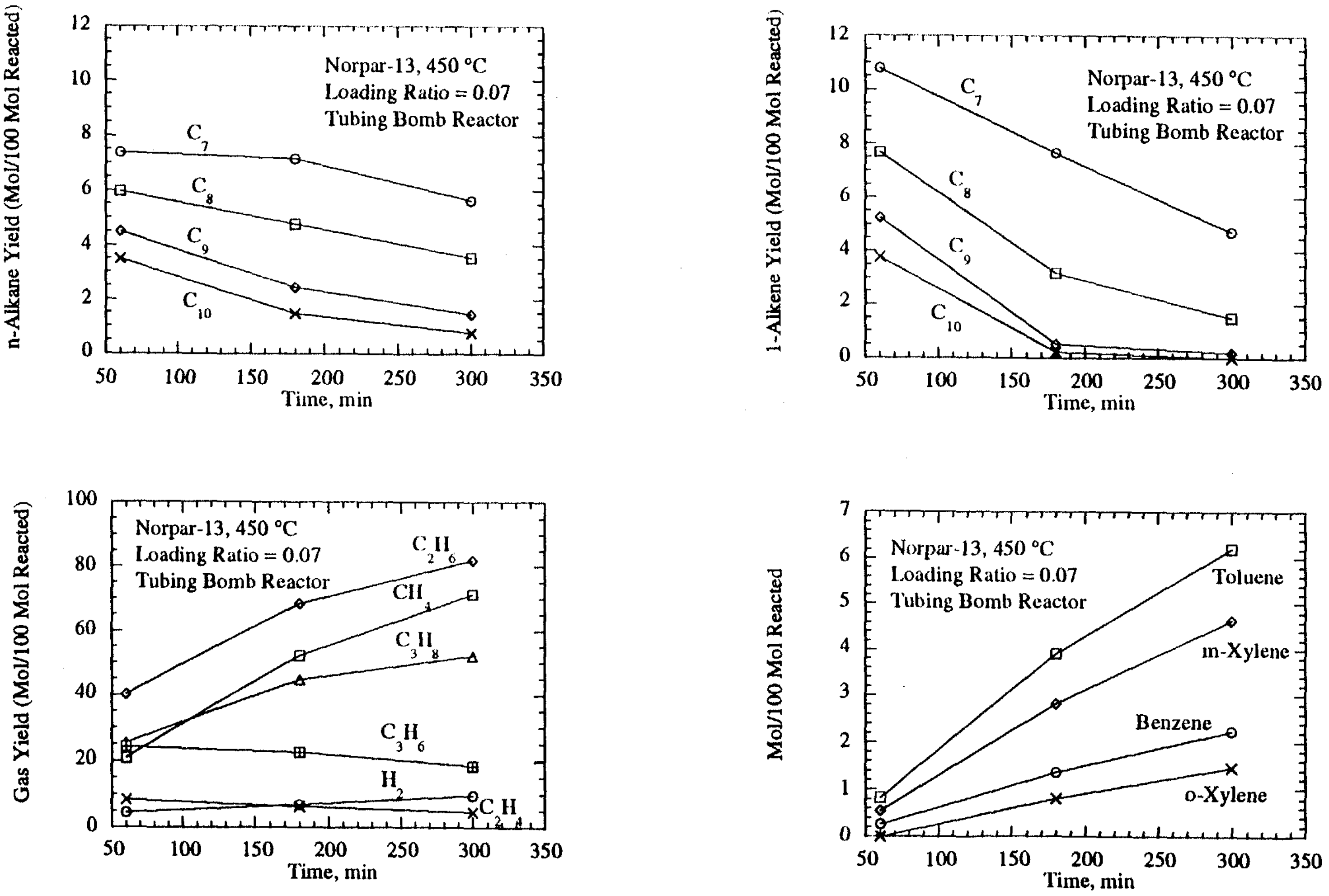

Figure 13. Changes in Product Yields with Reaction Time from Thermal Decomposition of Norpar-13 at 450 °C in Tubing Bomb Reactor for a Loading Ratio of 0.07.

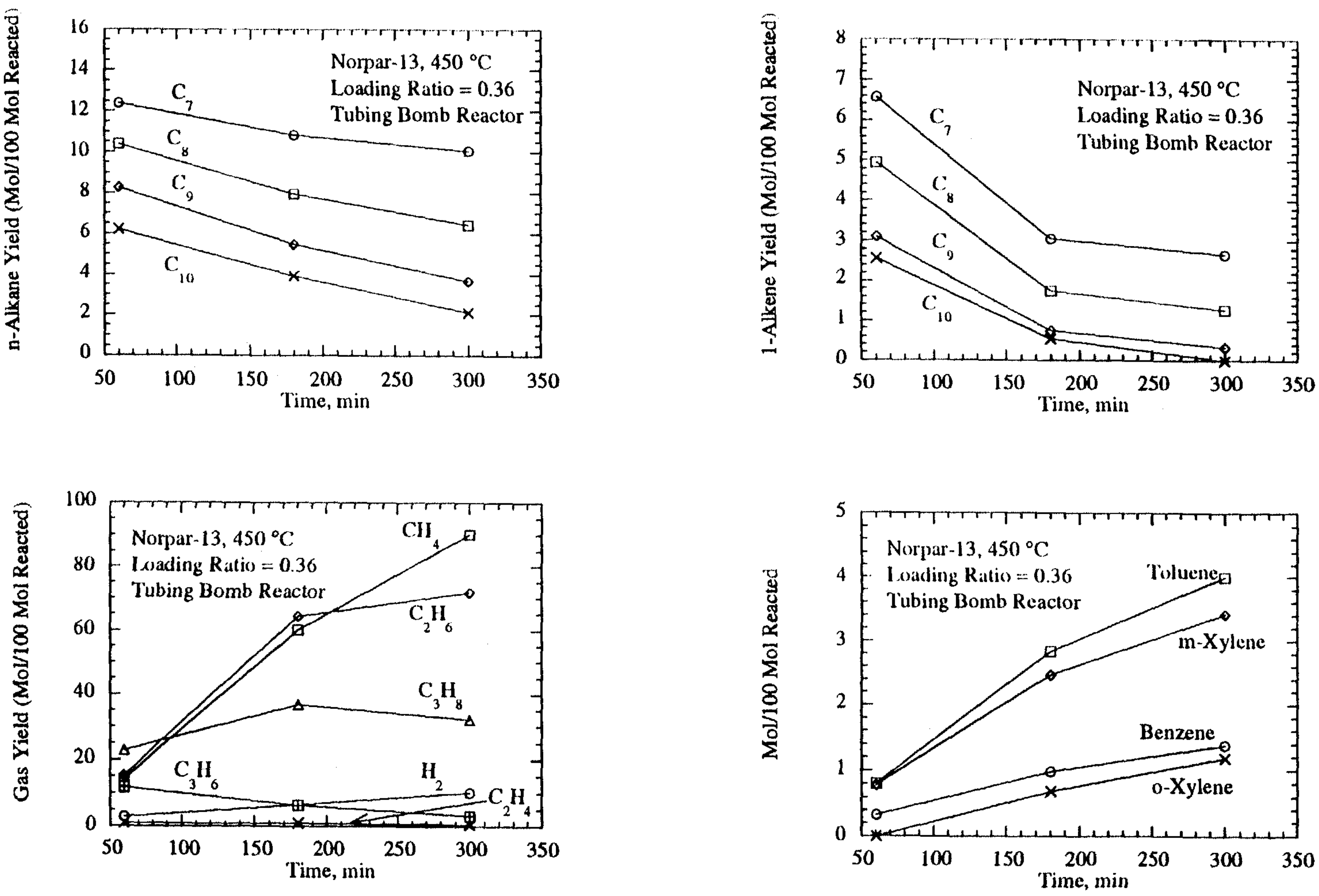

Figure 14. Changes in Product Yields with Reaction Time from Thermal Decomposition of Norpar-13 at 450 °C in Tubing Bomb Reactor for a Loading Ratio of 0.36.

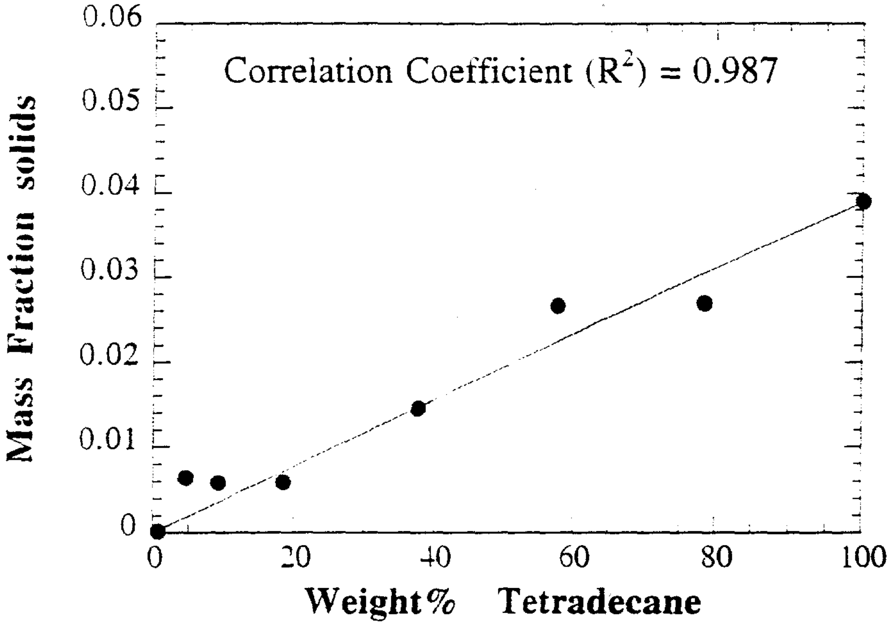

Figure 15. Mass Fractions of deposit produced after 6 hours of heating at 450°C versus initial weight percent of tetradecane present in the fuel mixtures.

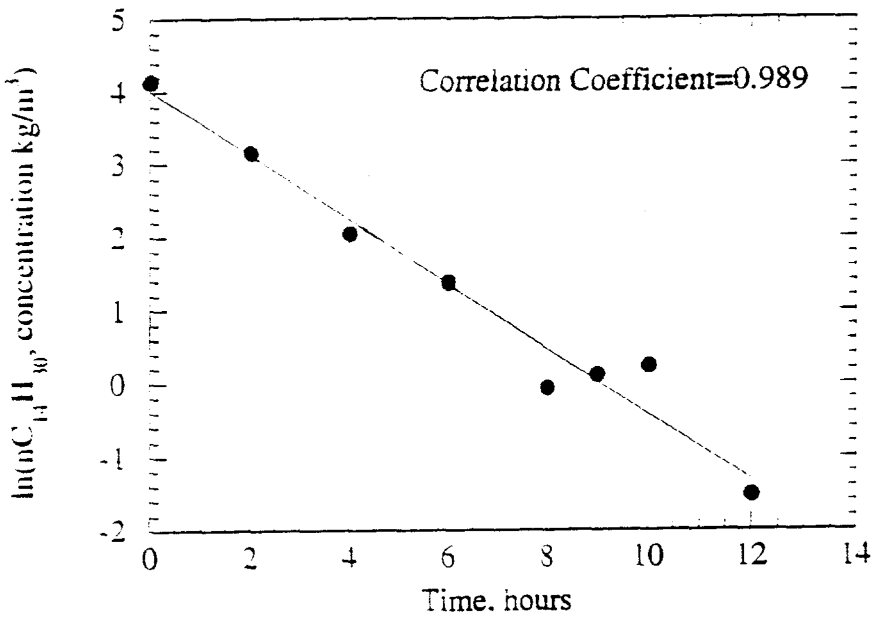

Figure 16. Natural logarithm of concentration of tetradecane remained in the neat and pyrolysed mixture at various times.

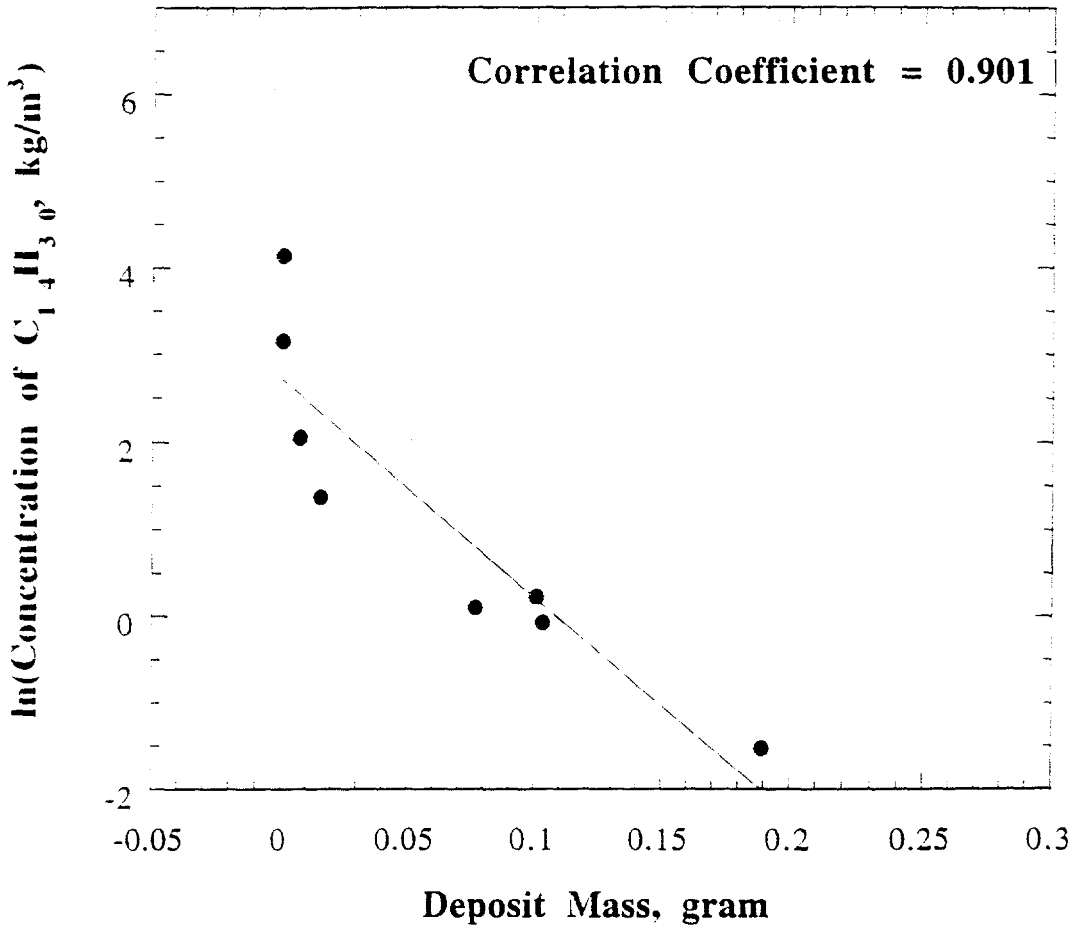

Figure 17. Natural logarithm of concentration of tetradecane remained in the neat and pyrolysed mixture at various times versus deposit mass produced in grams at the same time.

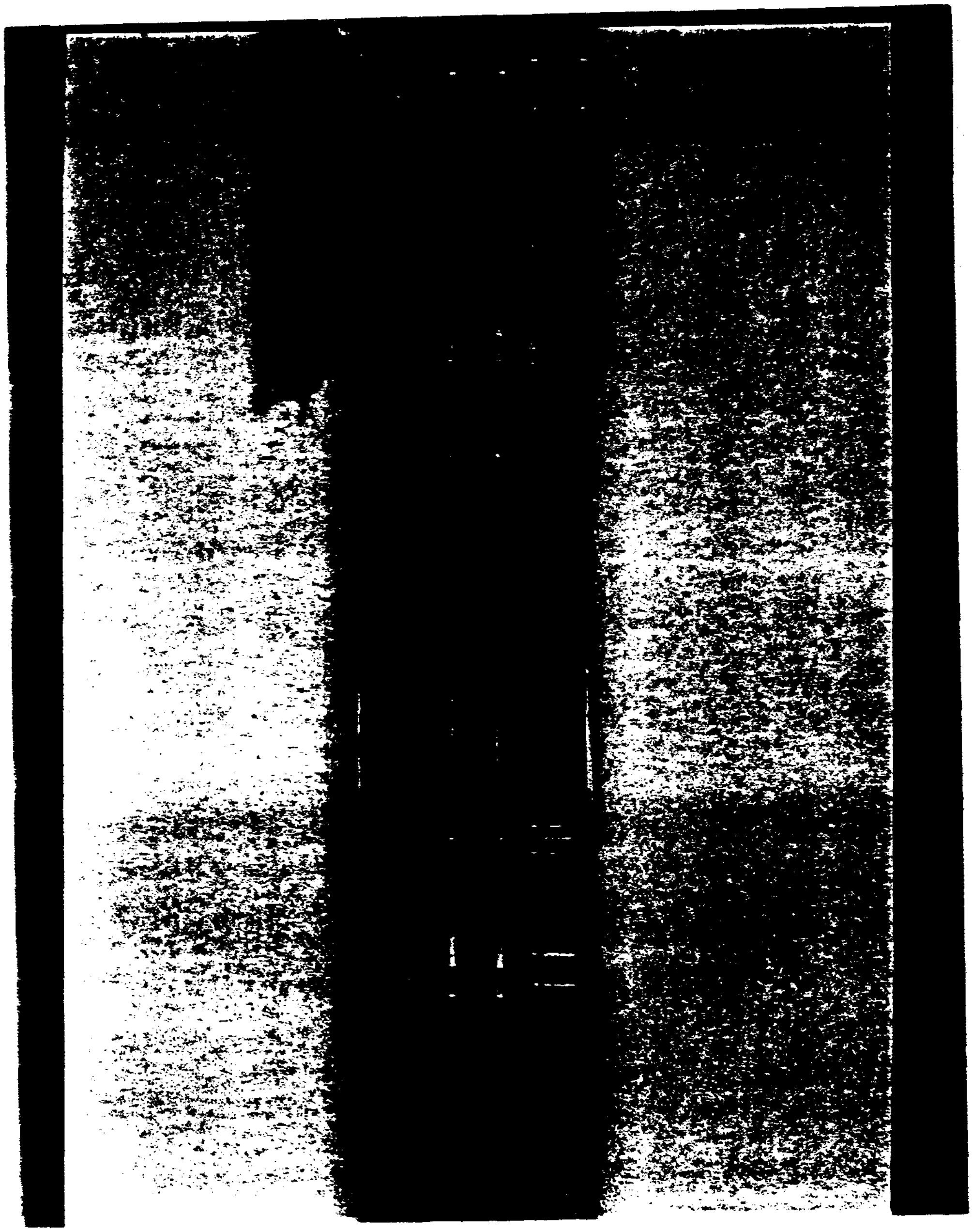

Figure 18. Photograph of Actual Engine Fuel Line Filled with Carbonaceous Deposit.

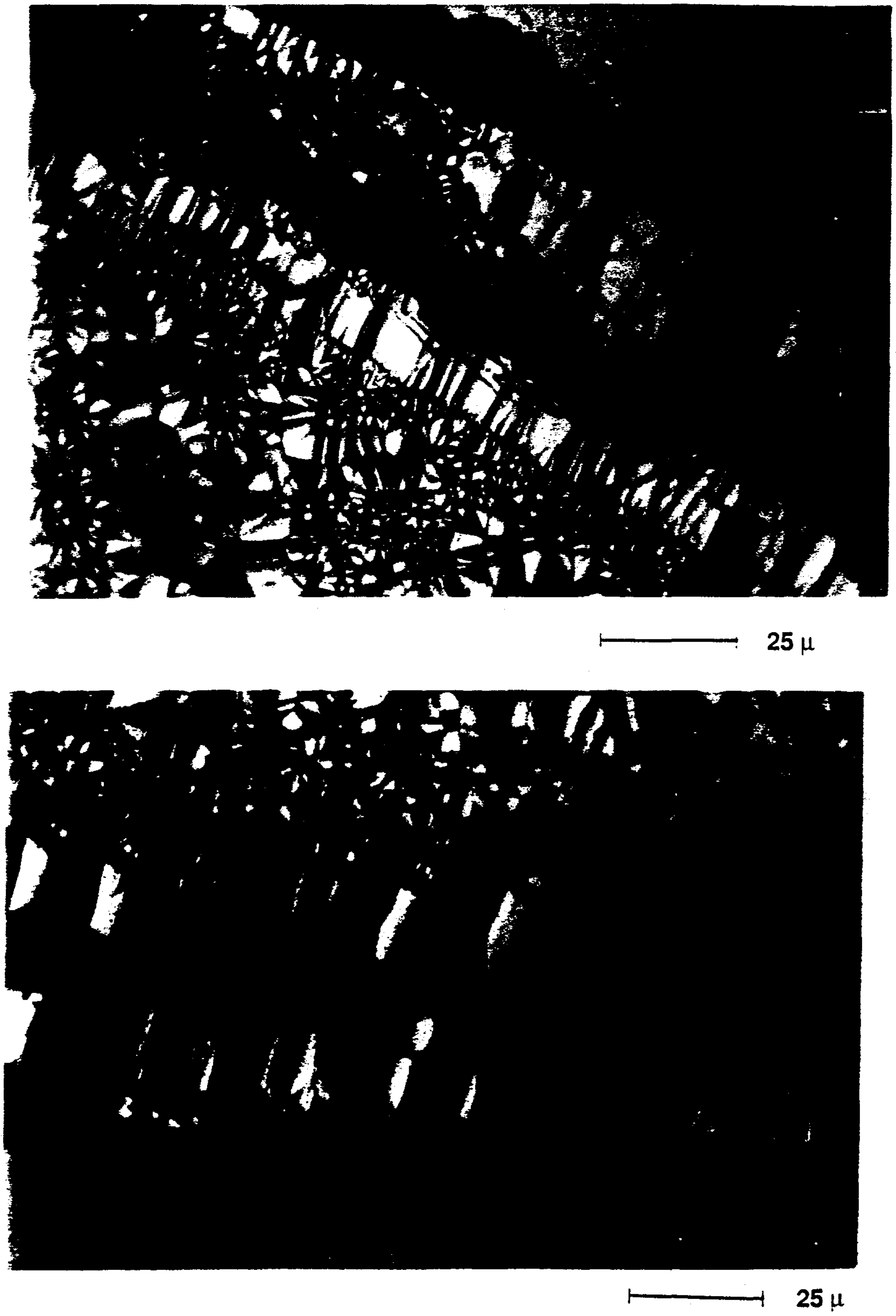

Figure 19. Polarized-Light Micrographs of Deposits on Afterburner Fuel Line.

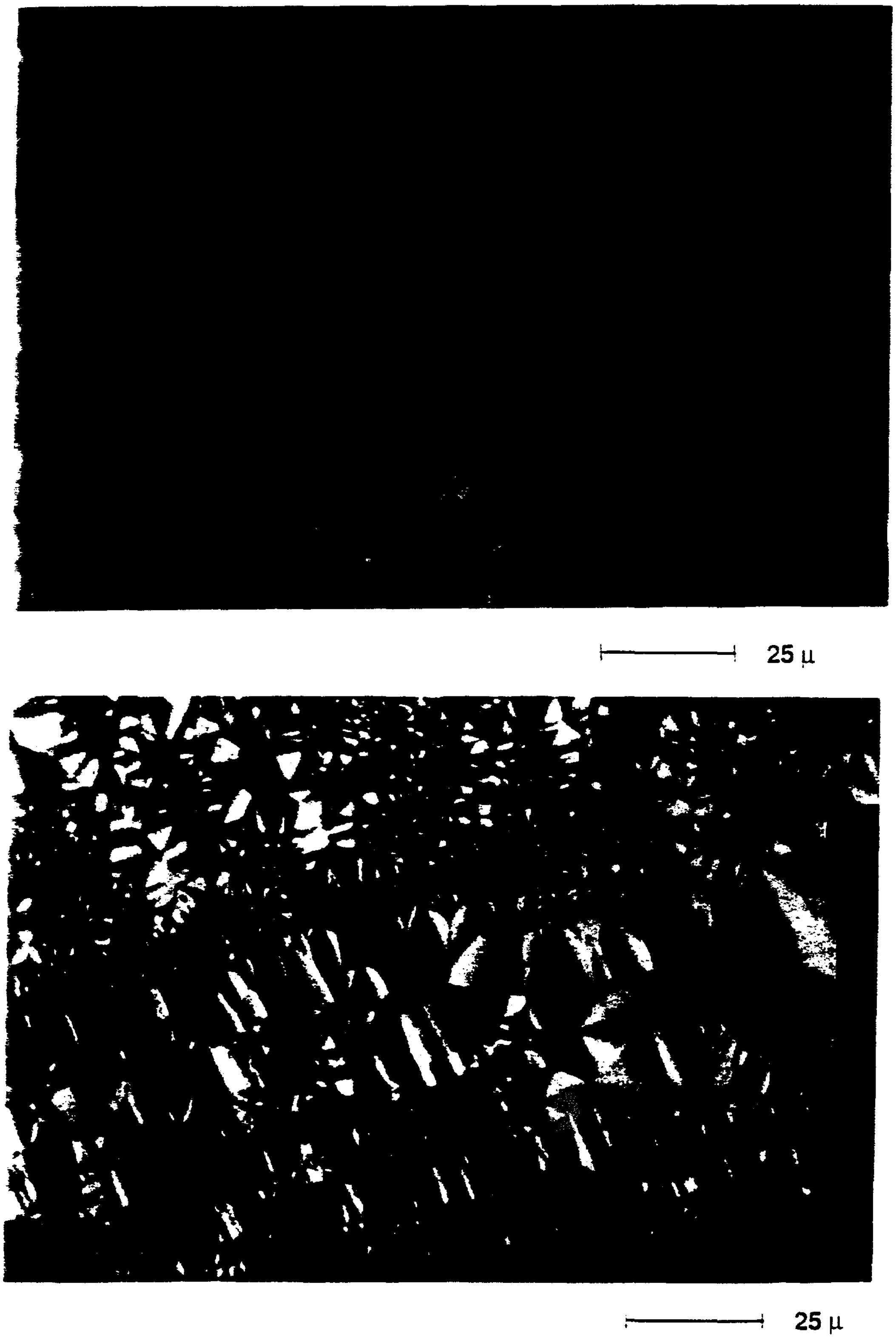

Figure 20. Polarized-Light Micrographs of Deposits on Afterburner Fuel Line.

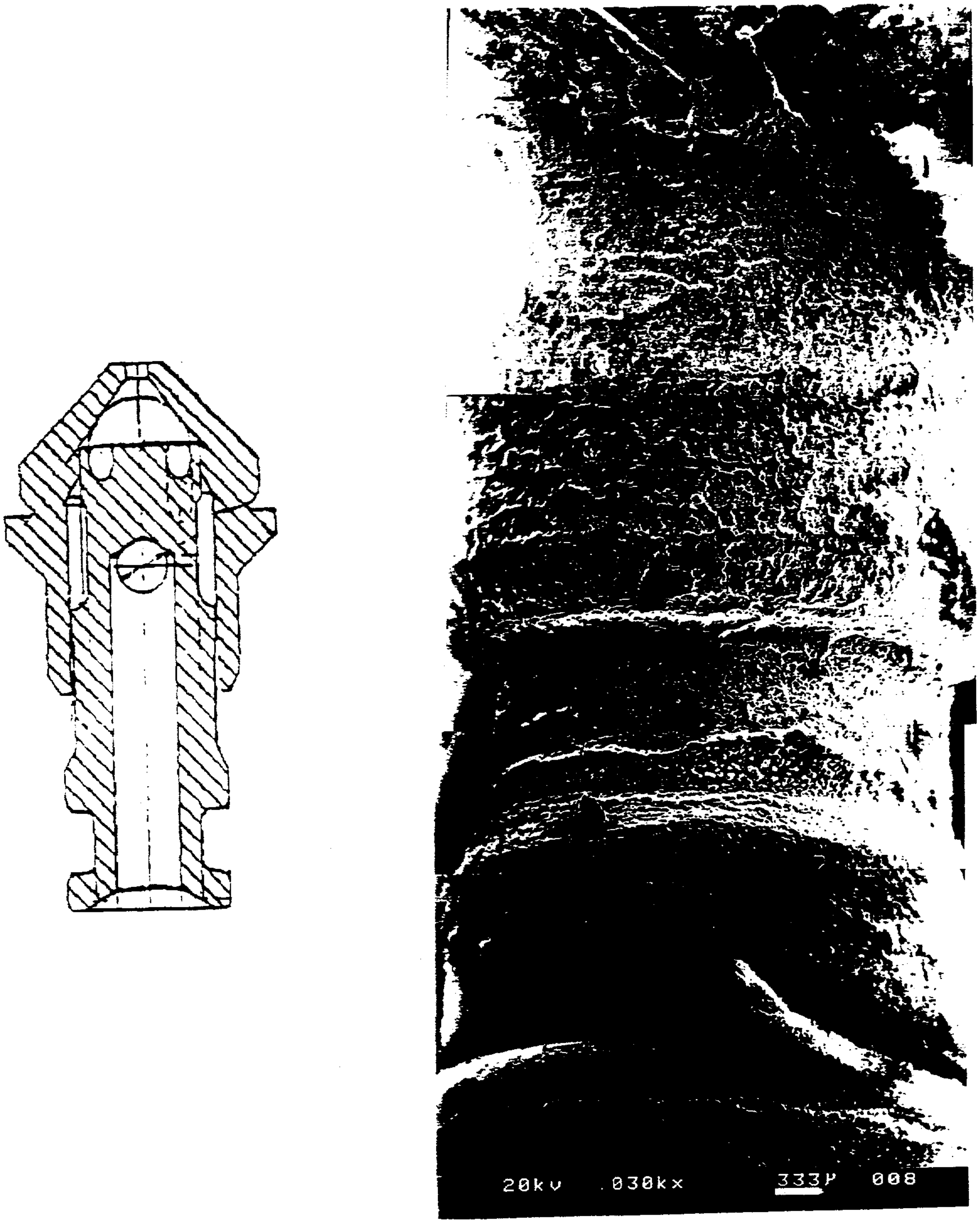

Figure 21. Composite SEM Micrographs of Deposit on the Primary Metering Set.

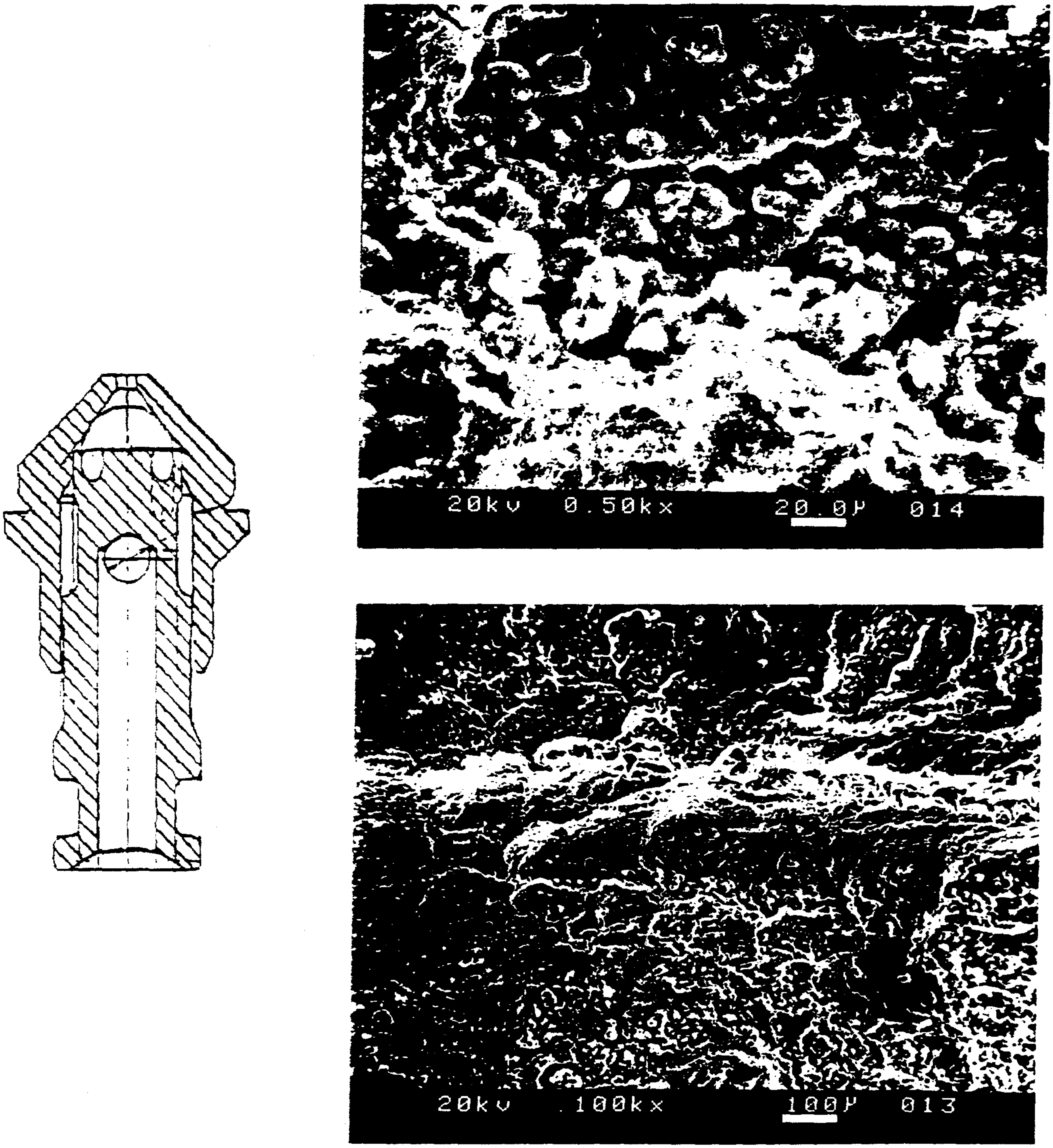

Figure 22. SEM Micrographs of Deposit on the Primary Metering Set.

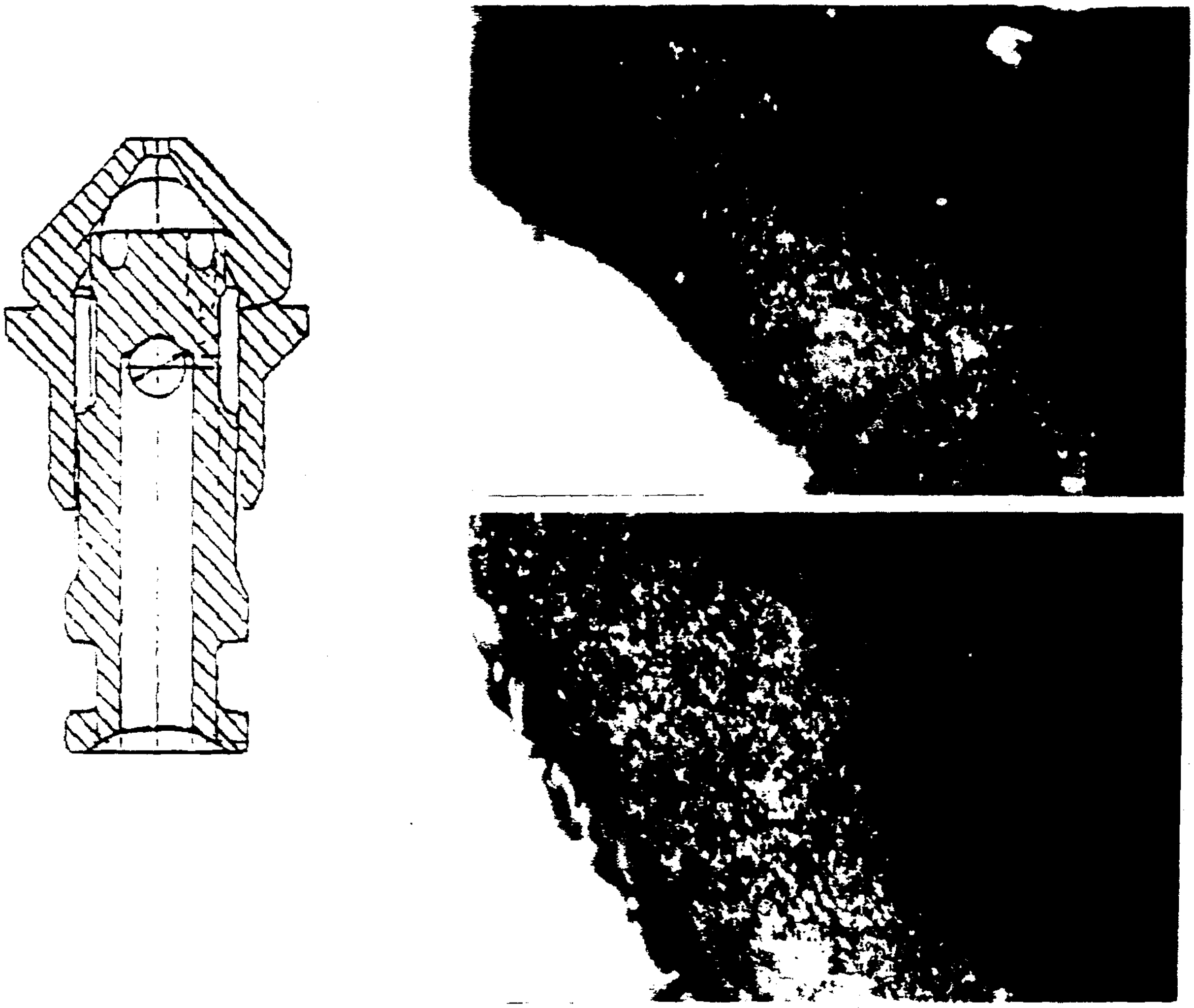

Figure 23. Polarized Light Micrographs of Deposit on Primary Plug near the O-Ring.

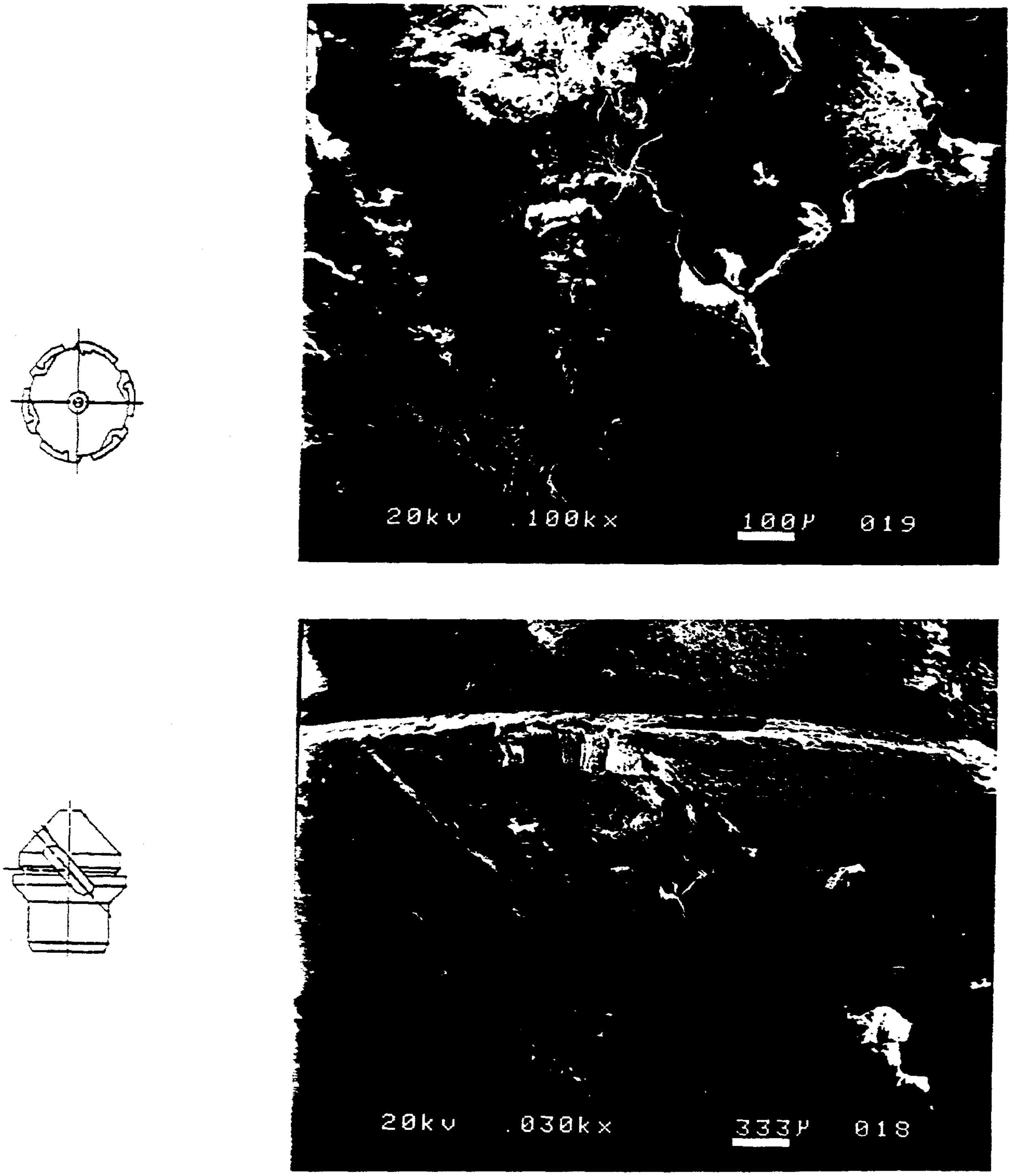

Figure 24. SEM Micrographs of Deposits in the Secondary Spin Slots.

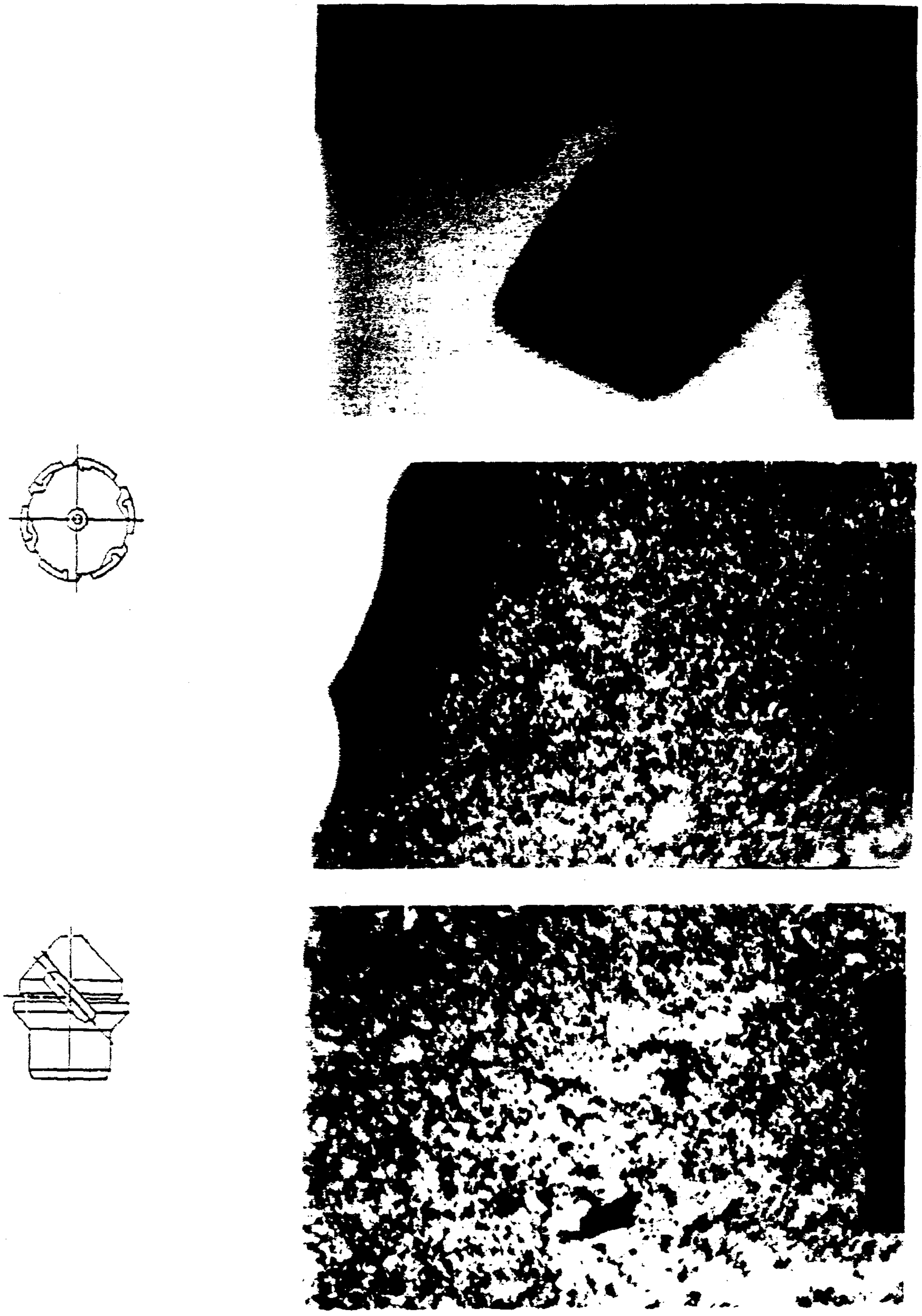

Figure 25. Polarized Light Micrographs of Deposits in the Secondary Spin Slots.

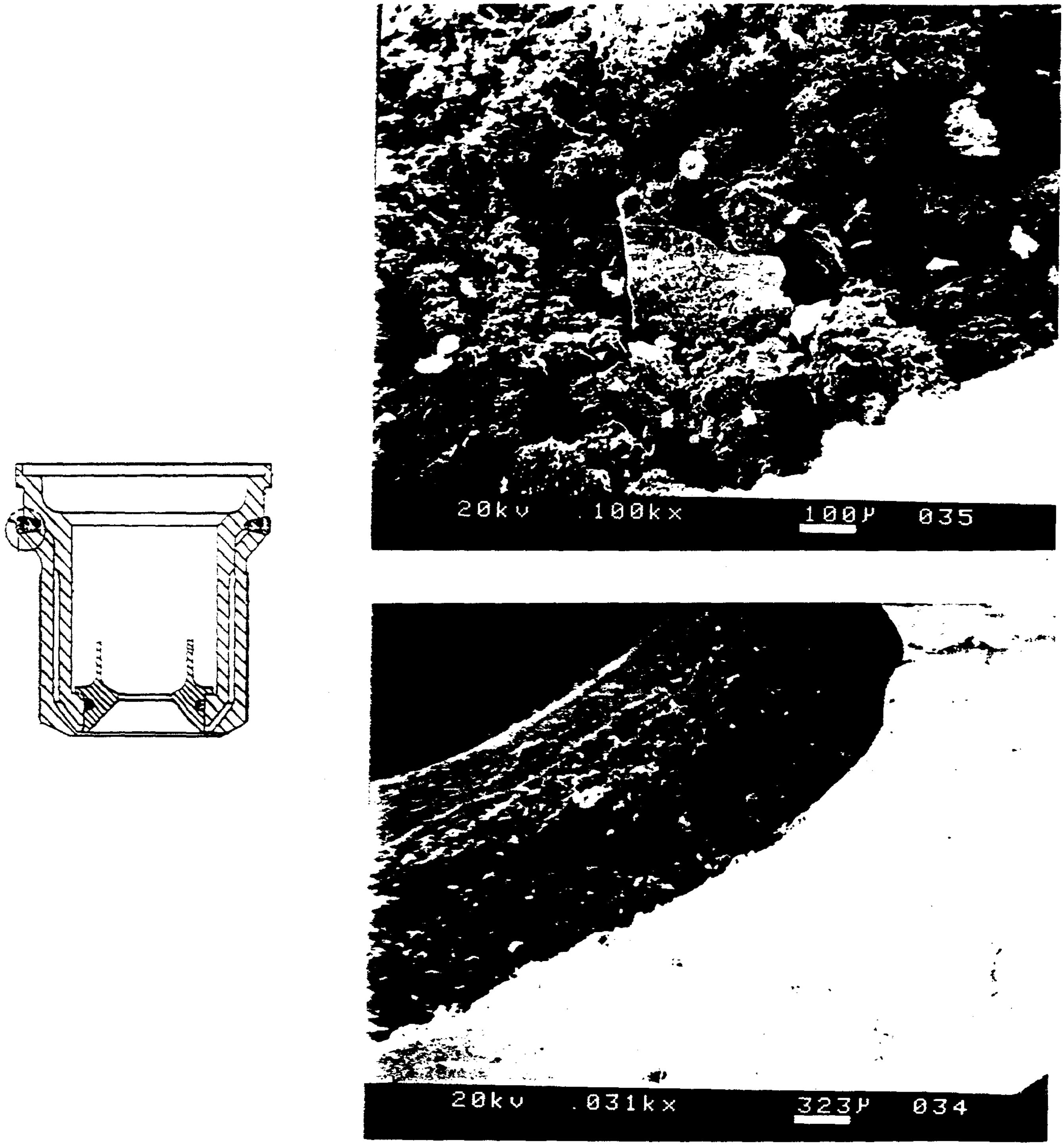

Figure 26. SEM Micrographs of Deposits on the Internal Surface of the Main Tip.

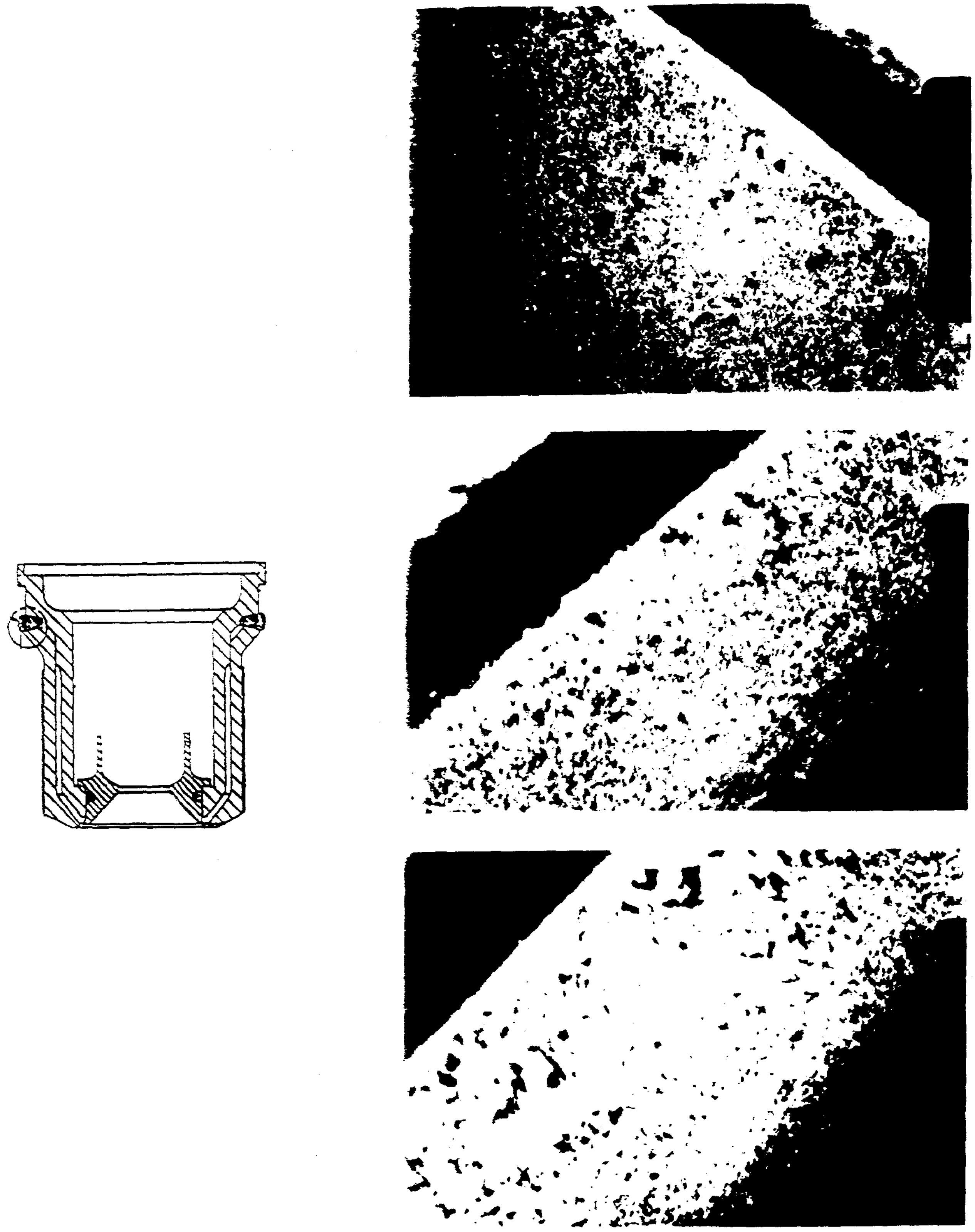

Figure 27. Polarized Light Micrographs of the Cross Section of Deposits the Internal Surface of the Main Tip.

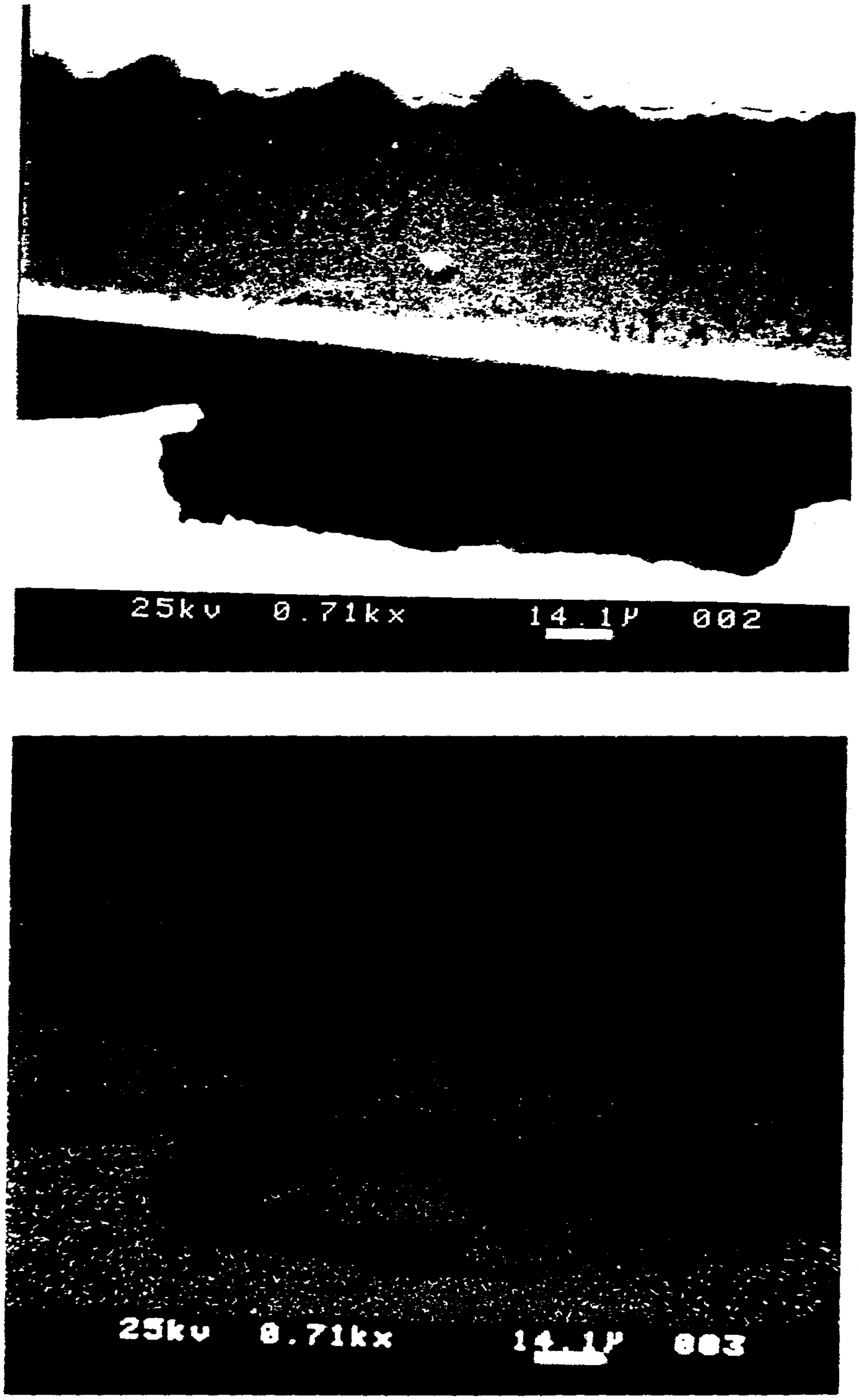

Figure 28. SEM and X-Ray Elemental Mapping (Ni) of the Cross Section of Deposits on the Internal Surface of the Main Tip..

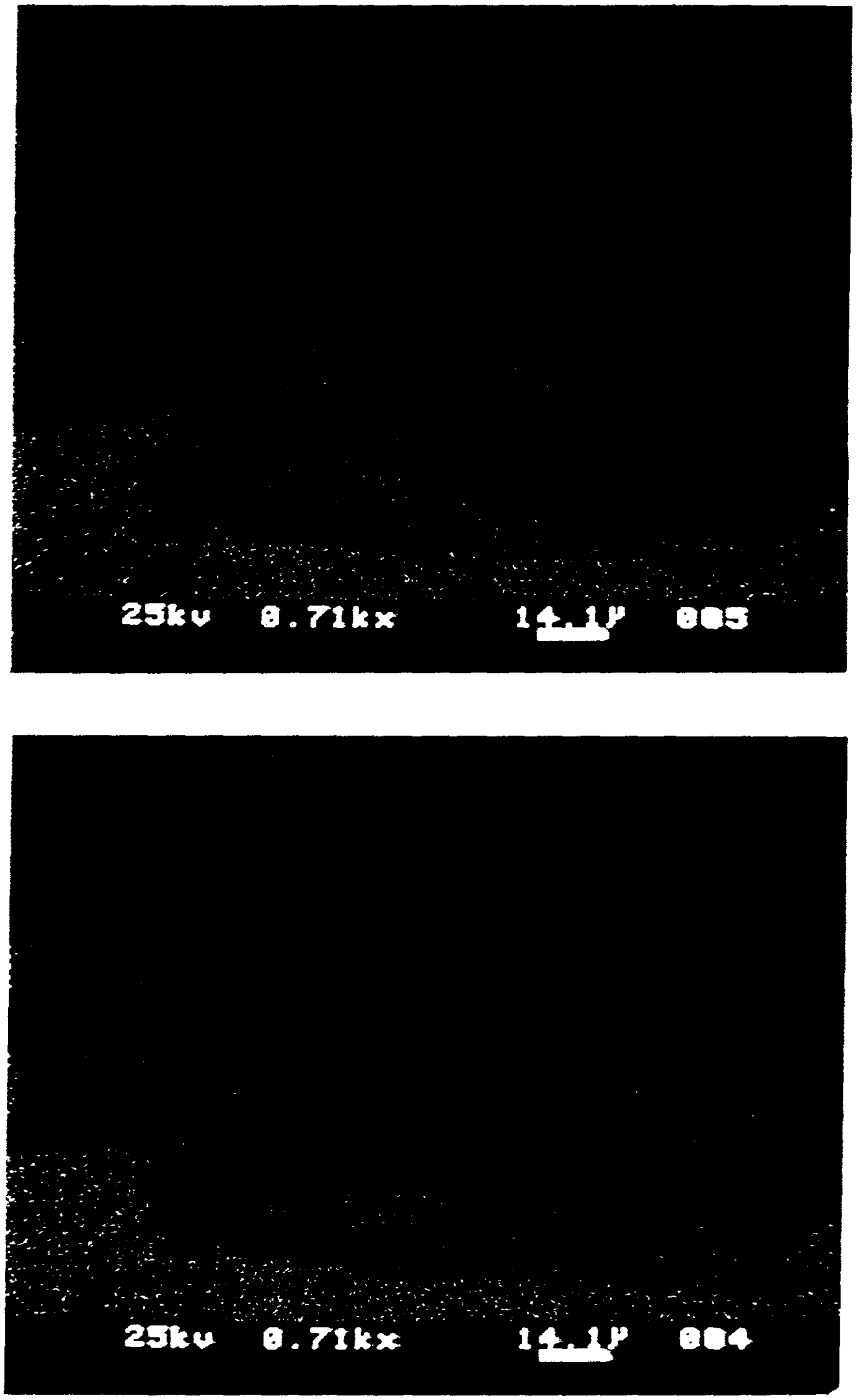

Figure 29. SEM and X-Ray Elemental Mapping (Fe and Cr) of the Cross Section of Deposits on the Internal Surface of the Main Tip..

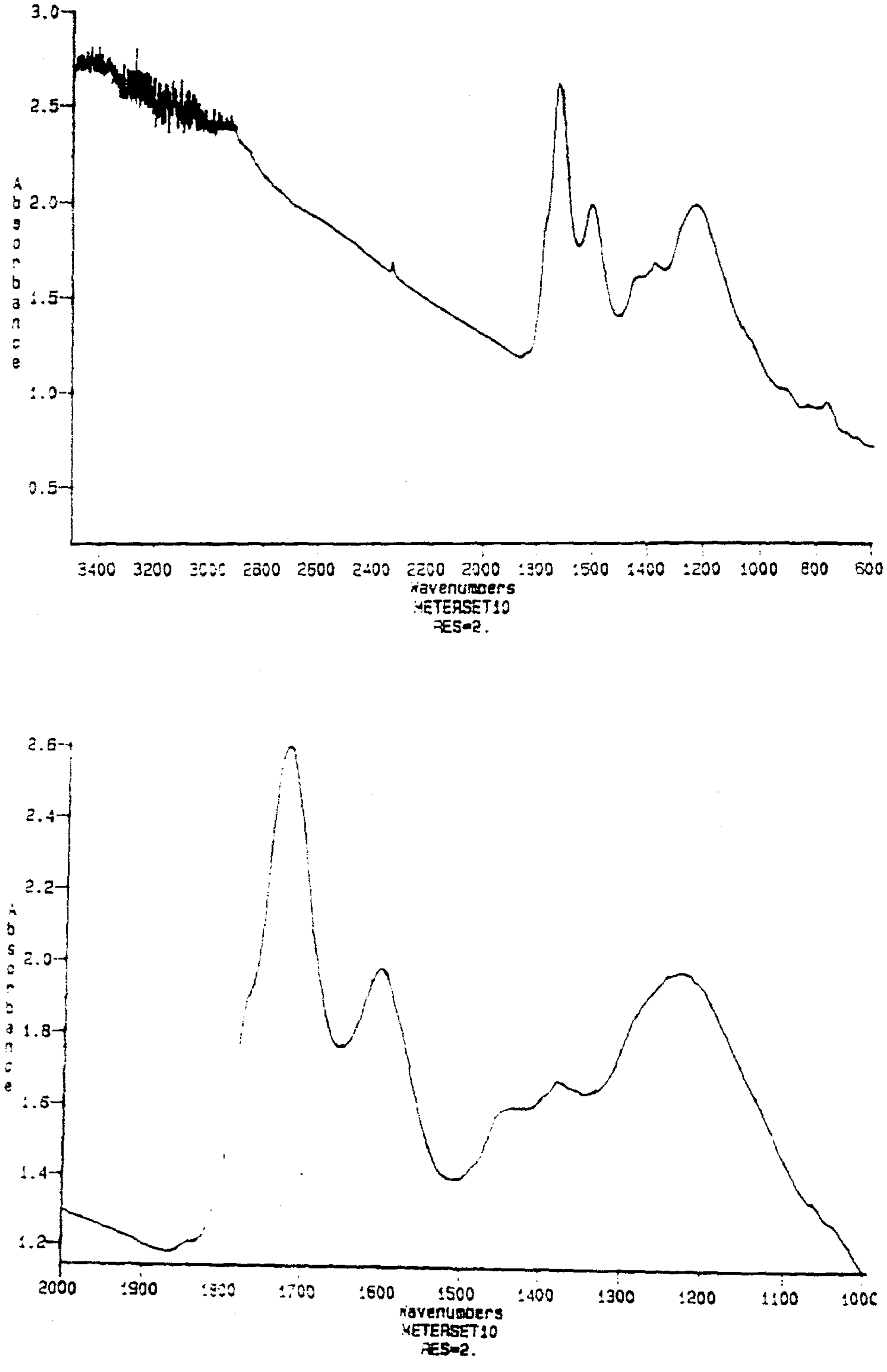

Figure 30. FTIR Spectrum of Deposit Collected from the Primary Metering Set.

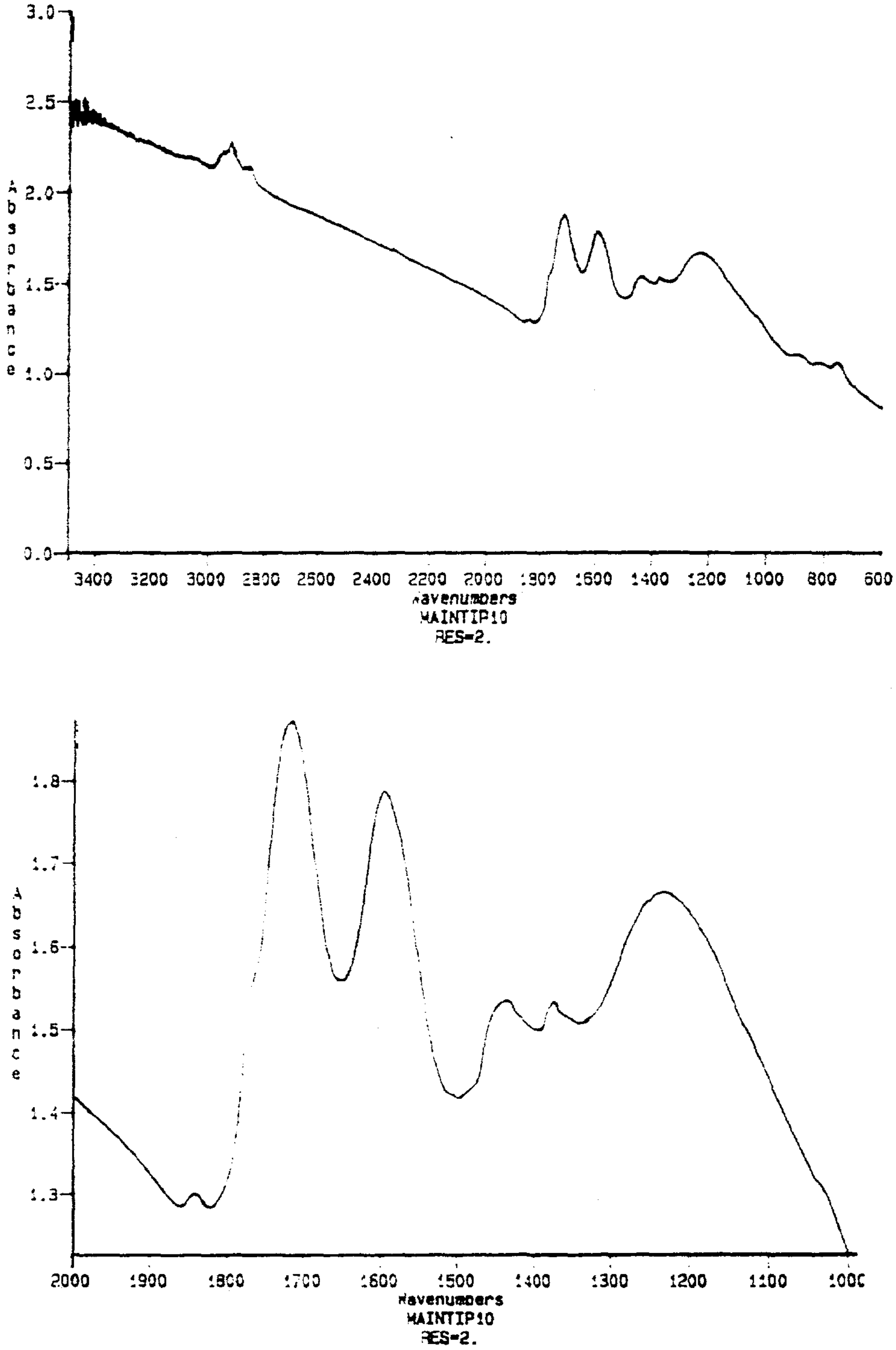

Figure 31. FTIR Spectrum of Deposit Collected from the Internal Surface of the Main Tip.

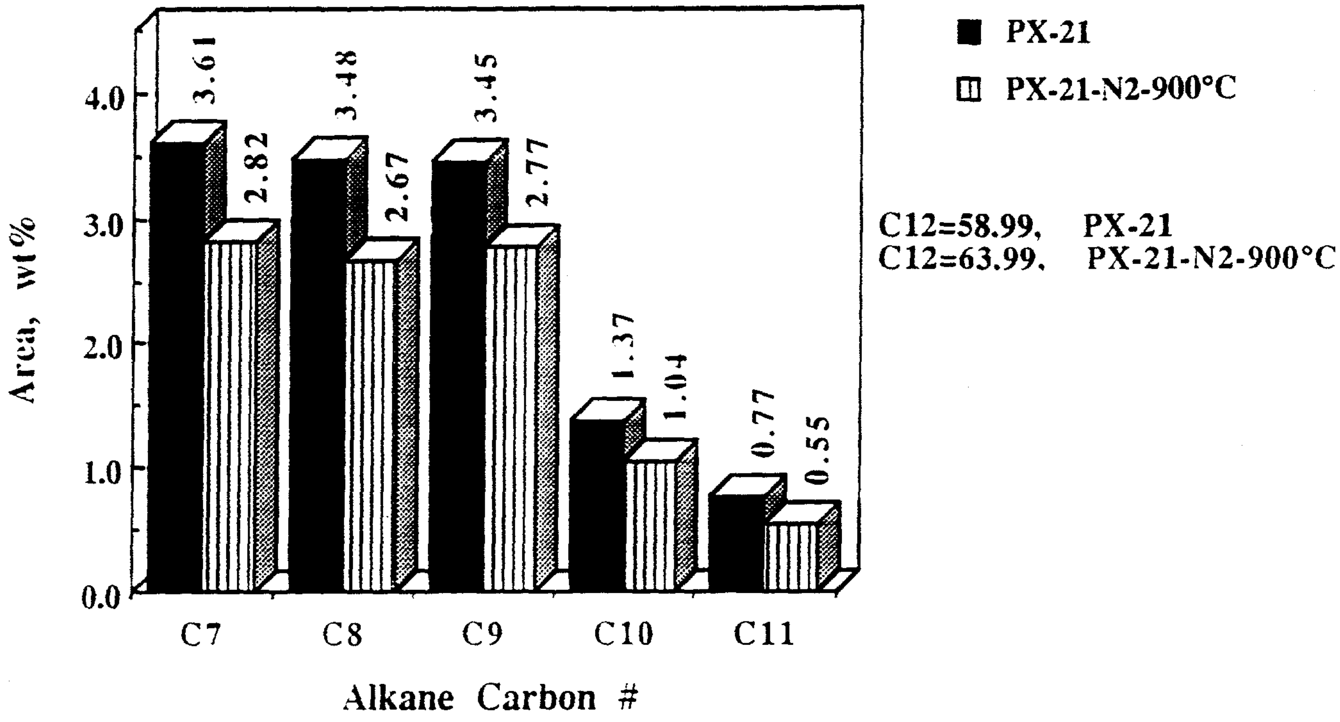

Figure 32. Variations of area percent of n-alkanes in the liquids obtained after thermal stressing of dodecane+5% decalin with PX-21 at 425°C for 1h.

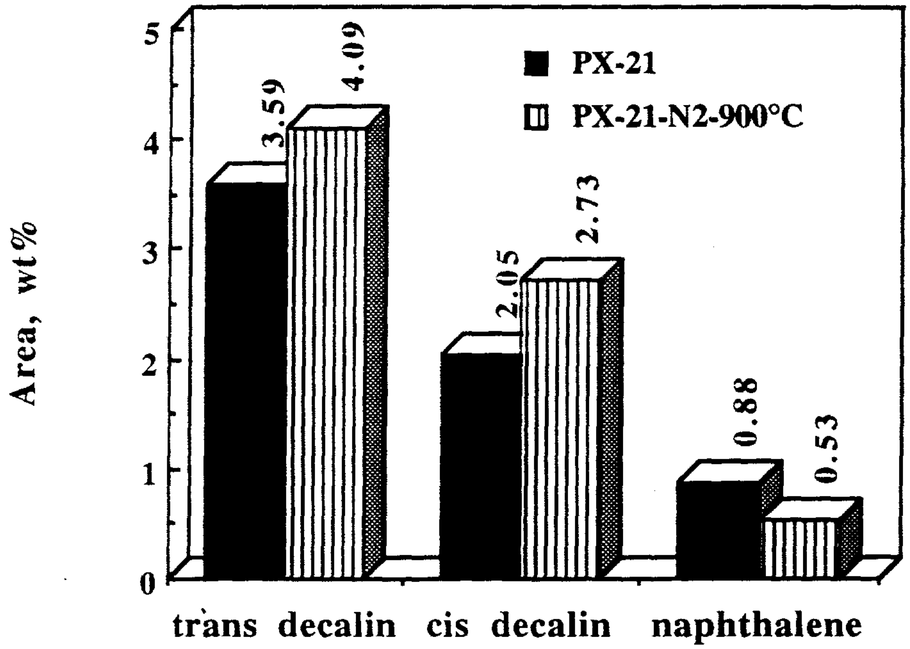

Figure 33. Variation of the area percent of decalin and naphthalene in the liquids obtained after thermal stressing of dodecane+5% decalin with PX-21 at 425°C for 5h.

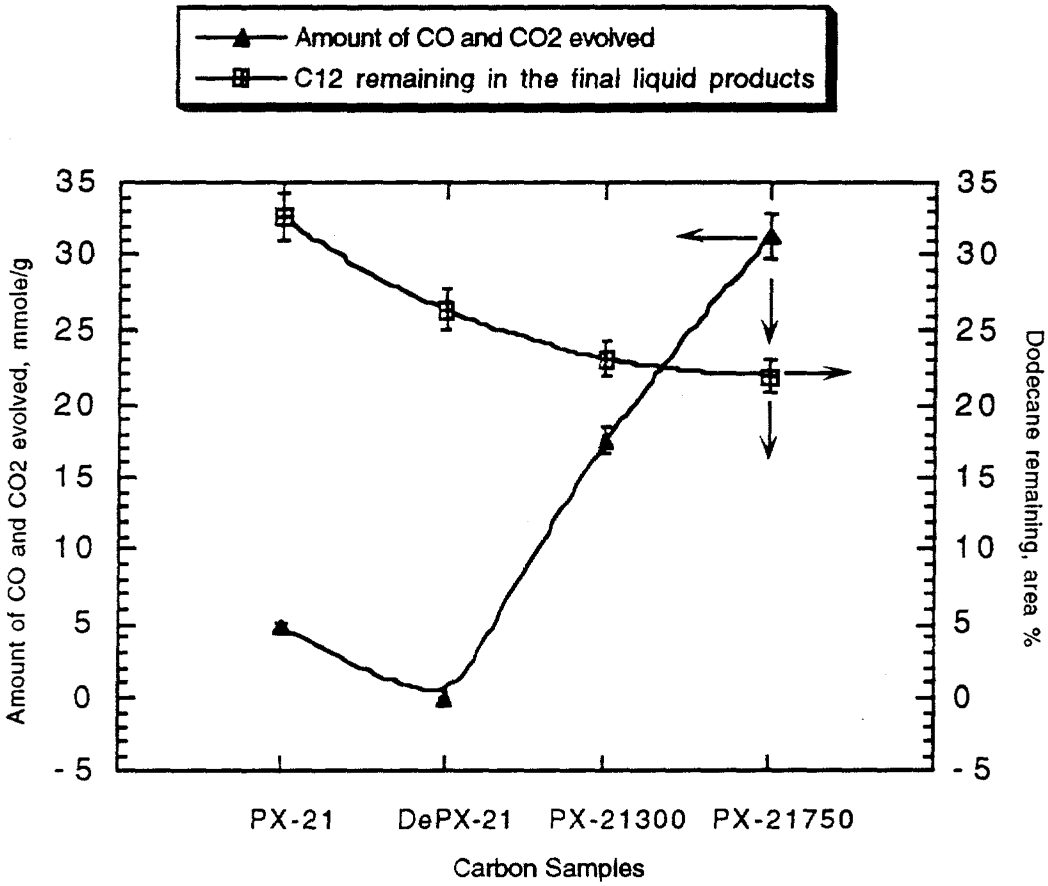

PX-21: Regular PX-21
DePX-21: Degassed PX-21
PX-21300: Oxidized at 300°C for 1 hr
PX-21750: Oxidized at 750°C for few mins

Figure 34. Effect of degassing and oxidation of PX-21 on oxygen functional groups and stabilization of n-dodecane during thermal stressing at 450°C for 4 h.

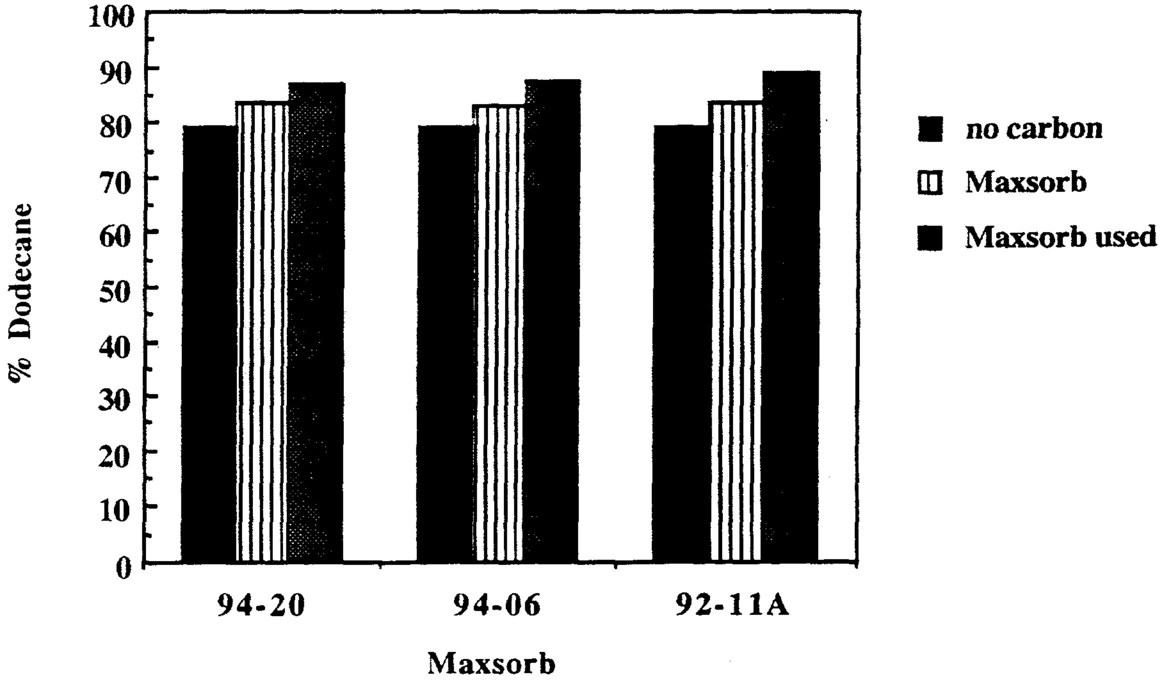

Figure 35. Variation of the area percent of dodecane in the liquids obtained after thermal stressing of Maxsorb 92-11A with dodecane + 5% decalin at 425°C for 1h.

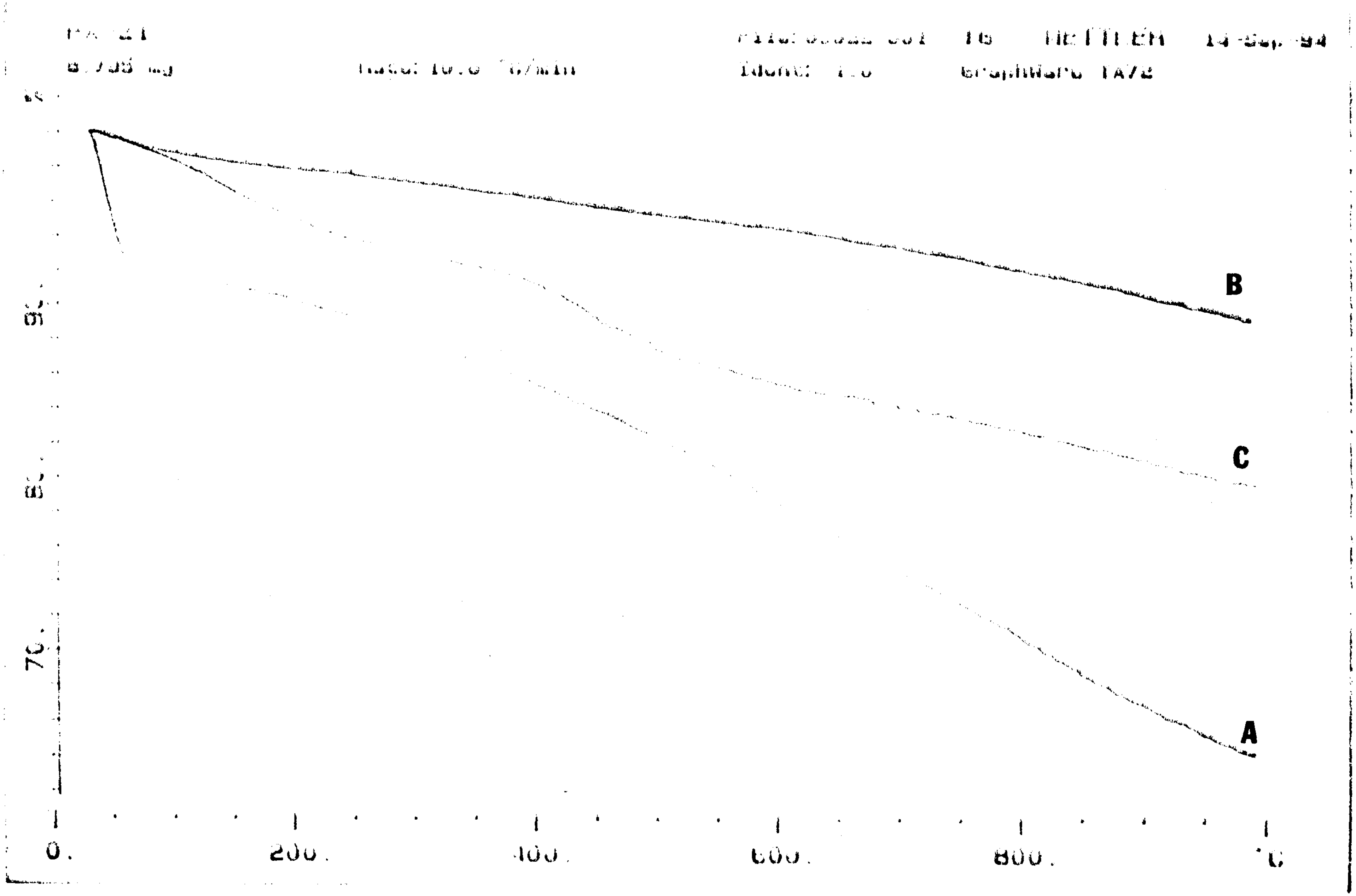

Figure 36. Thermogravimetric Analysis of (A) PX-21, (b) PX-21 Outgassed, (C) PX-21 Stressed with Dodecane+5%Decalin at 425°C for 1h.

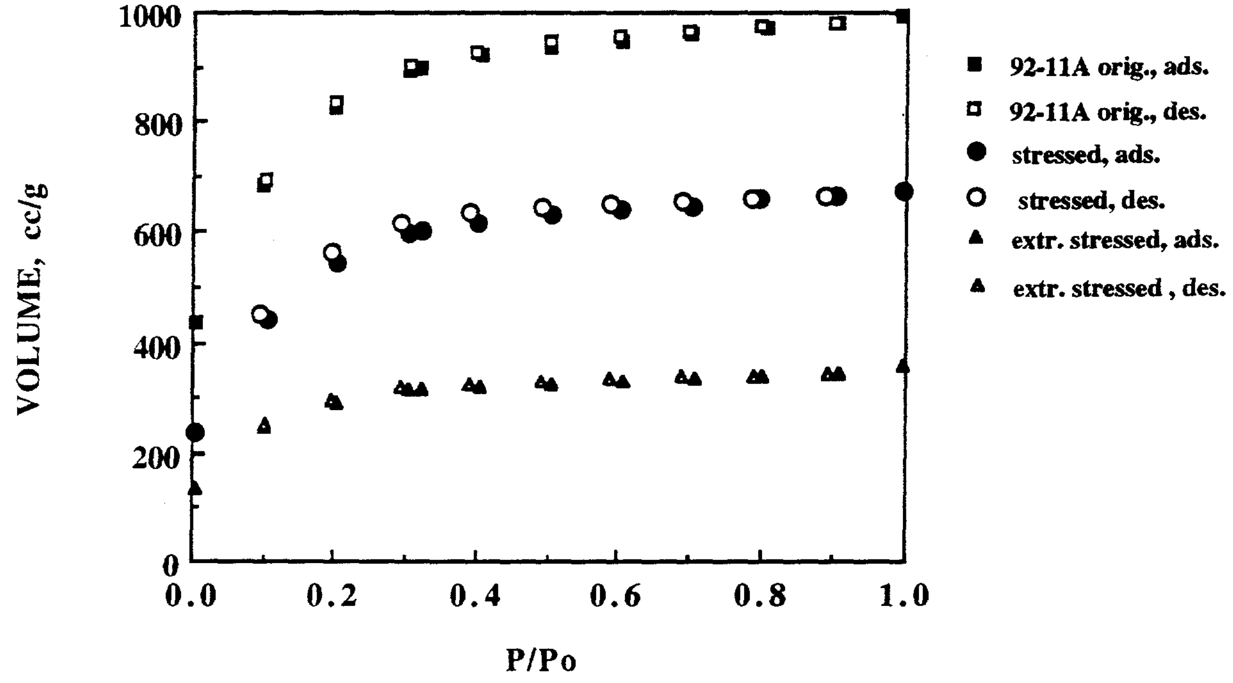

Figure 37. Nitrogen adsorption isotherms of activated carbon Maxsorb 92-11A original, stressed with dodecane+5% decalin, and Maxsorb 92-11A extracted and stressed at 425°C for 1h.

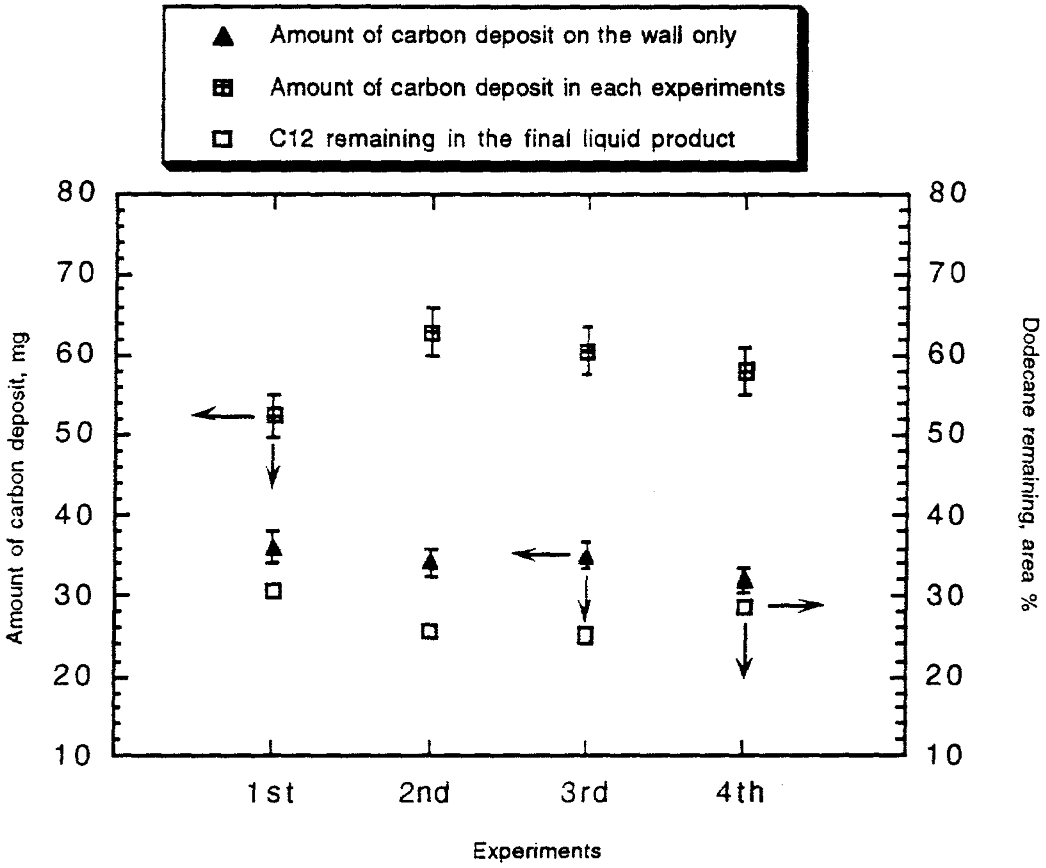

Figure 38. Amount of solid deposits accumulated and n-dodecane remaining in subsequent thermal stressing experiments.

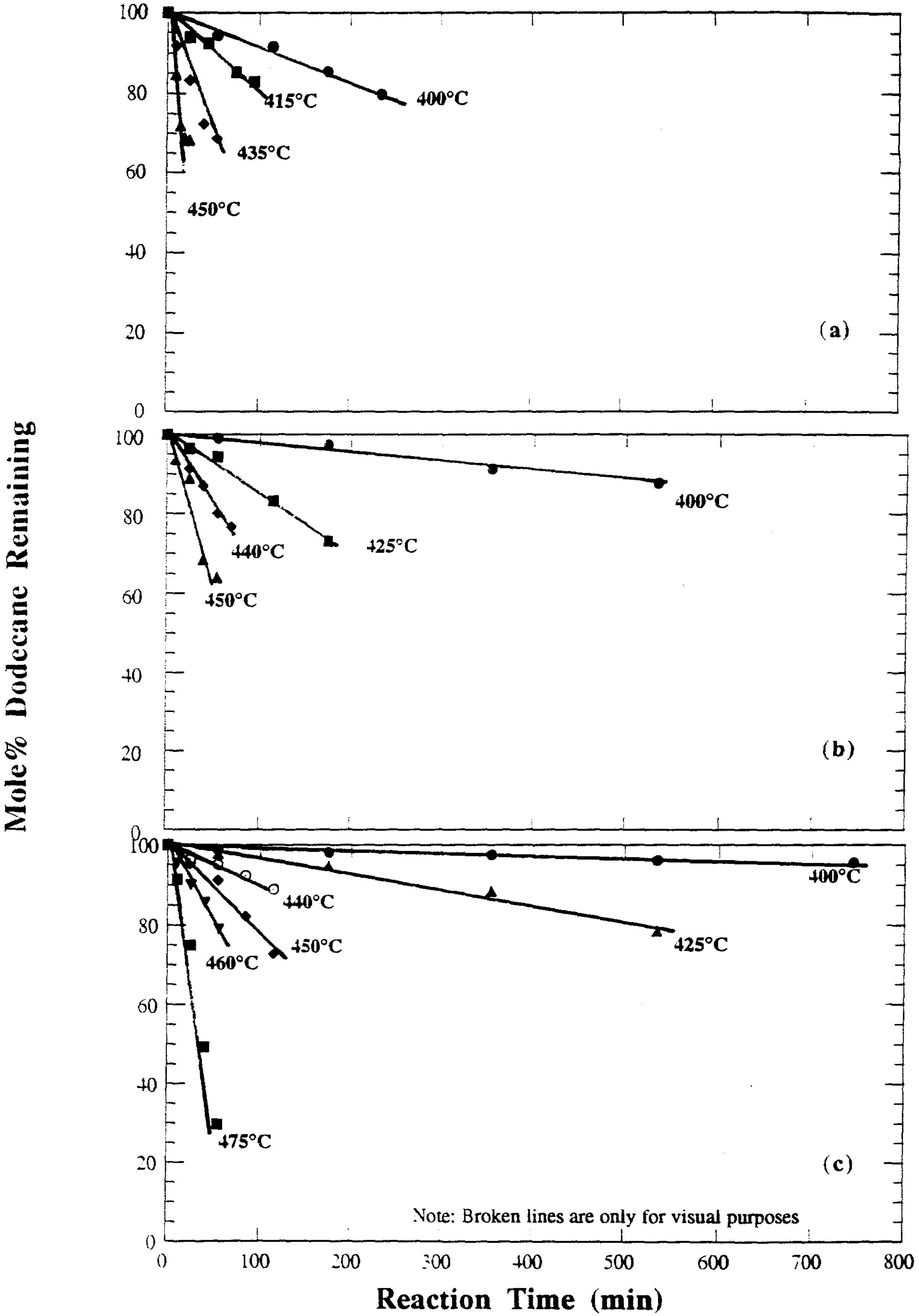

Figure 39. Mole% dodecane remaining after thermal stressing dodecane (a) neat, (b) with 10 mole% benzyl alcohol and (c) with 10 mole% THQ as a function of time

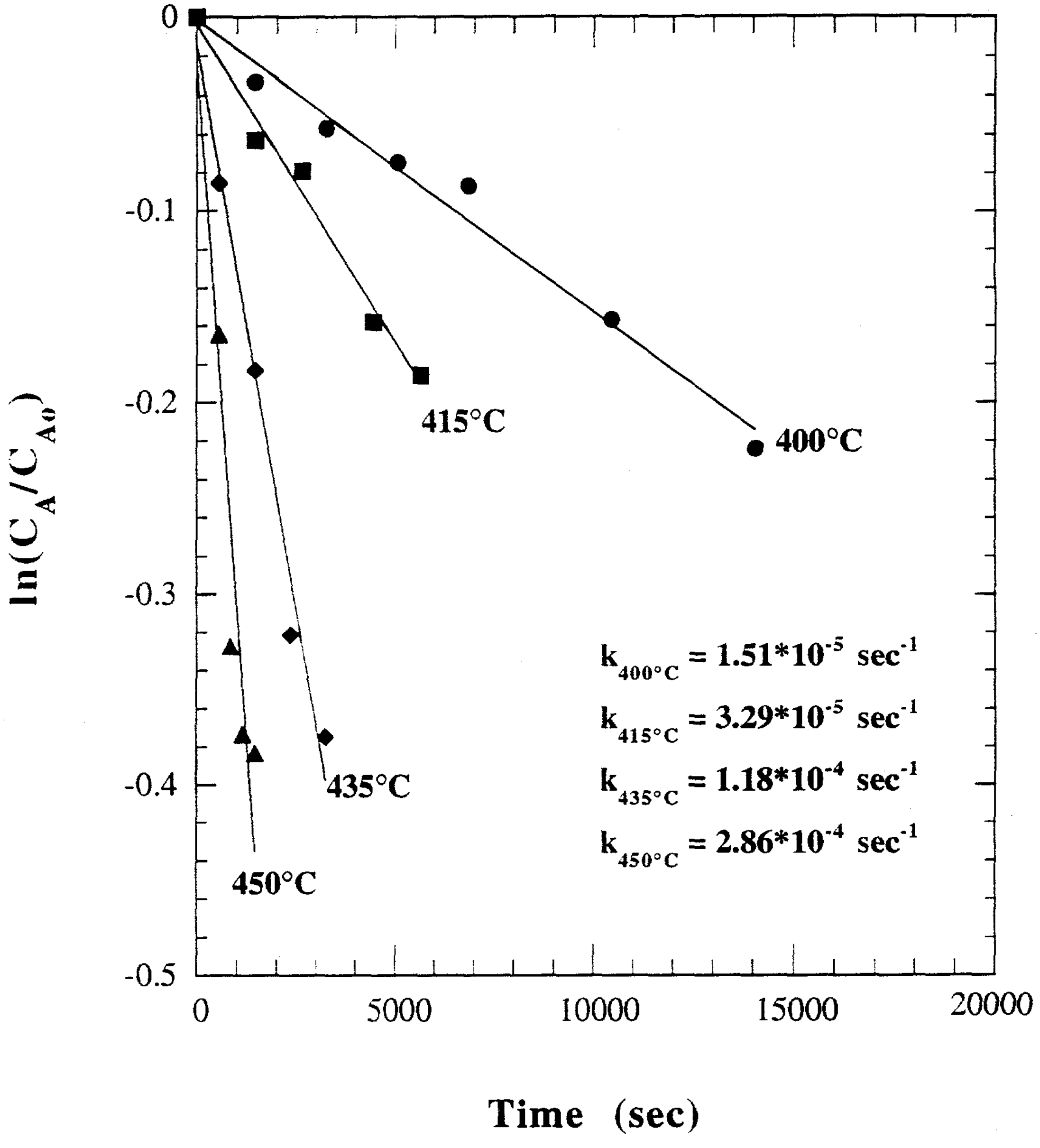

Figure 40. Plot of ln (C_A/C_{Ao}) versus time to determine rate constant k of dodecane neat at 400, 415, 435, and 450°C.

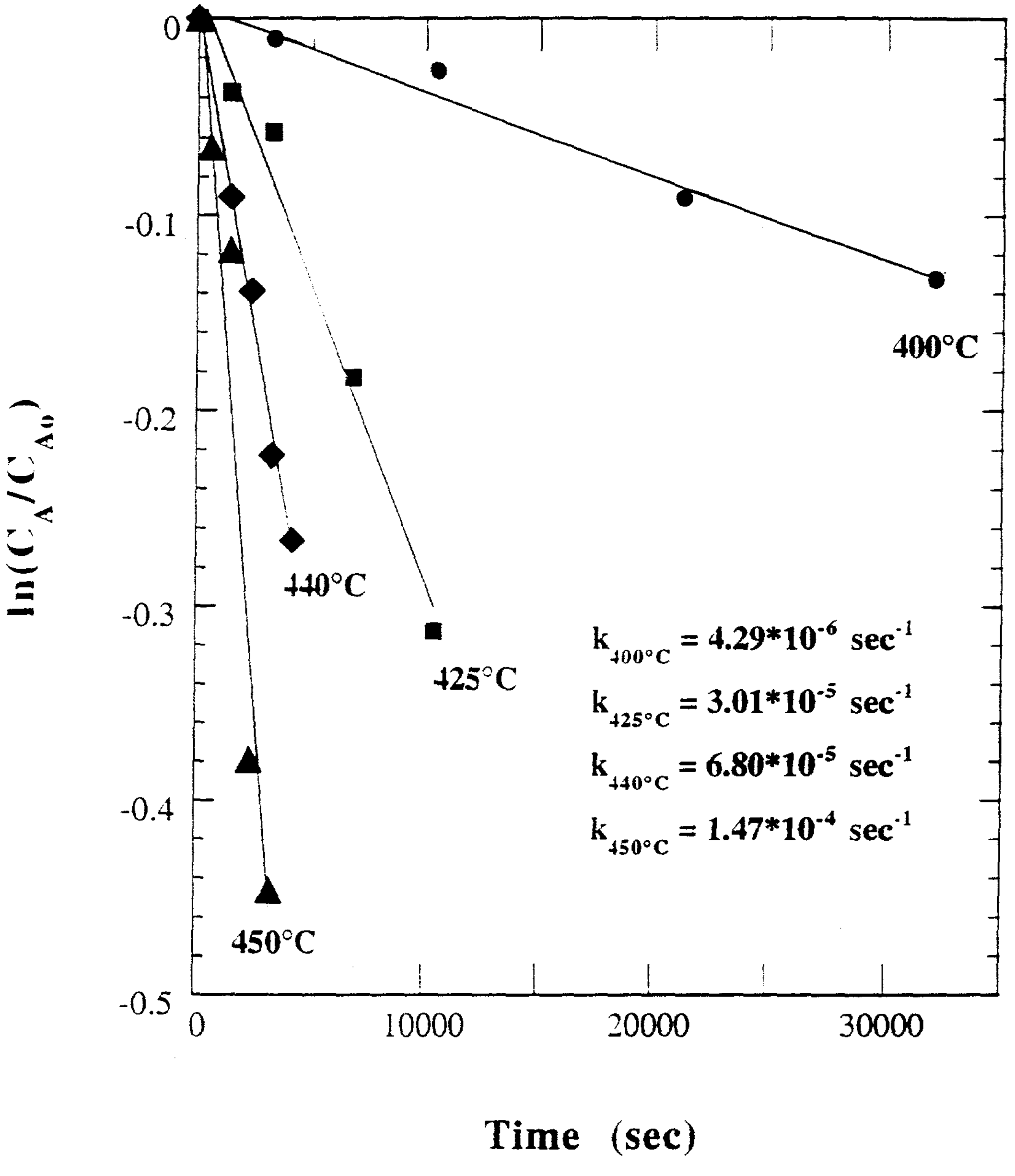

Figure 41. Plot of ln (C_A/C_{Ao}) versus time to determine rate constant k of dodecane/benzyl alcohol mixture (90:10 mol%) at 400, 425, 440, and 450°C.

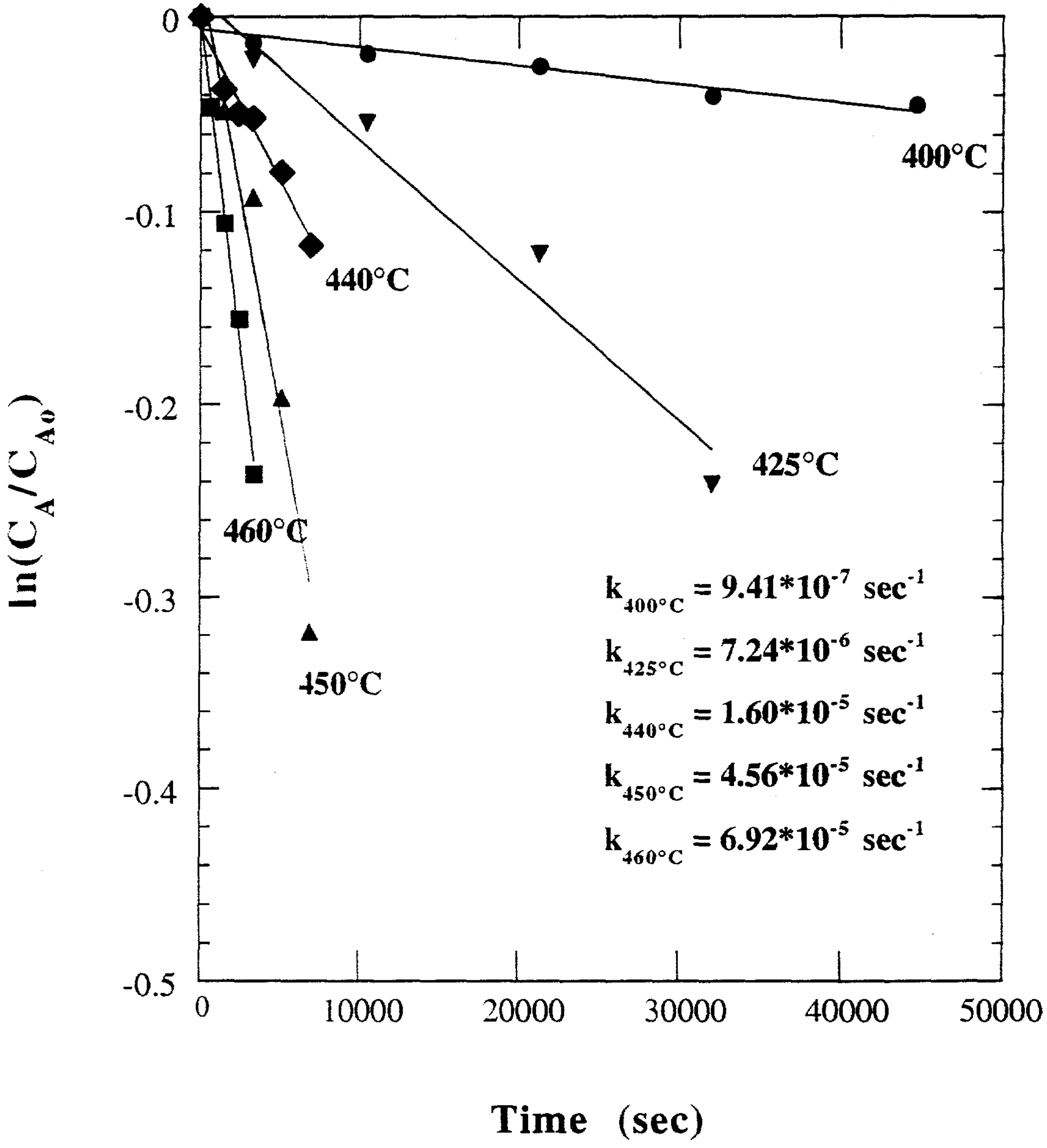

Figure 42. Plot of ln (C_A/C_{Ao}) versus time to determine rate constant k of dodecane/THQ mixtures (90:10 mol%) at 400, 425, 440, 450, and 460°C.

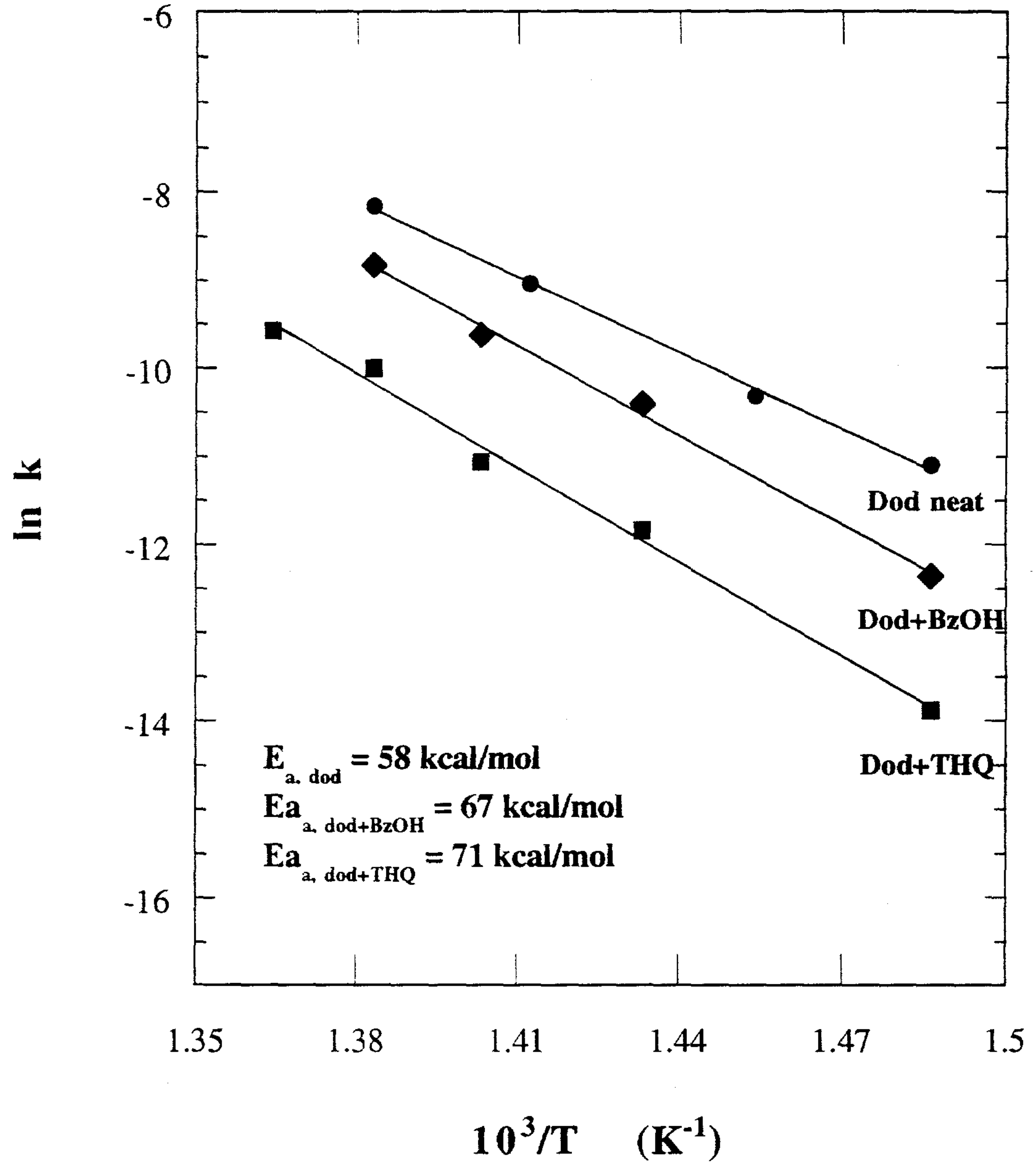

Figure 43. Arrehenius plot of the rate constant k for dodecane degradation.

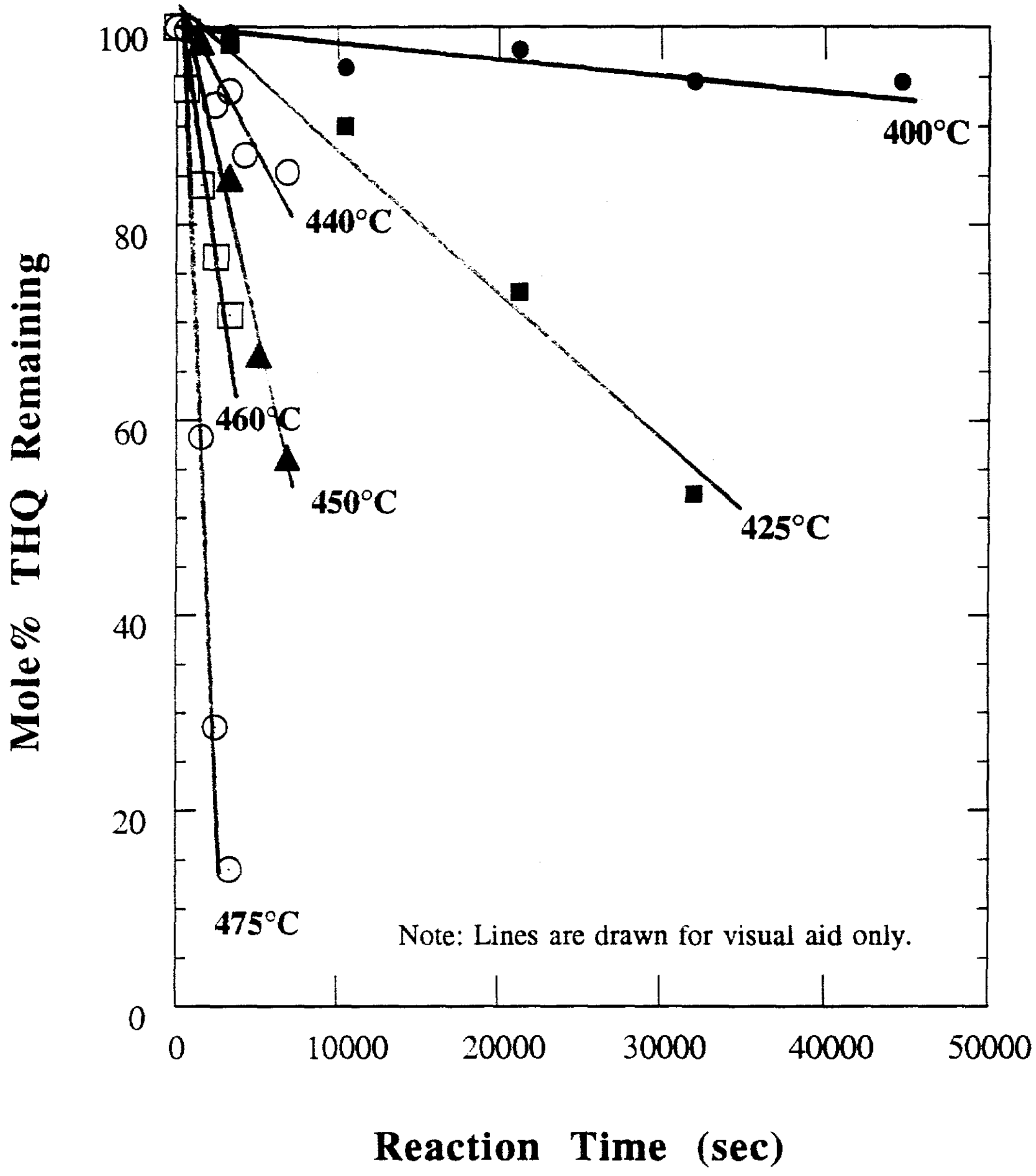

Figure 44. Mole% THQ remaining after thermal stressing in dodecane (Dod+10mol%THQ as a function of temperature.

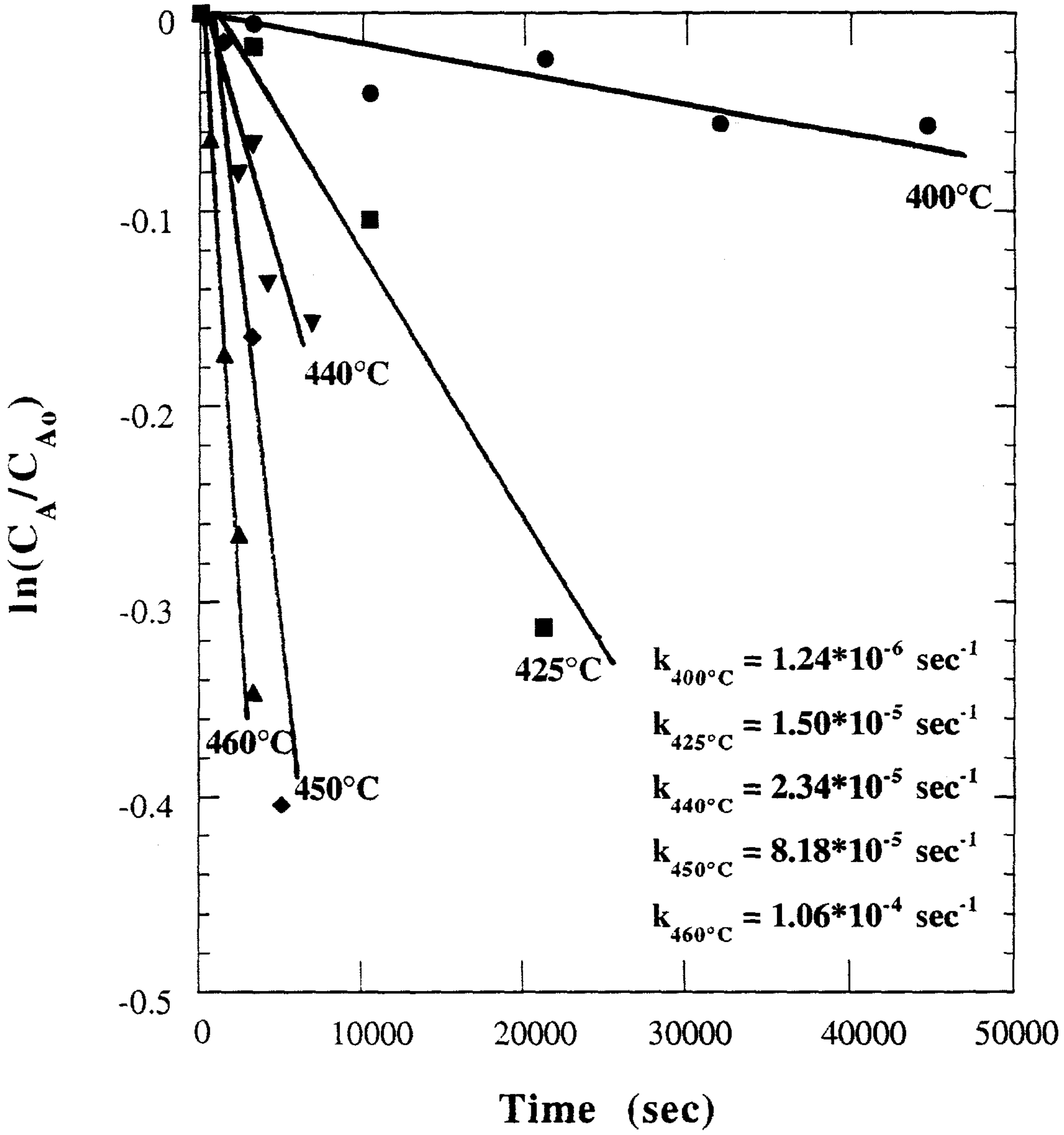

Figure 45. Plot of ln (C_A/C_{Ao}) versus time to determine rate constant k of THQ (10 mol%) disappearance in dodecane at 400, 425, 450, and 460°C.

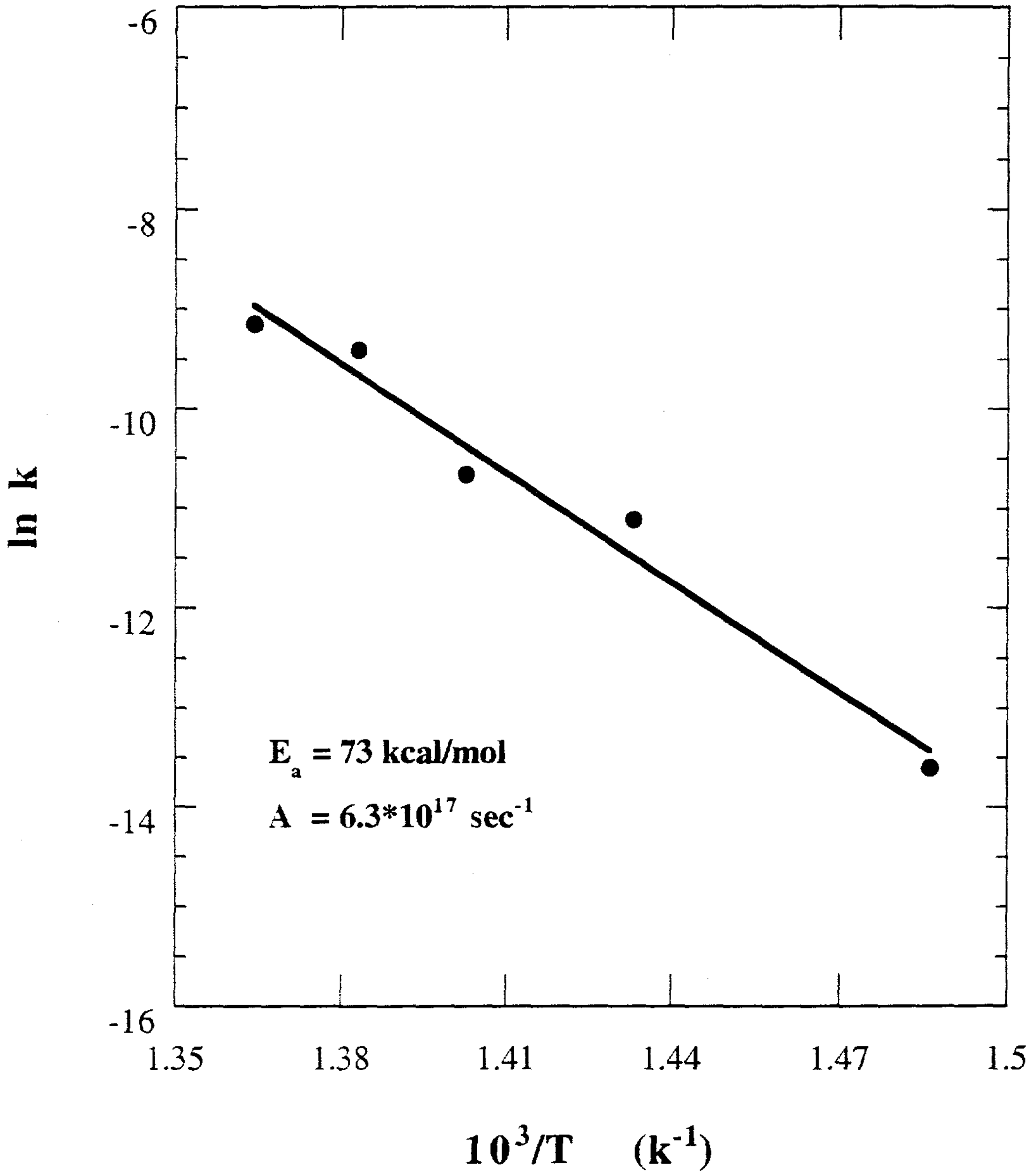

Figure 46. Arrhenius plot of the rate constant k for THQ(10mol%) disappearance in dodecane.

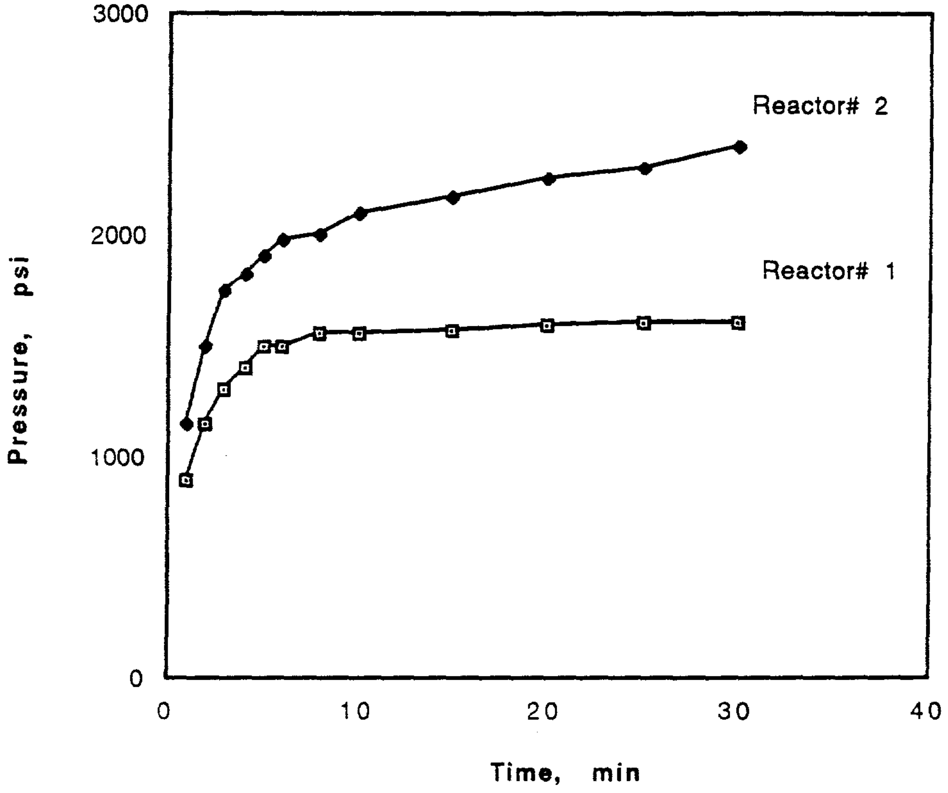

Figure 47. Changes of pressure inside the reactors vs. reaction time.

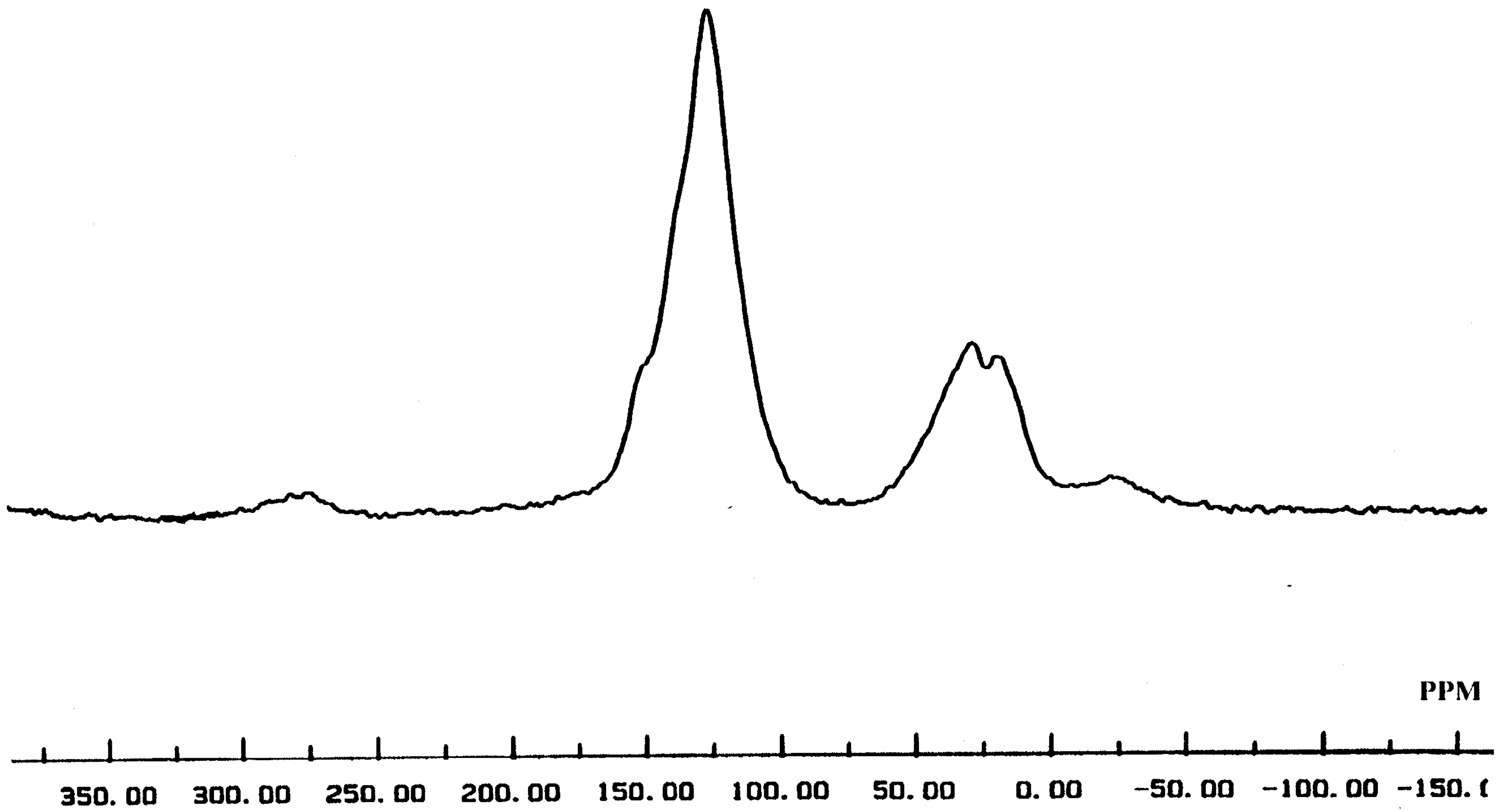

Figure 48. CP/MAS NMR spectrum of Pittsburgh #8 coal sample (original)

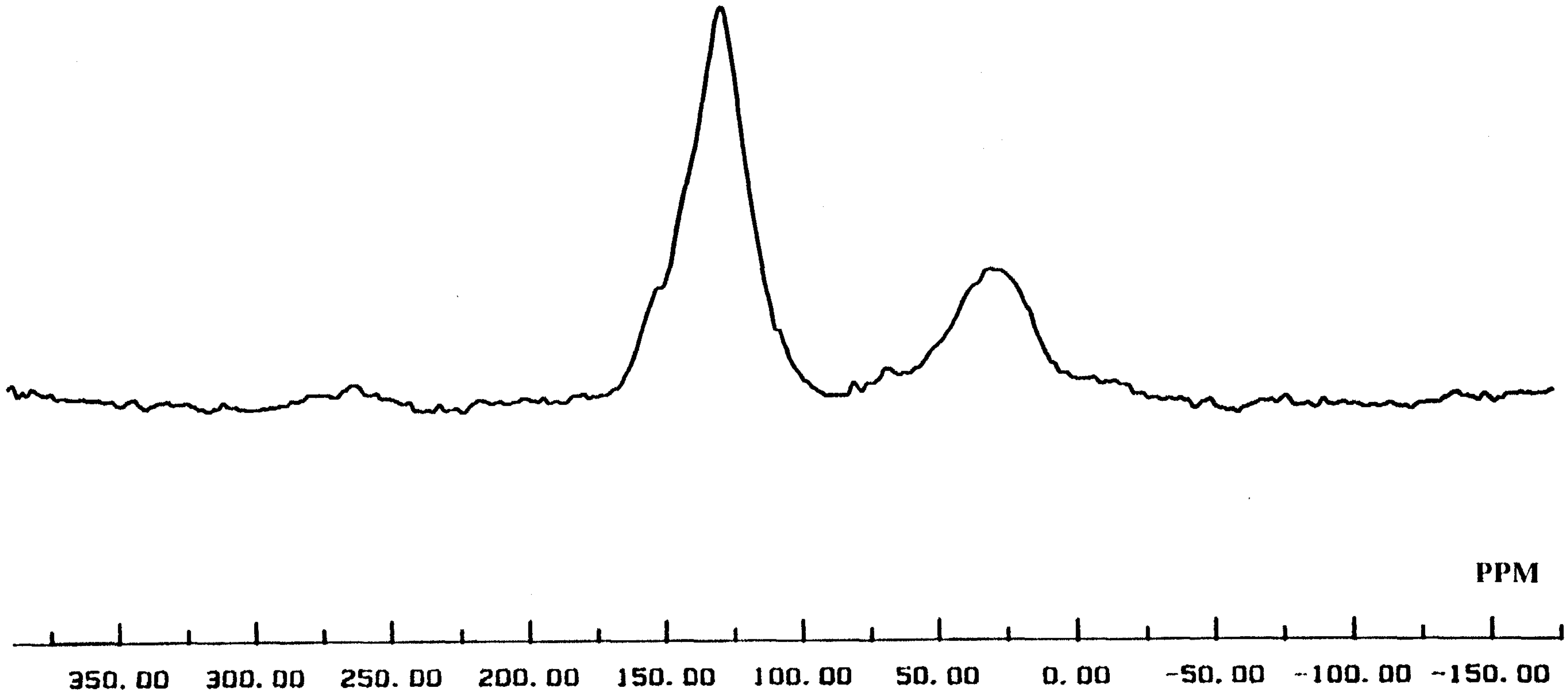

Figure 49. CP/MAS NMR spectrum of Pittsburgh #8 coal sample (treated)

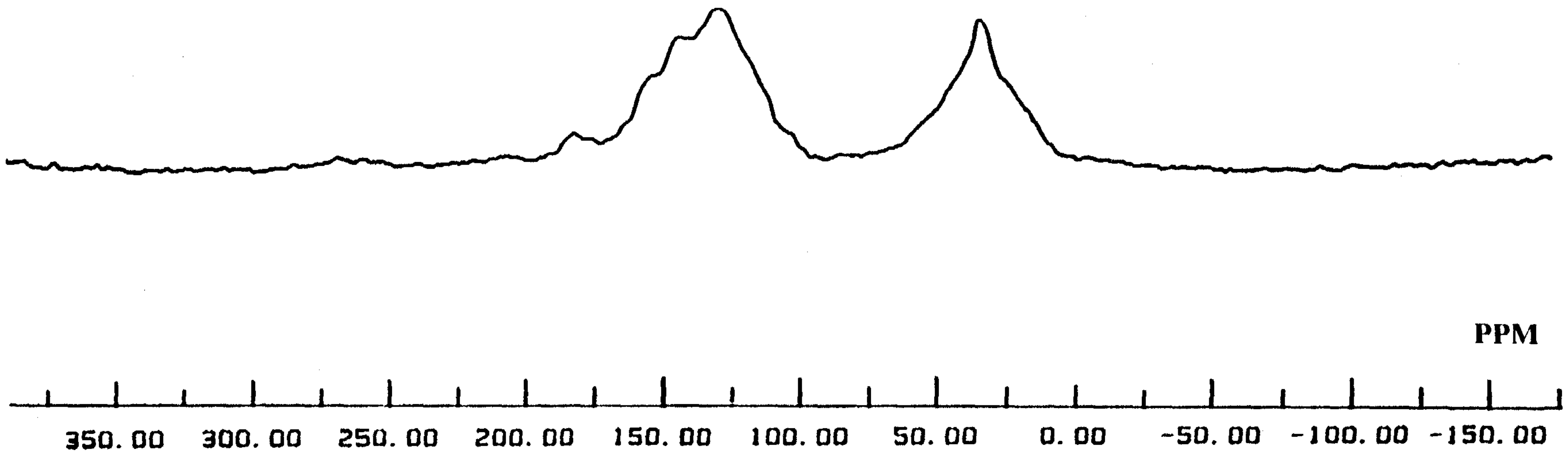

Figure 50. CP/MAS NMR spectrum of Wyodak coal sample (original)

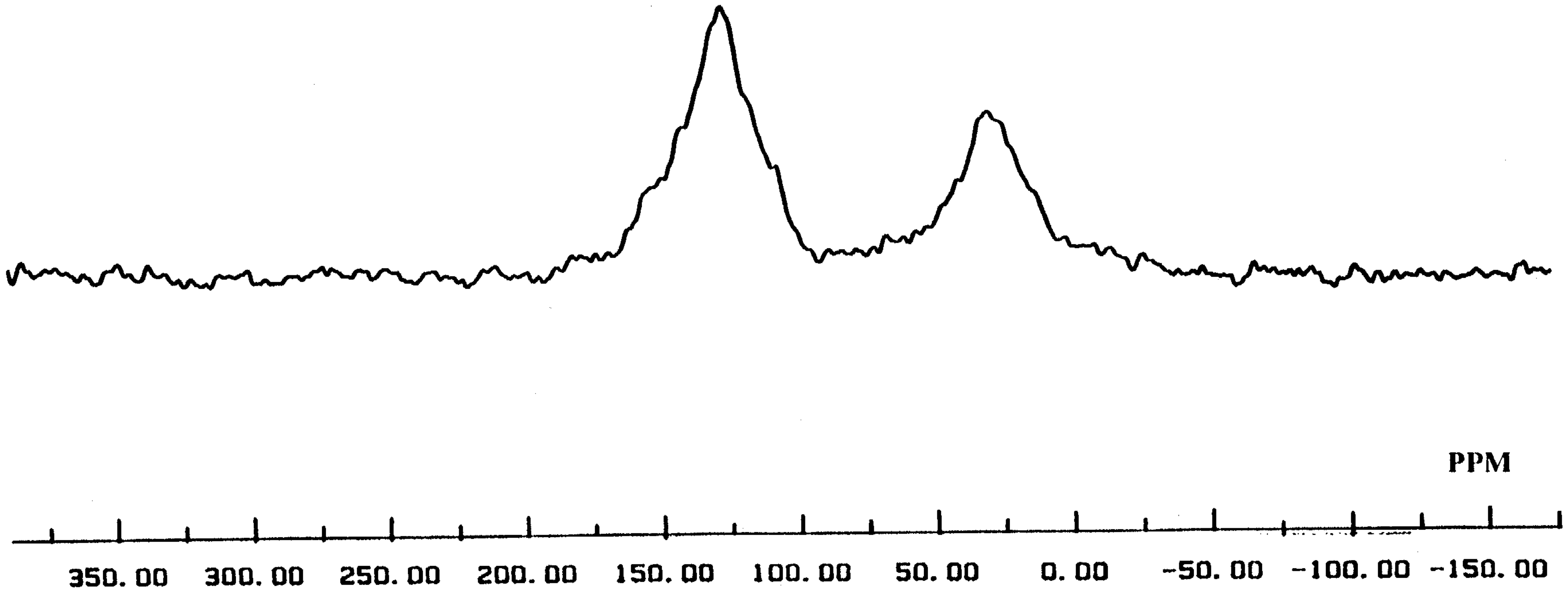

Figure 51. CP/MAS NMR spectrum of Wyodak coal sample (treated)

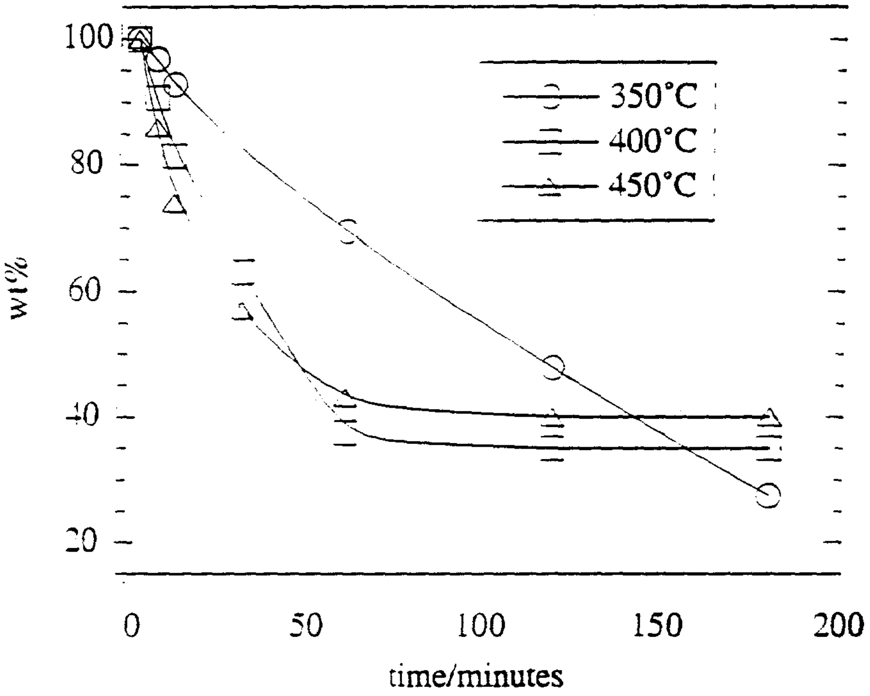

Figure 52 Effect of temperature on naphthalene to tetralin conversion during hydrogenation.

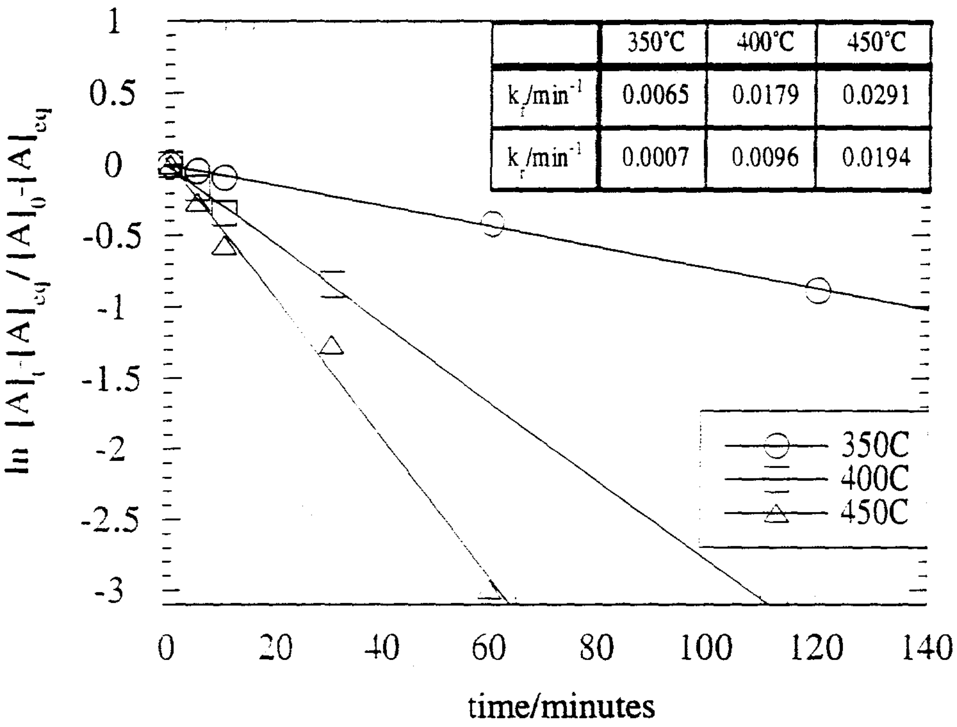

	350°C	400°C	450°C
k_f/min^{-1}	0.0065	0.0179	0.0291
k_r/min^{-1}	0.0007	0.0096	0.0194

Figure 53. Naphthalene hydrogenation kinetics at 350, 400 and 450°C.

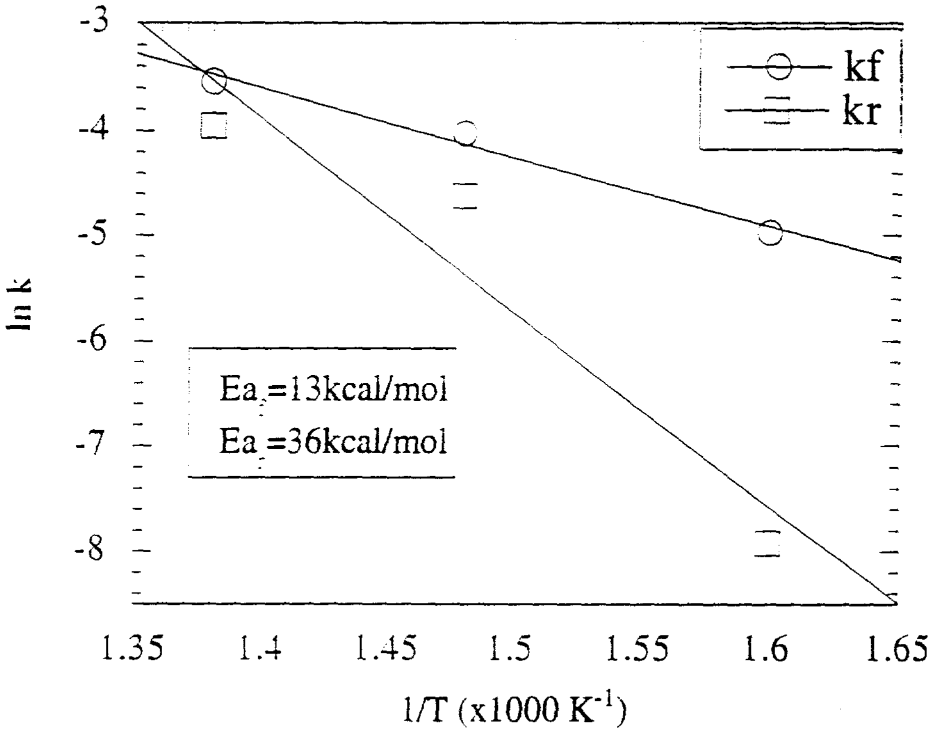

Figure 54. Naphthalene hydrogenation/dehydrogenation Arrhenius plot.

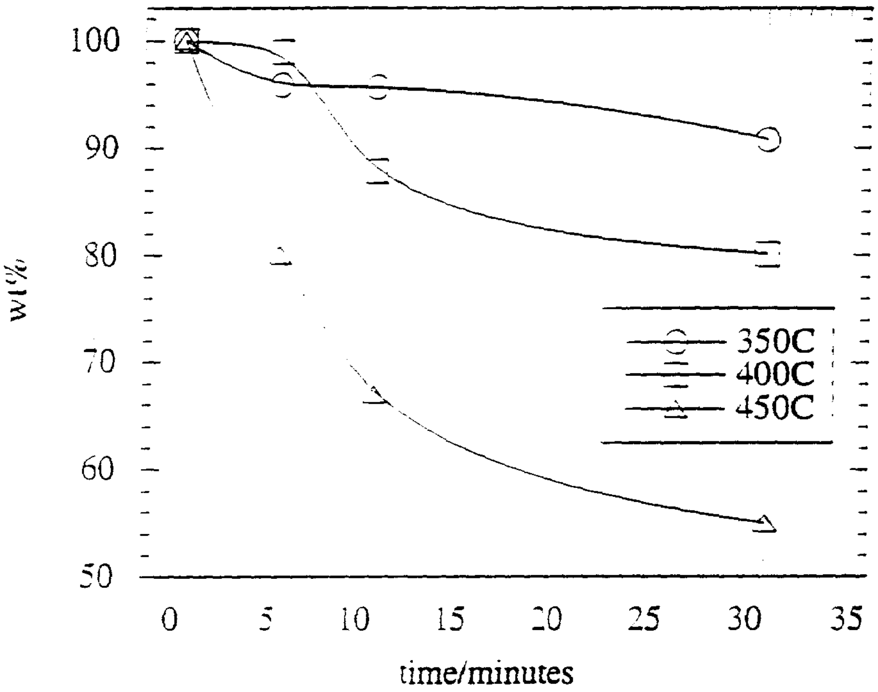

Figure 55. Effect of temperature on tetralin to naphthalene conversion during dehydrogenation.

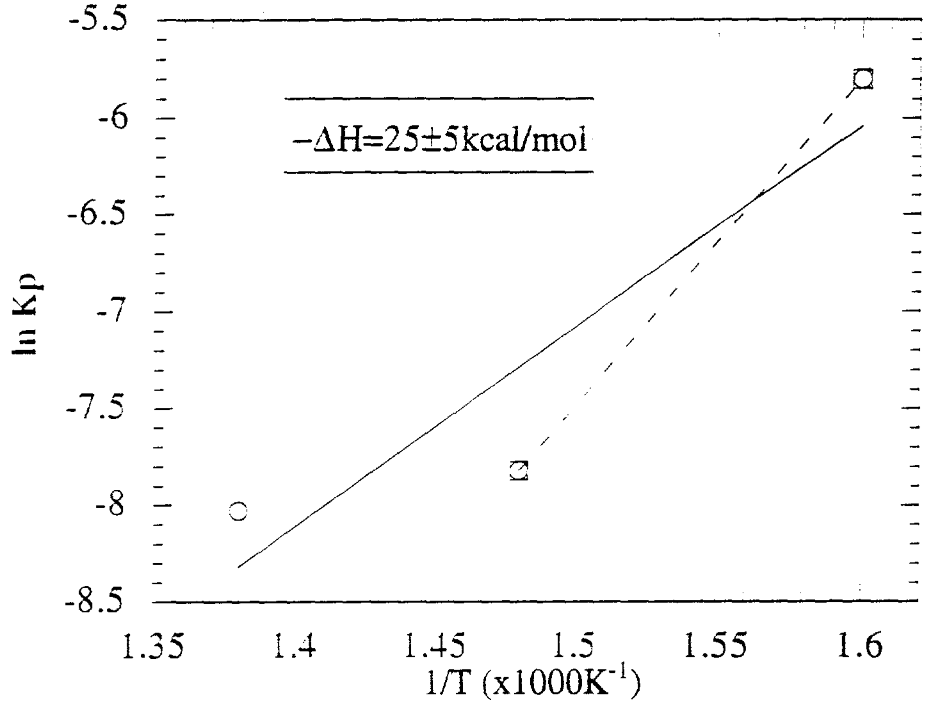

Figure 56. Van't Hoff plot of naphthalene hydrogenation.

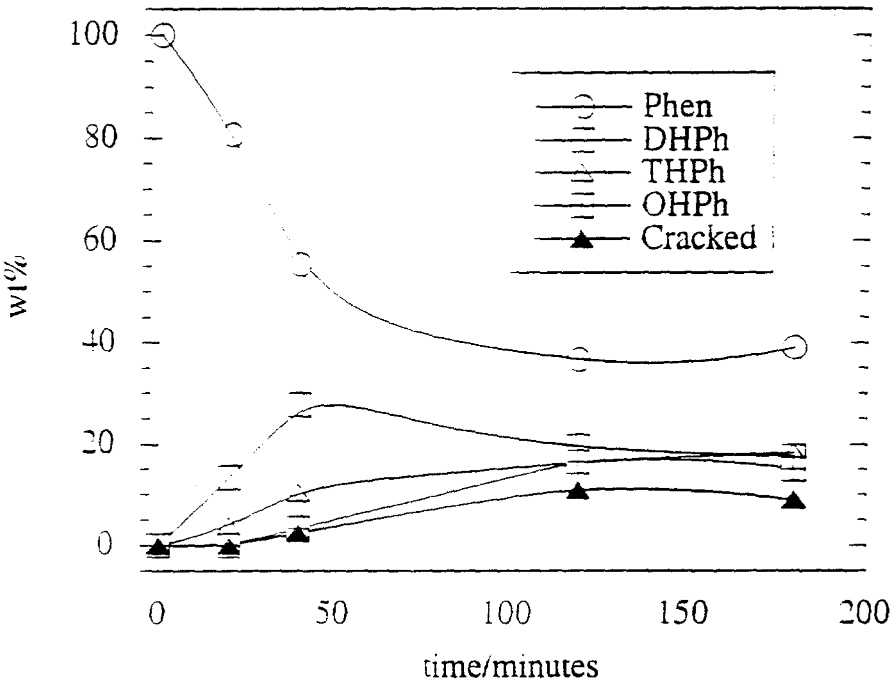

Figure 57a. Phenanthrene hydrogenation product distrubution at 350°C.

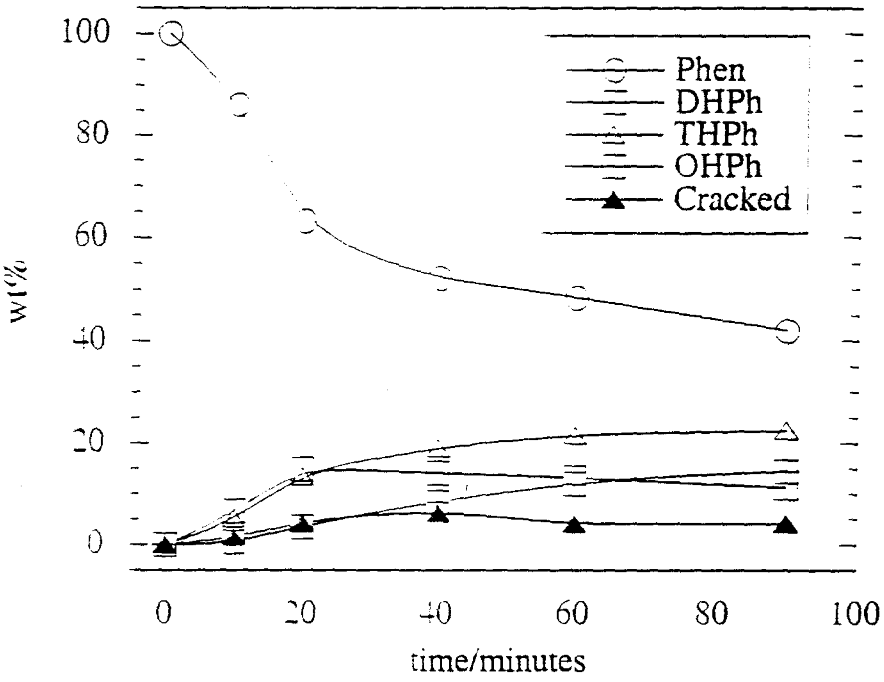

Figure 57b. Phenanthrene hydrogenation product distrubution at 400°C.

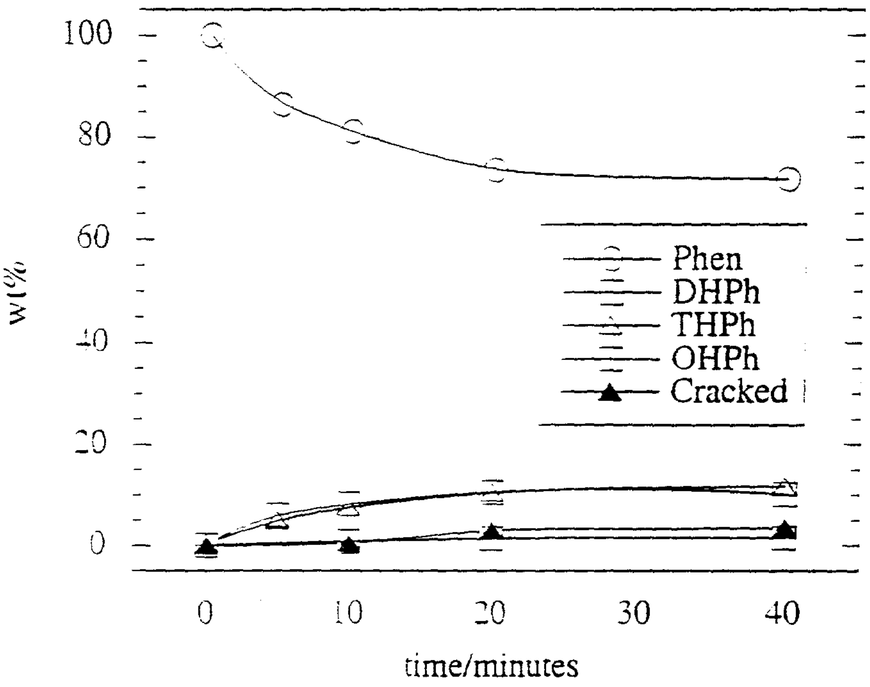

Figure 57c Phenanthrene hydrogenation product distrubution at 450°C.

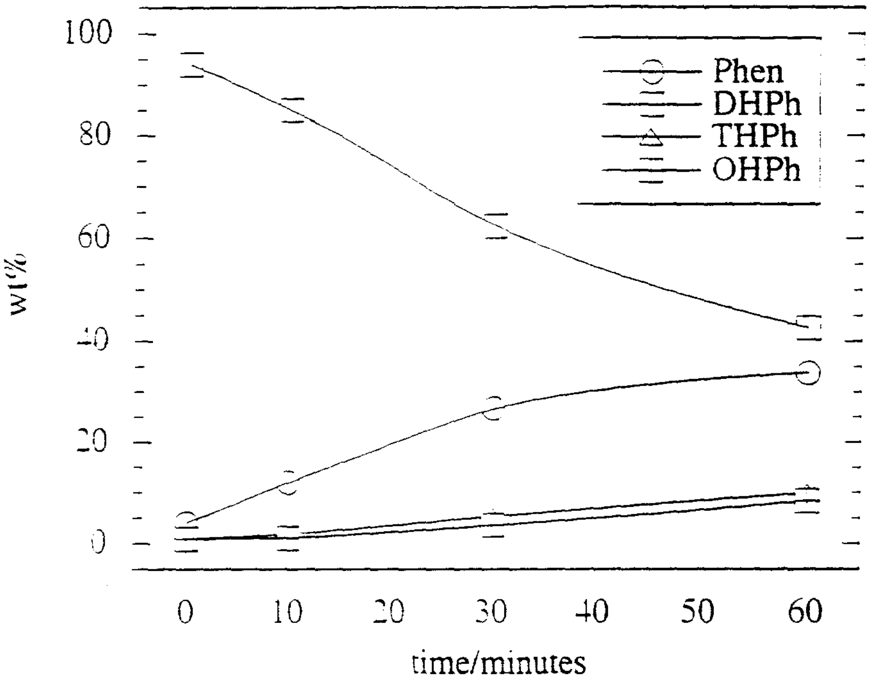

Figure 58. Dihydrophenanthrene hydrogenation product distribution at 350°C.

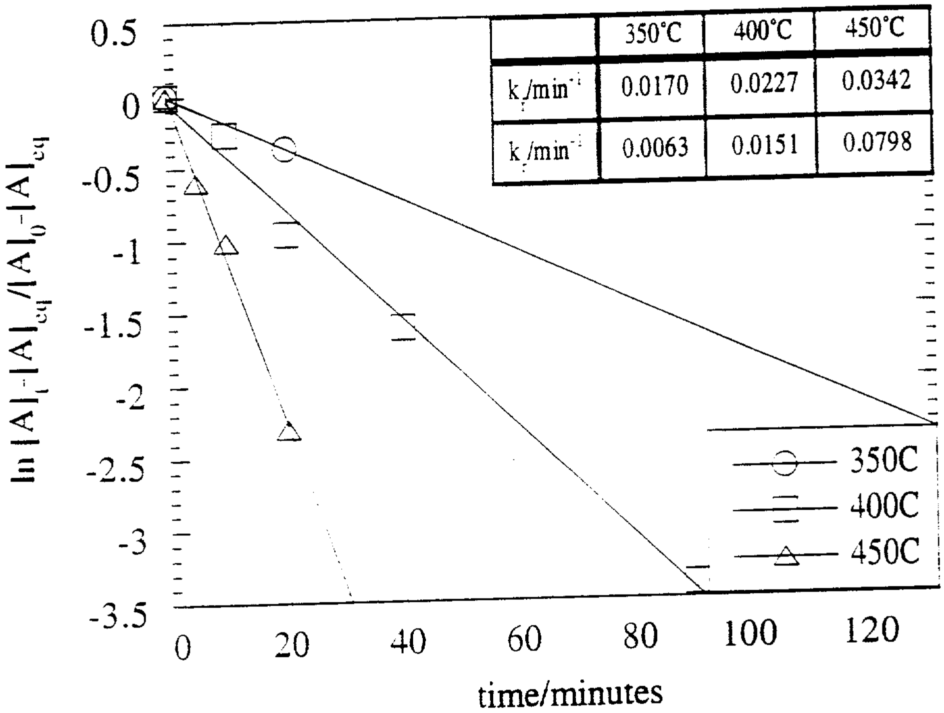

	350°C	400°C	450°C
k_f/min^{-1}	0.0170	0.0227	0.0342
k_r/min^{-1}	0.0063	0.0151	0.0798

Figure 59. Phenanthrene hydrogenation kinetics at 350, 400 and 450°C.

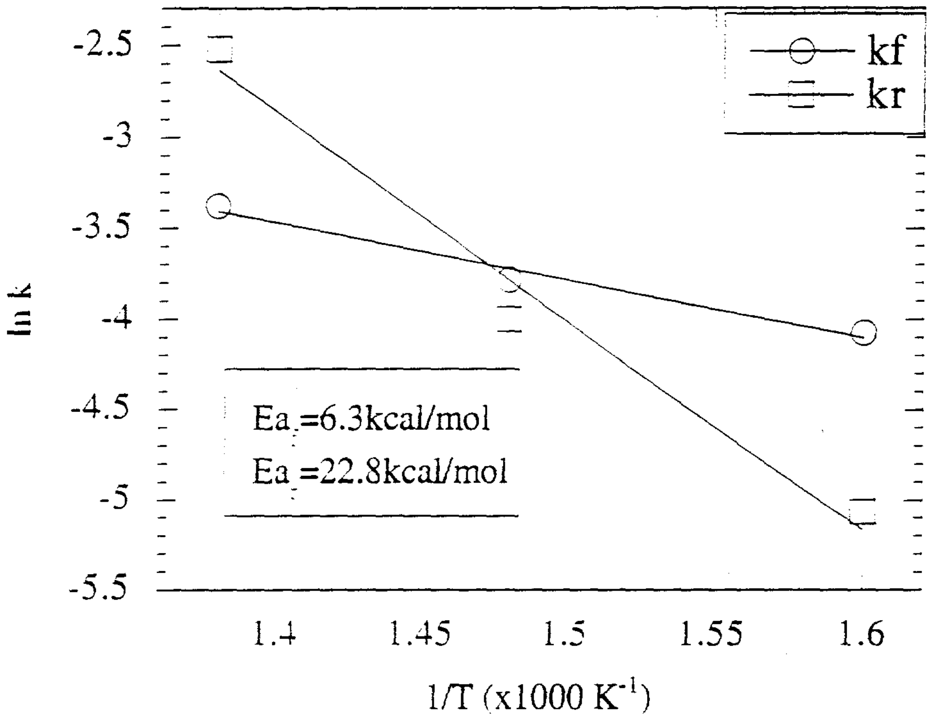

Figure 60. Phenanthrene hydrogenation/dehydrogenation Arrhenius plot.

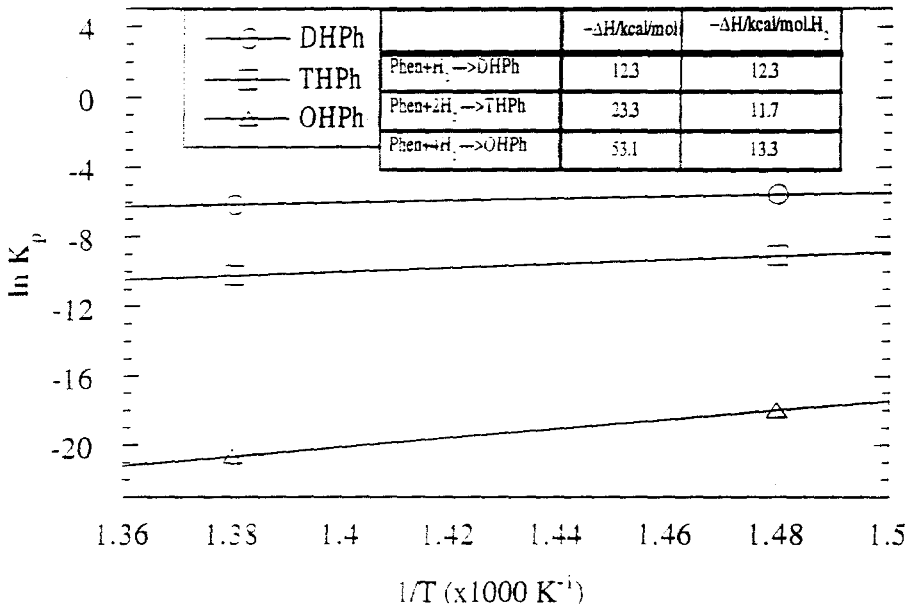

	$-\Delta H$/kcal/mol	$-\Delta H$/kcal/molH_2
Phen+H_2—>DHPh	12.3	12.3
Phen+2H_2—>THPh	23.3	11.7
Phen+4H_2—>OHPh	53.1	13.3

Figure 61. Van't Hoff plot of phenanthrene hydrogenation.

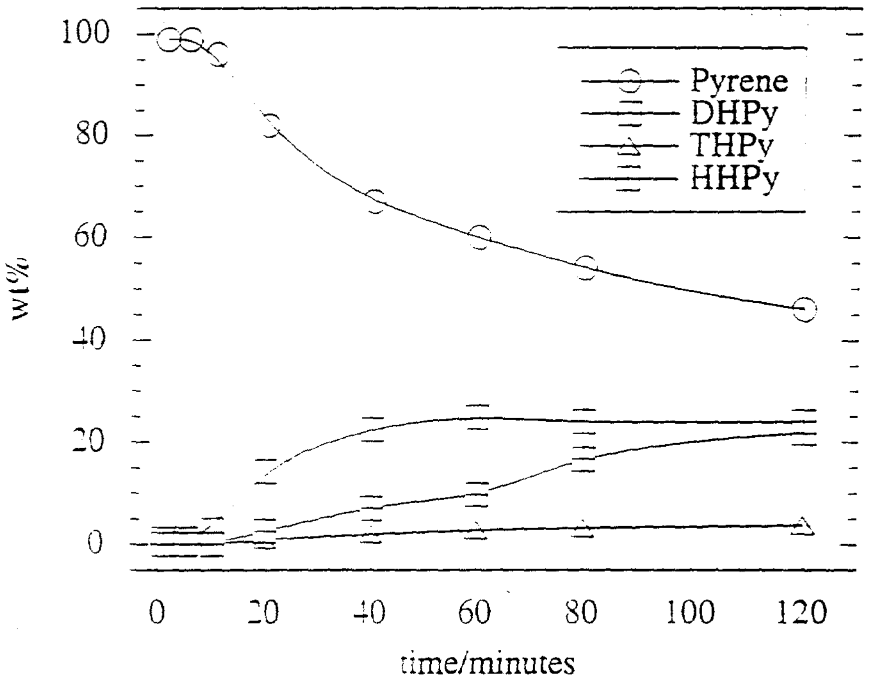

Figure 62a. Pyrene hydrogenation product distrubution at 350°C.

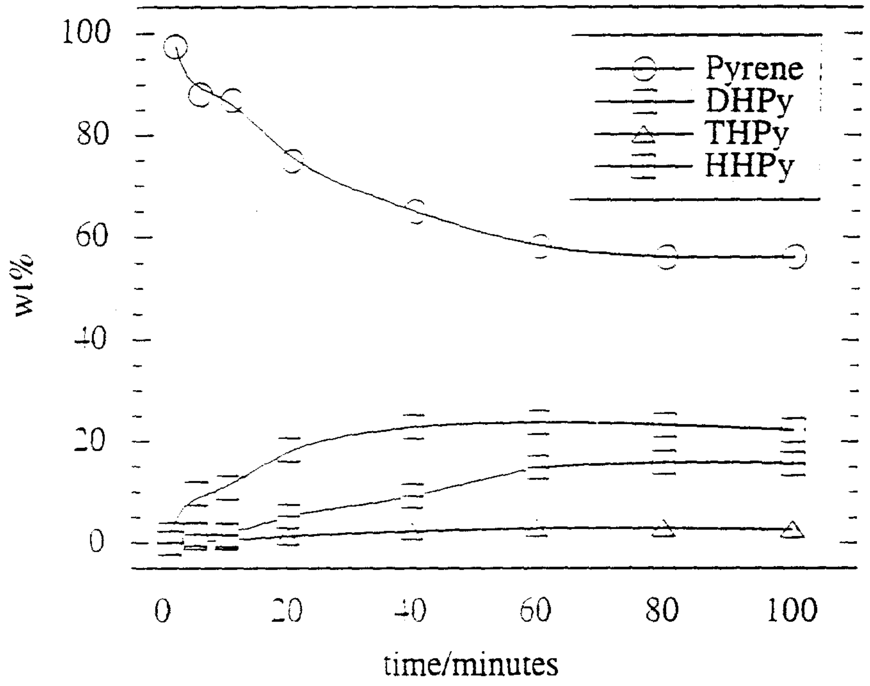

Figure 62b. Pyrene hydrogenation product distrubution at 400°C.

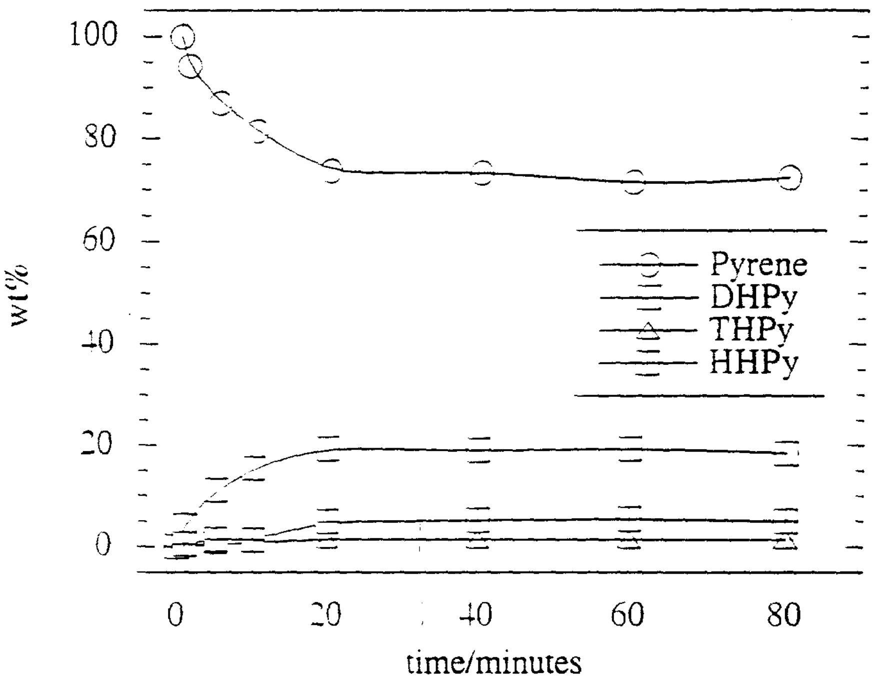

Figure 62c. Pyrene hydrogenation product distrubution at 450°C.

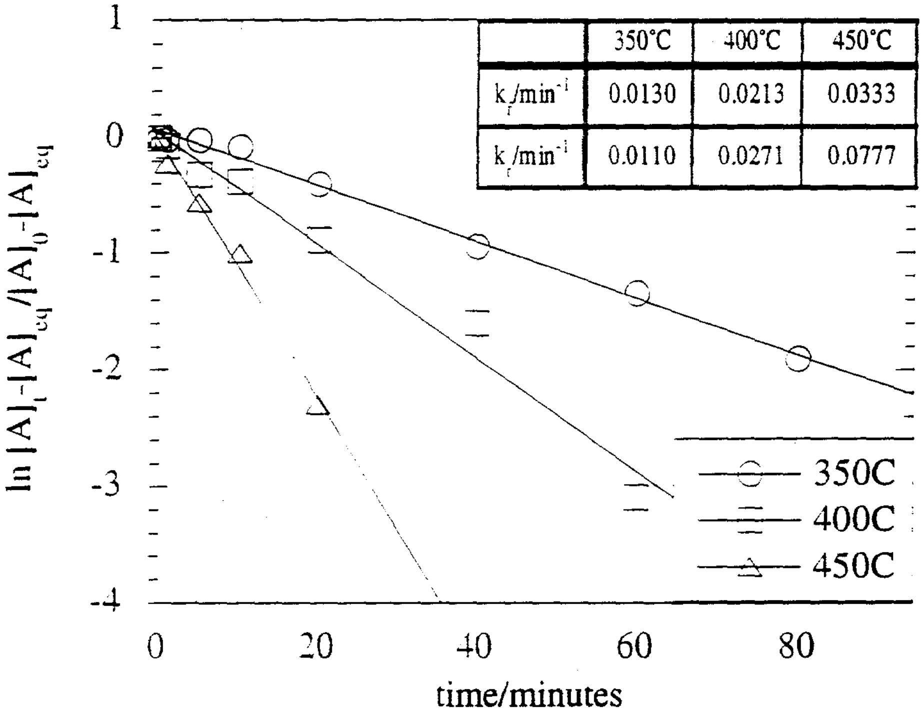

	350°C	400°C	450°C
k_f/min^{-1}	0.0130	0.0213	0.0333
k_r/min^{-1}	0.0110	0.0271	0.0777

Figure 63. Pyrene hydrogenation kinetics at 350, 400 and 450°C.

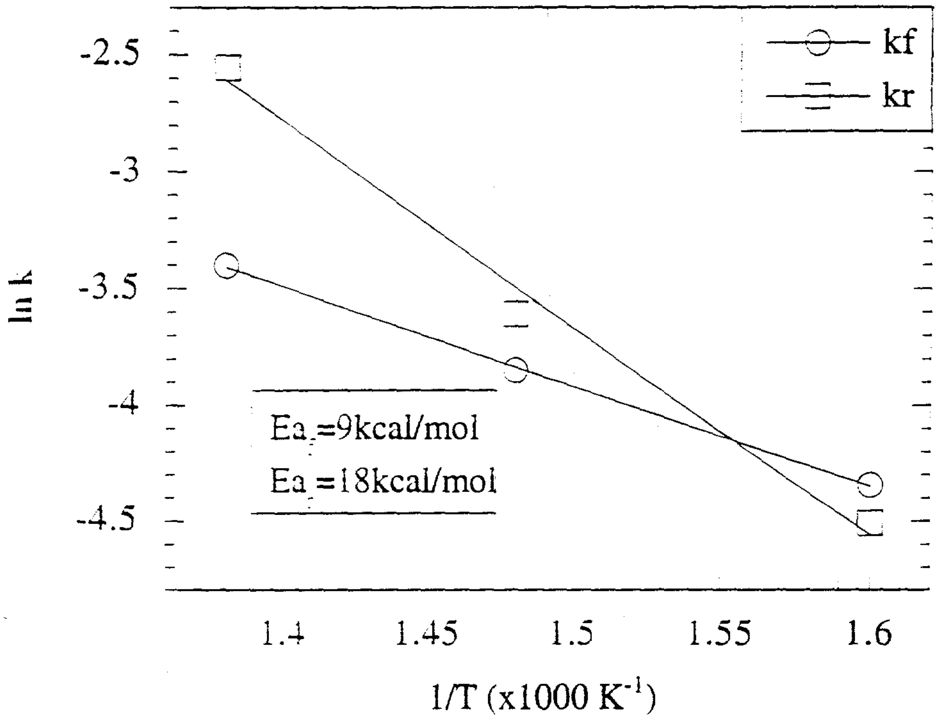

Figure 64. Pyrene hydrogenation/dehydrogenation Arrhenius plot.

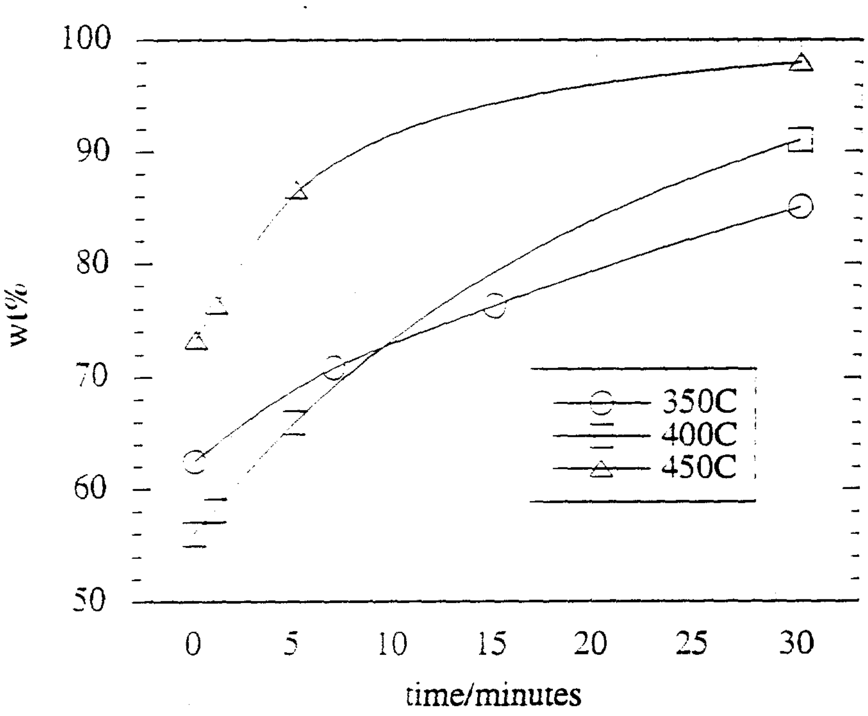

Figure 65. Effect of temperature on hydrogenated pyrenes to pyrene conversion during dehydrogenation.

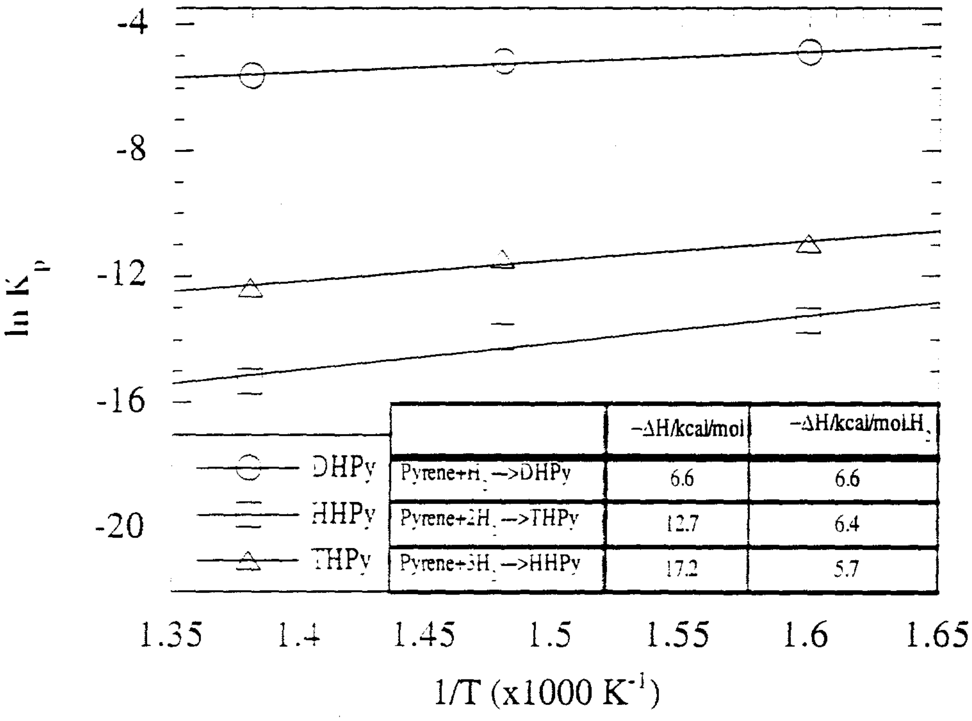

	$-\Delta H$/kcal/mol	$-\Delta H$/kcal/mol.H_2
Pyrene+H_2—>DHPy	6.6	6.6
Pyrene+$2H_2$—>THPy	12.7	6.4
Pyrene+$3H_2$—>HHPy	17.2	5.7

Figure 66. Van't Hoff plot of pyrene hydrogenation.

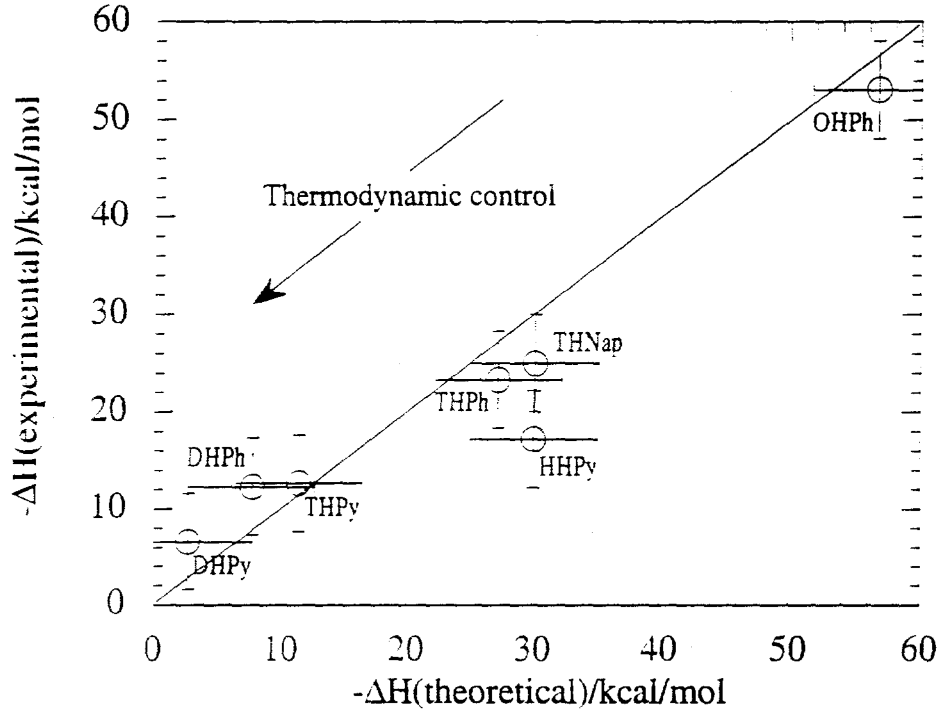

Figure 67. Comparison of -$\Delta H_{hydrogenation}$ from present work with theoretical data [37].

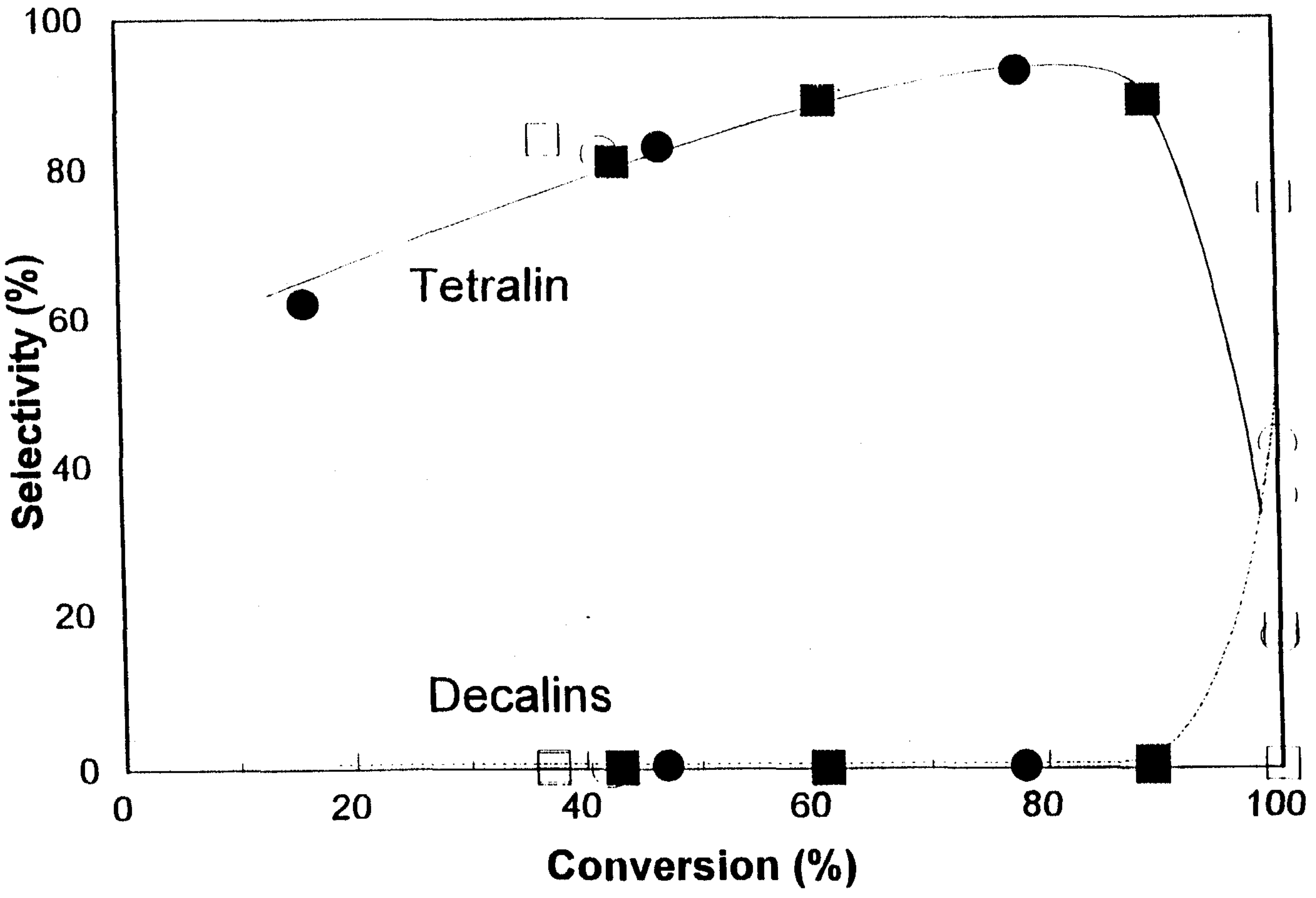

Figure 68. Selectivity to tetralin and decalins as a function of naphthalene conversion during the naphthalene hydrogenation at 473K over Pd/Al_2O_3 (○, ●) and Pd/TiO_2 (□, ■). Open symbols: runs without benzothiophene; filled symbols: runs in the presence of benzothiophene.

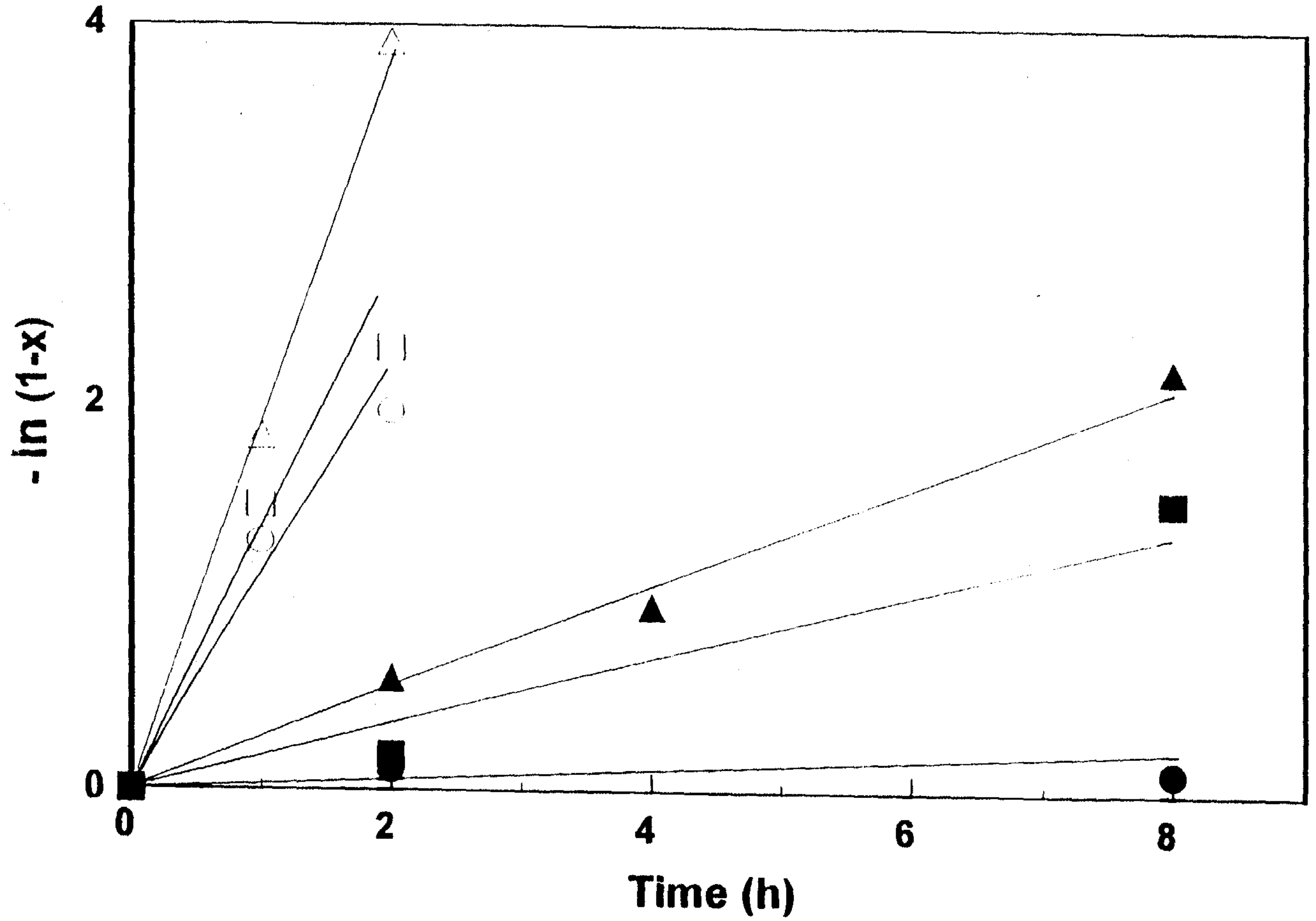

Figure 69. Pseudo-first-order plot of the naphthalene hydrogenation over Pt/Al_2O_3 (○, ●), Pd/Al_2O_3 (□, ■) and Pd/TiO_2 (△, ▲). Open symbols: runs at 553K with no addition of benzothiophene; filled symbols: runs at 473K in the presence of benzothiophene.

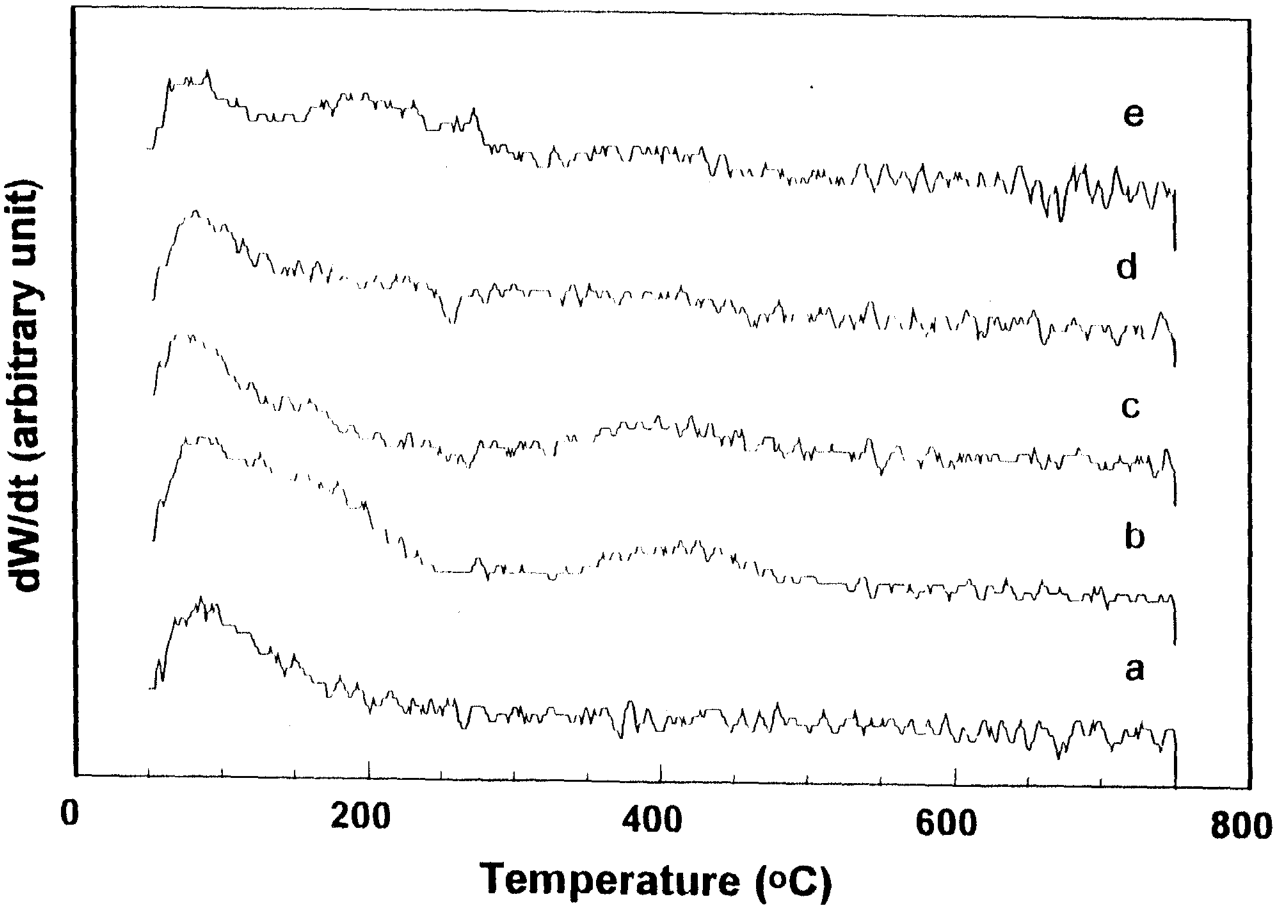

Figure 70. TGA results of fresh and used Pd/Al2O3 catalysts: (a) fresh, (b) exposed to reaction mixture at room temperature for 30 min., (c) reaction at 553K for 2h, (d) reaction at 473K for 2h, and (e) reaction at 473K for 2h in the presence of benzothiophene.

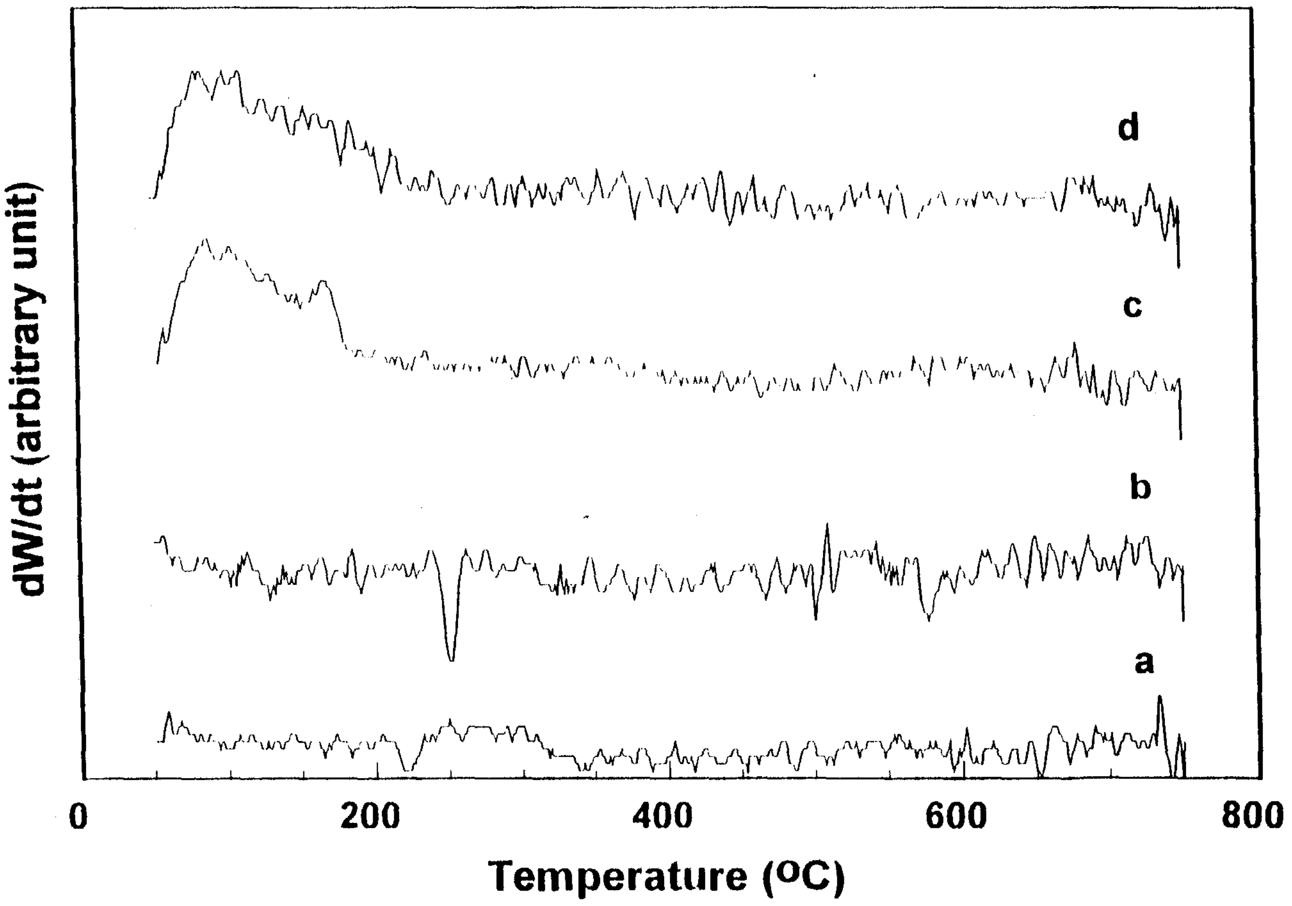

Figure 71. TGA results of used catalysts after reaction at 473K for 2h: (a) Pd/TiO2 with no addition of benzothiophene, (b) Pd/TiO2 in the presence of benzothiophene, (c) Pt/Al2O3 with no addition of benzothiophene, and (d) Pt/Al2O3 in the presence of benzothiophene.

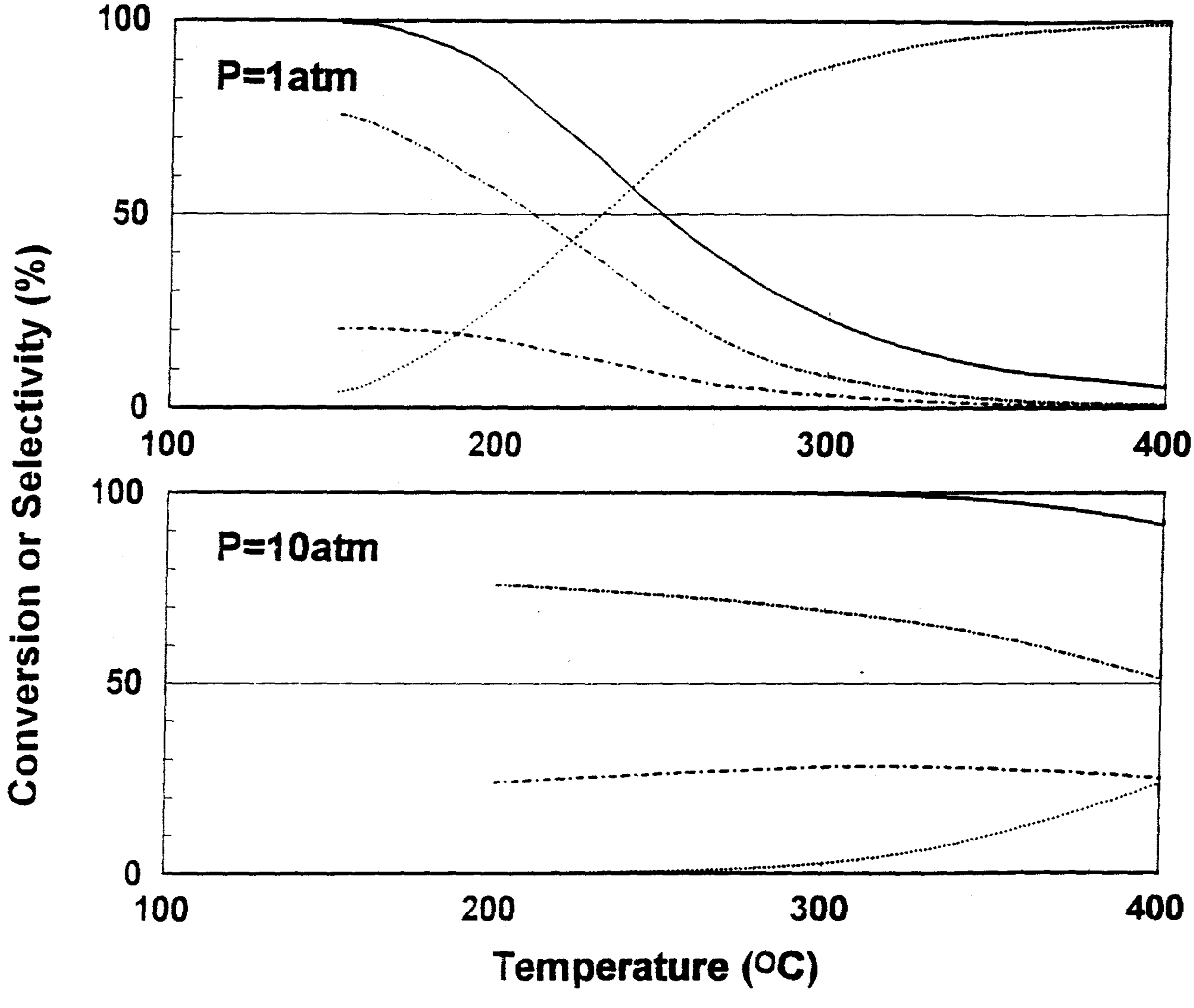

Figure 72. Calculated equilibrium conversion of naphthalene and product selectivity as a function of reaction temperature (see text for details). Conversion of naphthalene (——), selectivity to tetralin (•– – –), selectivity to trans-decalin (—•—), and selectivity to cis-decalin (—••—).

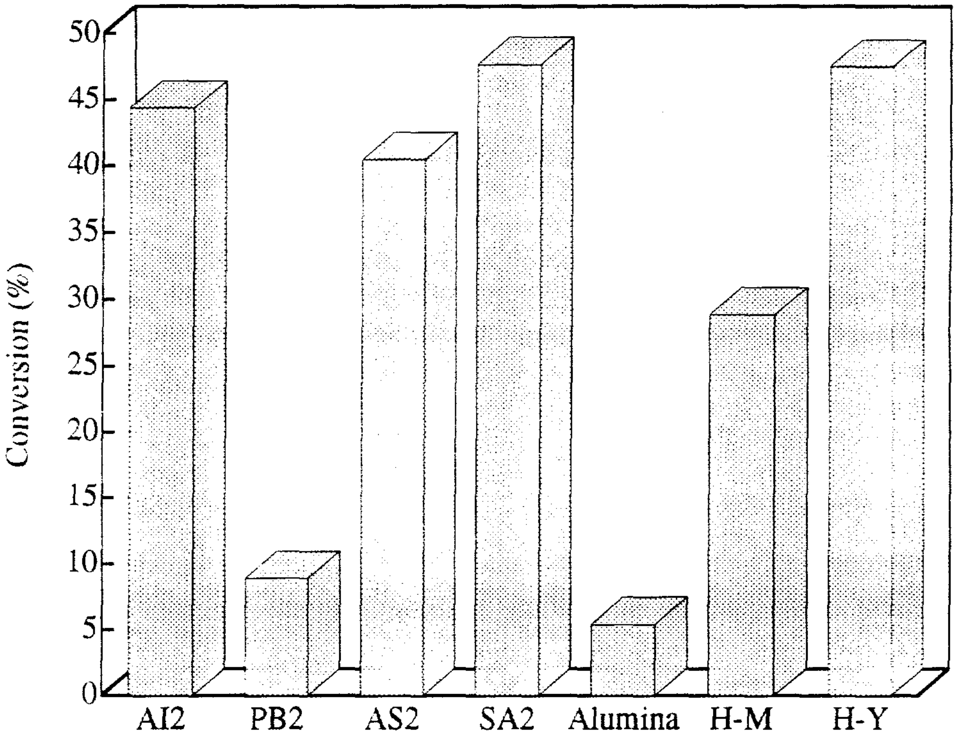

Figure 73. Comparison of catalytic activities of various catalysts for the reaction of 1,3,5-Triisopropylbenzene hydrocracking.

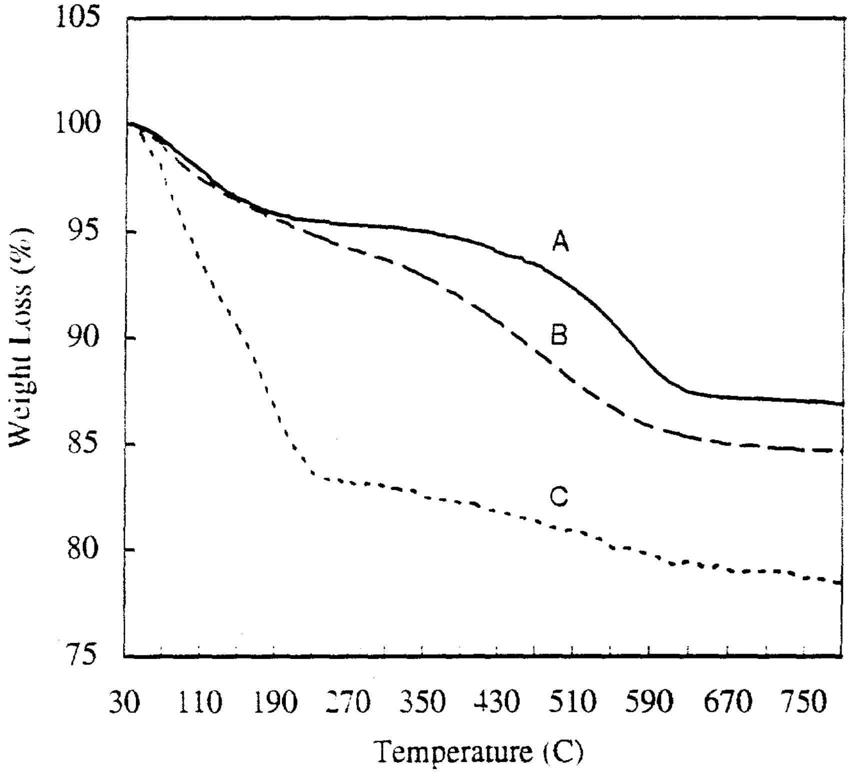

Figure 74. Thermogravimetric Analysis of used A) Mordenite, B) Zeolite Y, and C) MCM-41 catalysts.

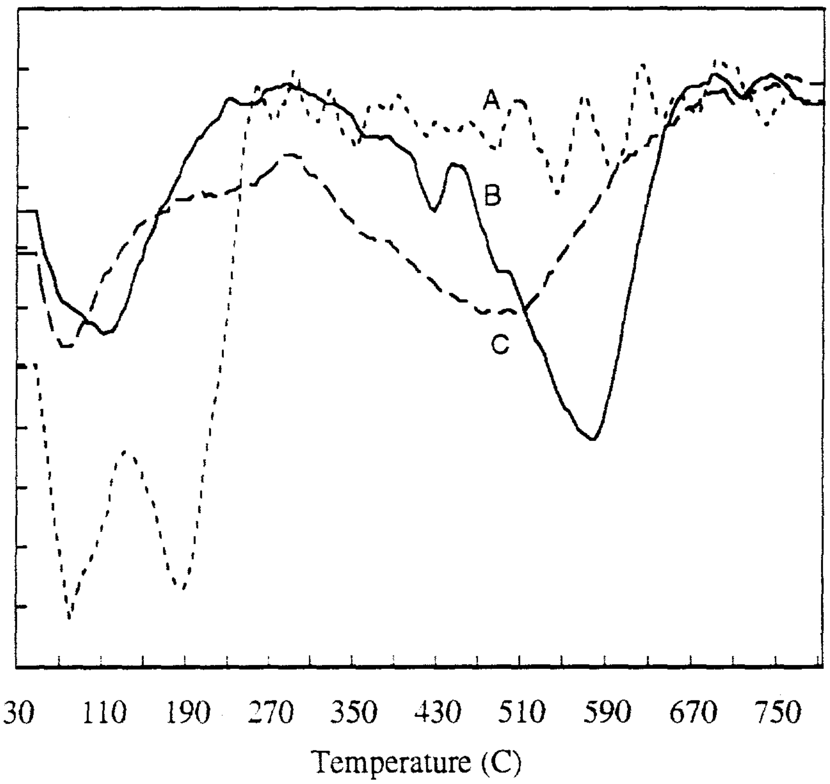

Figure 75. Differential Thermogravimetric Analysis of A) MCM-41, B) Mordenite, and C) Zeolite Y catalysts recovered after the reactioncatalysts.